

ABSTRACT

CERNIWAY, MATTHEW. Elliptical Diamond Milling: Kinematics, Force and Tool Wear (under the direction of Professor Thomas A. Dow)

Machining with diamond tools, whether turning or milling has proven itself as the manufacturing process that produces the highest quality surface finish, with the least amount of form error in the minimum amount of time. However, due to tool wear and the amount of force generated during conventional machining, diamond tools cannot be used on carbon containing materials such as steel and brittle materials such as silicates. In an attempt to by-pass the material limitations of diamond machining, a new machining process called vibration assisted machining (VAM) has been developed. VAM involves oscillating the diamond tool, bringing it into and out of contact with the material in rapid succession. VAM can either be 1-dimensional (1D), oscillation in a single direction, or 2-dimensional (2D), a summation of two independent tools motions. Currently, research efforts are focused on 2D vibration machining, 2D tool motion haven been shown to be superior to 1D tool motion. Over the past 10 years, 2D VAM with diamond tools has been demonstrated to reduce the amount of machining force and increase tool life when machining carbon-containing materials over that of conventional machining processes. However the mechanisms of this improvement have yet to be discovered. This research effort is focus on: 1) discovering the fundamental mechanical principals behind the improvement, force reduction and tool wear, 2) developing a model that predicts the cutting forces and tool contact times, 3) establishes guidelines for the use of vibration assisted machining and 4) developing an industrial grade 2D VAM servo. The reductions in tool wear and machining forces are related to the path geometry of the diamond tool and the speed and the depth at which it engages the workpiece. A model has been developed and experimentally verified for 2D VAM which predicts the machining forces and workpiece / tool contact time if the material properties are known. Along with the model, a set of charts has been developed for both 1D and 2D VAM that relate the key machining variables to one another. Lastly, a robust 2D VAM diamond tool servo has been designed.

**ELLIPTICAL DIAMOND MILLING:
KINEMATICS, FORCE AND TOOL WEAR**

by
Matthew Allen Cerniway

A dissertation submitted to the Graduate Faculty of
North Carolina State University
In partial fulfillment of the
Requirements for the Degree of
Masters of Science

DEPARTMENT OF MECHANICAL AND AEROSPACE ENGINEERING

Raleigh

2001

Approved By:

Chair of Advisory Committee

*To my loving wife, Rachael
(the adventure begins)*

BIOGRAPHY

MATTHEW ALLEN CERNIWAY was born on October 29th, 1973 in Long Beach California to Leon and Mary Cerniway. Showing a propensity for designing and building things at an early age, Matthew's track to becoming a future engineer was always known. Under the direction of his Father, Matthew became a skilled machinist and woodworker. Graduating at the top of his class in 1992 from Greenbrier Christian Academy in Chesapeake, Virginia, Matthew entered North Carolina State University to pursue a degree in Mechanical Engineering. In the spring of 1996, Matthew graduated from University and went to work for Nan Ya Plastics Corporation in Lake City, South Carolina. Supervising a maintenance group of 9 technicians, it was here that Matthew learned how to be an effective team leader. With a desire for more design work, Matthew relocated to Pittsburgh, Pennsylvania in the summer of 1997 to work as a facility engineer at II-VI Incorporated, a manufacturer of laser optics. While directing the maintenance effort and redesigning various manufacturing support equipment, Matthew interacted with systems operating with extremely hazardous materials on a daily basis. This imprinted on him the importance of safety in the design of mechanical systems. Due to a slow down in the optics market, Matthew was laid off from II-VI the following summer. With his varied skill set, Matthew was asked to join a National Science Foundation (NSF) research effort in Antarctica. Working for the Polar Ice Coring Office (PICO) at the University of Nebraska, Matthew served as the engineering advisor and ice core driller during the 1998-1999 field season at Siple Dome, Antarctica. For this Matthew received the Antarctic Service Medal from the NSF. Returning to the United States in 1999, Matthew decided to attend graduate school to obtain the higher level of engineering training need to qualify for the precision design positions that he had always wanted. Matthew returned to North Carolina State University in the summer of '99. Under the direction of Dr. Thomas Dow, Matthew began his Masters research work at the Precision Engineering Center (PEC) on Elliptical Diamond Milling for the Kodak Corporation. Matthew completed his Masters training in mechanical engineering in 2001. Currently, Matthew is employed with the Naval Surface Warfare Center in Washington DC as a researcher and analyst in acoustics.

ACKNOWLEDGEMENTS

This author would like to thank the following people and organizations for their support in this endeavor:

- To Jesus Christ, my Lord and Savior, without whom I could not have completed this educational endeavor.
- The Kodak Corporation for sponsoring this research project.
- Professor Thomas A. Dow, Professor Richard Keltie and Professor Ronald Scattergood. I feel truly honored to have been trained by such brilliant academics. Your love for your work inspired me. I thank you for that, as well as for your time and patience as I figured out the intricacies of this project.
- Staff of the PEC; Alex Sohn, Ken Garrard and Ena Meng. A more talented, friendly and willing to teach group I have never met. Even when you had little time to complete your own projects, you somehow made time to help me. And it was done with a genuine willingness and a smile that made me feel important. Thank you.
- My fellow graduate students, the “heart and soul” of the PEC, for their friendship and assistance. Whether it was help with a piece of equipment or as a sounding board for ideas, they were always up to the task. My heart felt thanks to Markus Bauer, Matias Heinrick, David Gill and Byoung Loh.
- Rachael, my wife. I know her heart broke every week when I had to leave her 200 miles away in Virginia to return to school. Mine did as well. Thank you for your never-ending love, patience and understanding.

CONTENTS

List of Tables	viii
List of Figures	ix

CHAPTER 1: INTRODUCTION

1.0 Historical Information	1
1.1 Current Needs of Industry	2
1.2 Innovative Techniques	2
1.3 Vibration Assisted Machining (VAM)	3
1.3.1 System Classification	3
1.3.2 Servo Designs	4
1.3.3 Reported Benefits of Vibration Assisted Machining	7
1.4 Research Goals	8
1.4.1 Servo Mechanics	8
1.4.2 Surface Feature Characterization	9
1.4.3 Force Model	9
1.4.4 Tool Wear of Subsonic Cutting	9

CHAPTER 2: ELLIPTICAL MOTION

2.0 Diamond Turning Basics	10
2.1 VAM Basics: Process Technology	10
2.1.1 One Dimensional Vibration Assisted Machining	11
2.1.1.1 Duty Cycle for One Dimensional Cutting	14
2.1.2 Two Dimensional Vibration Assisted Machining	16
2.1.2.1 Duty Cycle for Two Dimensional Cutting	18
2.2 Servo Mechanics: PEC Prototype	21
2.2.1 Components	22
2.2.2 Linkage Motion	23
2.2.3 Support Equipment	25
2.2.4 Path Measurement	26

2.2.5 Natural Frequency and Operational Parameters	27
CHAPTER 3: DEVELOPMENT OF ELLIPTICAL MODEL	
3.0 Surface Topography	29
3.1 Chip Shape	30
3.1.1 Controlling Parameters	31
3.1.2 Projected Tool Shape	32
3.2 Phase	33
3.3 Linear Cutting Model	35
3.4 Elliptical Cutting Model	36
3.4.1 Development of Elliptical Cutting Model	37
3.4.2 Complete Elliptical Model	50
3.4.2.1 Thrust Force	50
3.4.2.2 Cutting Force	52
3.4.2.3 Force vs. Duty Cycle	54
3.4.2.4 Limits of VAM Force Advantage	58
3.4.2.5 Class “A” Continuous Chip	60
3.4.3 Reported “Lifting” Phenomena of Elliptical Machining	62
3.4.3.1 Lifting Mechanics	62
3.4.3.2 Moriwaki’s Lifting Phenomena	65
CHAPTER 4: VAM MACHINING AND TOOL WEAR	
4.0 VAM Research Past and Present	67
4.0.1 Materials	67
4.0.2 Experimental Setup for Surface Feature Measurement	69
4.0.3 HSR Setup: Turning	72
4.1 Surface Topography	74
4.1.1 Surface Features	75
4.1.1.1 Phase	75
4.1.1.2 Up-Feed	76
4.1.1.3 Apparent Tool Radius	78

4.1.2 Metrology: Surface Roughness and Form Error	79
4.2 Force Measurements	82
4.2.1 Elliptical Vibration Machining Force Data	83
4.2.2 Comparison to Model	84
4.2.3 Benefits of a “Sharp” Tool	88
4.2.4 Discussion of Vibration Assisted Cutting Results	89
4.3 Vibration Assisted Machining of Steel with Diamond Tools	90
4.3.1 Tool Wear and VAM	90
4.3.2 Experimental Setup	91
4.3.3 Elliptical Vibration Cutting of Steel Results	92
4.3.4 Discussion of Diamond Turning of Steel	97
CHAPTER 5: HIGH SPEED PROTOTYPE	
5.0 Goals	98
5.1 Design of the High Speed Servo	98
5.1.1 Actuator	100
5.1.2 Cutter Head	102
5.1.3 Preload Spring	103
5.1.4 Diamond Tool	105
5.1.5 Support Equipment	105
5.1.6 System Specifications	106
CHAPTER 6: CONCLUSIONS AND FUTURE WORK	
6.0 Questions Answered	110
6.1 Summary	111
REFERENCES	113
APPENDIX A (MathCad Programs)	115
APPENDIX B (UMHS Detailed Drawings)	137

LIST OF TABLES

1.1	Results of Diamond Tool VAM Research	7
2.1	UMLS Operational Parameters of Build Shown in Figure 2.16	28
3.1	Example of Elliptical Duty Cycle Numbers	37
3.2	VAM for Force Model	38
3.3	Tool Geometry	39
3.4	Measured Material Properties	39
3.5	Chip and Tool Component Velocities ~ Option Evaluation	65
4.1	Properties of Materials Used in Cutting Trials	67
4.2	Surface Roughness Comparison (Angular)	80
4.3	Recorded Peak Elliptical Cutting Forces	83
4.4	Prediction Accuracy for Peak Machining Forces and Chip Length ..	87
4.5	Radial Surface Roughness of Turned Steel Flats	93
4.6	Angular Surface Roughness of Turned Steel Flats	93
5.1	UMHS Tool Path Specifications	106
5.2	UMHS Cutter Head Specifications	107
5.3	UMHS Natural Frequency	107
5.4	Piezoelectric Material	107
5.5	Miscellaneous Parameters	107
5.6	UMHS Cooling	108
5.7	UMHS Amplifiers	108
5.8	UMHS Chillers	108
5.9	UMHS Function Generator	109

LIST OF FIGURES

1.1	1D and 2D “Elliptical” Vibrations Cutting	4
1.2	Fraunhofer Design	4
1.3	Servo Design from the University of Bremen, Germany	5
1.4	Servo Design form Pusan National University, Korea	6
1.5	Servo Design from Kobe University, Japan	7
2.1	Tool / Workpiece Arrangement on a DTM	10
2.2	1D Vibration Cutting	11
2.3	Cutting Cycle for Vibration Assisted Machining (VAM)	13
2.4	Contact Snapshot	14
2.5	Diamond Cross-Section	15
2.6	1D Duty Cycle Chart	16
2.7	Ellipse	17
2.8	Basic 2D VAM ~ Overlapping Ellipses	18
2.9	2D Duty Cycle Chart	20
2.10	UltraMill-LS Reflected in a Turned Aluminum Sphere	29
2.11	Low Speed Prototype	22
2.12	Linkage and Path Shapes	23
2.14	Y-Axis Relationship to Phase Separation	25
2.15	Motion Measurement Setup for UMLS	26
2.16	Tip Motion of UMLS (Below 1 st Nat. Freq.)	27
3.1	Resultant Surface Finish via “Scooping” Motion	30
3.2	Chip Classification	31
3.3	Chip Cross-Section	32
3.4	Projected Tool Size	33
3.5	Row Alignment ~ Phase	33
3.6	Surface Roughness and Phase	34
3.7	Cross-Section of Plated Copper Chip w/ Segment and Forces Overlaid	35
3.8	Standard Cutting Model Tool / Workpiece Interface	38
3.9	Basic Geometry in 2D “Straight Line” Elliptical Cutting	40

3.10	Tool Contact Area and Length	42
3.11	Chip Thickness and Tool Contact Area	43
3.12	Tool Edge Components and Elliptical Cutting Cycle.....	45
3.13	Variable Rake Angle of VAM	47
3.14	Shear Angle Geometry	48
3.15	VAM Shear Angle	48
3.16	Hardness Correction Curve for Copper	50
3.17	VAM Thrust Force for 22% 2D Duty Cycle	51
3.18	VAM Cutting Force for 22% 2D Duty Cycle	52
3.19	VAM Force for 22% 2D Duty Cycle	53
3.20	VAM Thrust Force for 23% 2D Duty Cycle	54
3.21	VAM Cutting Force for 23% 2D Duty Cycle	55
3.22	VAM Force for 23% 2D Duty Cycle	55
3.23	VAM Thrust Force for 25% 2D Duty Cycle	56
3.24	VAM Cutting Force for 25% 2D Duty Cycle	56
3.25	VAM Force for 25% 2D Duty Cycle	57
3.26	Comparison of 2D VAM and Conventional Machining	58
3.27	VAM Thrust Force Comparison at 12.5% Increments	59
3.28	VAM Cutting Force Comparison at 12.5% Increments	60
3.29	Class “A” Chip for 23% 2D VAM	61
3.30	Chip Thickness Comparison	61
3.31	Chart from “Study of Elliptical Vibration Cutting” Lifting Phenomena	62
3.32	Shear Angle and Chip Velocity	64
3.33	Orientation of the Moriwaki Servo Elliptical Path [7]	66
4.1	Indentation of a 0.5 kgf Load in Type W2 Steel Sample (500x)	69
4.2	UMLS and Support Equipment on DTM	70
4.3	Close-Up View of UMLS Mounted on DTM for Cutting Trials	71
4.4	Wiring Schematic of UMLS	72
4.5	Schematic of Spindle Drive Arrangement	73
4.6	Surface Roughness of Turned 1100 Series Aluminum Surface	74
4.7	Overlapping of Surface Features w/ Decreasing Part Radius	75

4.8	Up-Feed Variation from Theoretical Value	76
4.9	Surface Profile of a 0.035 HSR, 23% Duty Cycle Cut	77
4.10	Surface Profile of a 0.075 HSR, 25% Duty Cycle Cut	77
4.11	Oblique Plots of Turned Copper Flats	78
4.12	Definition of Traced Paths	79
4.13	Angular Trace of Standard Turned Flat	79
4.14	Angular Trace of VAM Turned Flat	80
4.15	Change in Surface Profile w/ HSR	81
4.16	Exploded View of Sample Holder Used to Measure Cutting Forces	82
4.17	Duty Cycle Force Data for C110 Copper	84
4.18	Illustration of Key Machining Force Features	85
4.19	Figure 4.19: Measured / Predicted Forces for 22% 2D VAM	86
4.20	Measured / Predicted Forces for 23% 2D VAM	86
4.21	Measured / Predicted Forces for 2D VAM	87
4.22	Reduction in Machining Forces Due to a Sharp Tool	89
4.23	Photograph of Conventionally Diamond Turned Steel Surface	92
4.24	Photograph of Diamond Turned VAM Steel Surface	93
4.25	Oblique Plot of a Non-Vibration Turned Steel Part	94
4.26	SEM Images of Post Trial 0.5 mm Radius Diamond Tools	95
4.27	SEM Images of Post Trial 0.5 mm Radius Diamond Tools	96
4.28	Theorized 2D VAM Tool Wear in Steel	97
5.1	Exploded Drawing of UMHS	99
5.2	Assembly Drawing of UMHS with Aluris Attachment	100
5.3	PZT Actuator of UMHS	101
5.4	Cross-Section of UMHS Cutter Head	102
5.5 I	Illustration of UMHS Assembly	104

CHAPTER ONE: INTRODUCTION

1.0 HISTORICAL BACKGROUND

Precision metal cutting is defined as a cutting technique, which enables the production of optical, mechanical and electronic components with micrometer or sub-micrometer form accuracy and surface roughness to within a few tens of nanometers [11]. Starting with the United States in the mid 60's, research into precision metal cutting was driven by the technological demands of defense and aerospace industries [11]. While still very important to the military complex, precision metal cutting has expanded its field of application to touch almost every aspect of manufacturing, whether molds for contact lens production or non-spherical mirror arrays used in the most advanced scientific research satellites.

The hydrostatic bearing with its sub-micrometer rotational accuracy was the first component of precision metal cutting to benefit from the research push [11]. Along with the refinement of conventional machine components (spindles, metrology frames, etc.), the development of linear motors in the late 70's and piezoelectric driven stages in the 80's allowed for tool positioning and control on the nanometer scale [11]. Not to be left out, materials research and the development of the monocrystalline diamond tool with its nanometric edge sharpness saw the levels of form error and surface roughness lowered even further [11].

The technology discovered and/or refined over the past 40 years has found it's way into one of three primary machining techniques: turning, planning or milling. Of these, turning has established itself as the preferred method due to its combination of relatively short machining time and high quality surface finish. Regardless of which manufacturing process is used, an additional polishing step is sometimes required to meet the ever-increasing demand of industry for better surface finishes and higher form accuracy [3,5].

1.1 CURRENT NEEDS OF INDUSTRY

The development of precision metal cutting equipment in recent years has not only been focused on better surface finishes, but also in expanding the manufacturing sphere of application. Machining of micro-scale parts is one such area. With the diminishing size and increasing complexity of audio/visual products, the demand for high-precision micro machining is only going to increase [3]. Multi-function components such as Fresnel lenses or other varying profile optics require higher form accuracy and lower cutting forces [3]. Though not typically thought of as significant, sub-Newton cutting forces become significant when the features being milled are less than half a millimeter in size. Workpiece deformation, chatter and burr become major problem at this micro scale [3].

Companies not associated with aerospace or optical components are considering diamond turning to achieve greater performance. Diamond turning is a process that uses a precision ground diamond cutting implement mounted on a lathe capable of nanometer positioning to produce nearly error free shapes (within micrometers of desired) with high quality surface finishes (roughness on nanometer scale). The high modulus and fracture toughness of diamond make for a tool that retains a uniform, sharp edge over extended cutting periods (up to hundreds of kilometers) [11].

The diamond turning of steel is a research topic that has been under serious investigation since the early 90's [4, 5, 6, 8, 14, 17]. Carbon containing materials such as steel do not lend themselves to being machined with diamond tools. It is theorized that the carbon in the material either chemically or mechanically weakens the carbon bonds in the diamond to produce rapid wear. If a surface finish of the same magnitude common on materials such as copper and aluminum (< 50 nm) could be manufactured in one step on steel parts, such as valve seats, higher performance as well as tremendous time and money savings could be realized.

1.2 INNOVATIVE TECHNIQUES

To meet industrial needs and expand the realm of diamond turning, several innovative machining methods and equipment modifications have been tried with varying degrees of

success. Evans attempted to machine stainless steel at cryogenic temperatures [17]. Casstevens experimented with diamond turning of carbon steel in a carbon-saturated environment [14]. Yet another method performed by Moriwaki and Masuda utilized CBN tools, with their low chemical reactivity to iron, to produce an optical quality surface on steel [16, 15]. While acceptable surface finishes were produced and tool life was extended, any single method failed to obtain the both [6].

1.3 VIBRATION ASSISTED MACHINING

In the mid 70's a new class of machining was born. This new technique was one in which the cutting tool underwent a cyclic displacement independent to the x, y and z-axis displacement of the lathe's slide ways. This class of machining was referred to as vibration cutting. Early experiments were primarily carried out at frequencies greater than 20 kHz. These "ultrasonic", frequencies greater than 18 kHz, trials however showed vibration machining to have little practical value. It took nearly two decades of slow growth before this technology started to show promise. Finally in the early 90's, research into vibration cutting at both low and high frequency produced results sufficient for industrial applications [8]. This mature class of machining is called Vibration Assisted Machining (VAM).

1.3.1 System Classification

The tool servos that operate on the VAM principal can be divided into two main classes: resonance and non-resonance. Servos that operate at a single or combination of two modes of vibration are called resonance systems. Typically benefiting from tool vibration greater than 20 kHz, this type of servo can only operate at discrete frequencies and produce displacement amplitudes less than 6 μm . In sharp contrast with these are the non-resonance devices that operate under the first natural frequency of the system. This setup offers the benefit of a range of operating frequencies as well as amplitudes 10+ times greater than the resonance servos. However the increased control and displacement comes at the price of low tool velocity and increased operational power requirements.

Within each class are sub-classes defined by the dimensional space in which the excited tool moves, i.e. one-dimensional (1D) and two-dimensional (2D). 1D systems operate in a plane parallel to that of the workpiece surface; that is inline with the principal or cutting force (Figure 1.1). Adding a dimension, 2D systems produce an elliptical tool motion where the major axis of the ellipse is inline with the cutting force and the minor axis is inline with the thrust force.

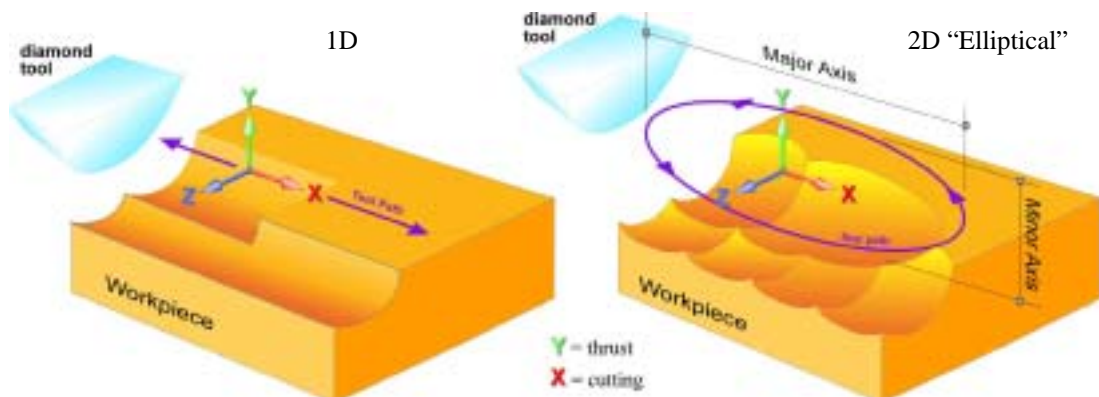


Figure 1.1: 1D and 2D “Elliptical” Vibration Cutting

1.3.2 Servo Designs

The evolution of vibration cutting is reflected in the development of the tool servos constructed. The simplest servo is one that operates on the 1D VAM principal. The majority of early research, circa 1980-1990, into vibration cutting utilized this type of system. A servo similar to the early designs is shown in Figure 1.2. This 1D servo developed at Fraunhofer, IPT was used to investigate ultrasonic assisted diamond turning

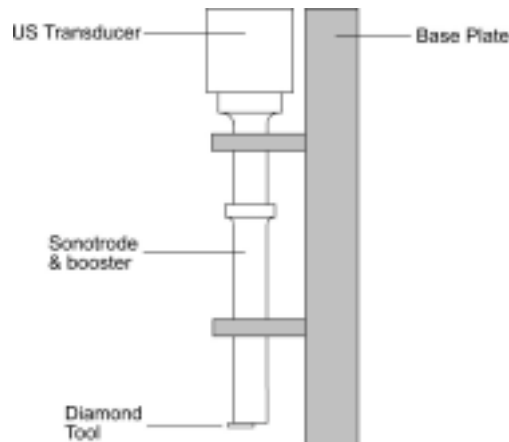


Figure 1.2: Fraunhofer Design

of steel and glass [5]. The operation of this servo is fairly simple. A piezoelectric transducer creates a 40 kHz longitudinal vibration, which is connected through a sonotrode to an amplification horn. The sonotrode, a non-amplifying resonator, is designed so that the ultrasonic energy input sets up a longitudinal resonance in the booster causing the amplitude of the vibration to be increased. This arrangement results in a $\pm 5 \mu\text{m}$ sinusoidal displacement of the diamond tool [5].

Researchers at the University of Bremen, Germany, realized that if the mass of the diamond tip were off the longitudinal or centerline axis, then an elliptical motion would be produced. Similar in construction to that of the Fraunhofer design, the Bremen design employs a 40 kHz, 700W ultrasonic generator coupled to a piezoelectric converter to produce its tool motion [4]. Utilizing a sonotrode / booster arrangement, a vertical amplitude of $6\mu\text{m}$ was produced. By locating the diamond off the centerline axis of the sonotrode, a bending resonance was induced. Summing the vertical and horizontal bending displacements results in an elliptical motion of the diamond tip. The elliptical tool path is slightly tilted do to the phase of the bending motion. Within certain limits, the elliptical motion of this servo could be controlled with the addition of a counterweight. Figure 1.3 illustrates this elliptical motion due to system imbalance and the orientation of the tool servo to the workpiece.

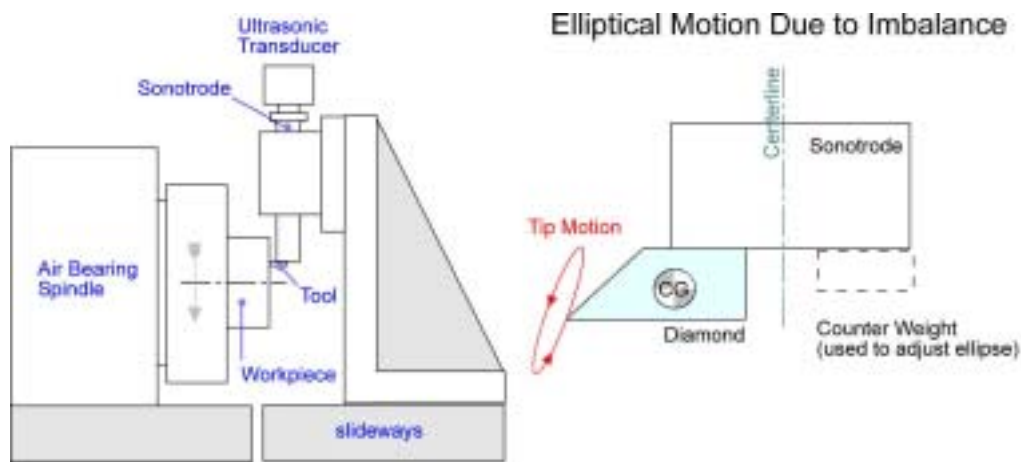


Figure 1.3: Servo Design From the University of Bremen, Germany

The positive results obtained from the Bremen study involving the diamond turning of steel (discussed in Section 1.3.3) shifted focus away from 1D systems to 2D systems. As previously mentioned, aside from the dimension of cutting motion, servos operate either at or below resonance. The servos illustrated in Figures 1.4 and Figures 1.5 represent non-resonance and resonance designs respectively. The Pusan University design seen in Figure 1.4 is a non-resonant design utilizing two piezoelectric actuators oriented 90° to each other. The piezo stacks are connected to the diamond tool through a plus (+) shaped flexure. The design of the flexure eliminates shear stress in one stack by the motion of the other [3]. The tool path that results is a summation of two arcs, which produce a quasi-ellipse. This research effort was primarily aimed at increasing the machining accuracy of micro-scale parts by using elliptical vibration cutting. The Pusan University, non-resonant servo operated at 1 kHz with a maximum axial displacement of 5 μm .

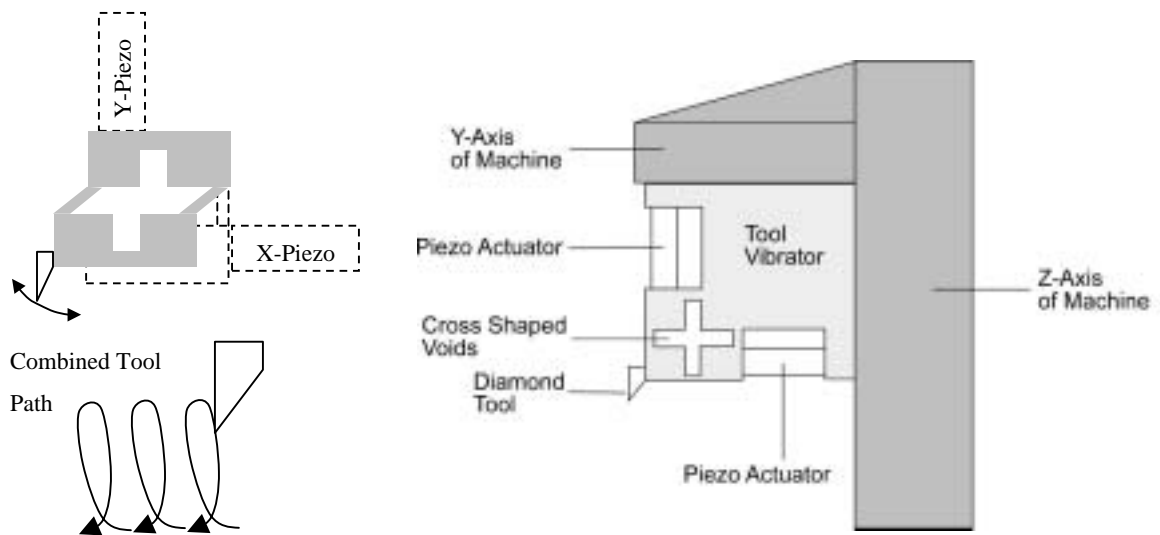


Figure 1.4: Servo Design From Pusan National University, Korea

Revisiting VAM in 1999, Shamoto and Moriwaki developed a 2D servo, shown in Figure 1.5, that operates at a resonance frequency of 20 kHz and produced an amplitude of 3.5 μm [6]. Their investigation focused on the benefits of vibration diamond cutting of hardened steel. This tool servo operated at the 3rd resonant bending mode to produce a circular path. Unlike previous designs where the actuators were in the same plane as the generated tool path, the actuators are perpendicular to the tool path.

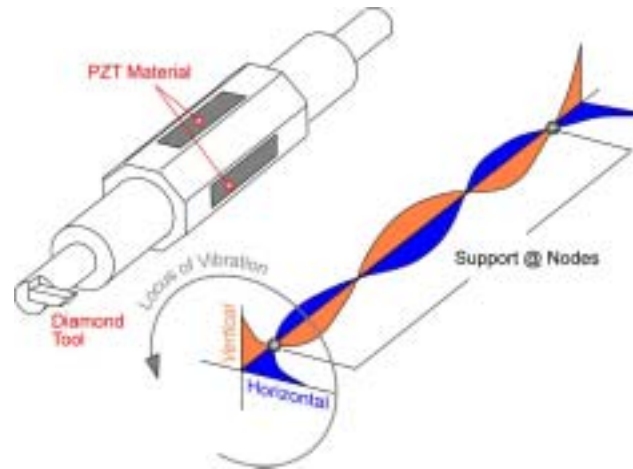


Figure 1.5: Servo Design From Kobe University, Japan

1.3.3 Reported Benefits of Vibration Assisted Machining

Experimental trials have shown that vibration assisted machining has the potential to become the key feature in the next generation of precision metal removal equipment.

Table 1.1 lists the location and results of the research efforts to date.

Table 1.1: Results of Diamond Tool VAM Research

Reported Benefits of Vibration Assisted Machining (VAM) Prior to 2000	
Cutting Force	References
General	
• thrust force is almost eliminated	3
• cutting (primary) force is reduced by half to a third over standard turning	3
1D Vs. 2D VAM	
• 2D “elliptical” vibration cutting forces are less than 1D vibration cutting forces	6, 7
2D VAM	
• forces are small enough for micro machining without loss of form accuracy	3, 7
Surface Characteristics	
• surface roughness is improved 3 ½ times over standard cutting	3
• reduction in the creation of burr, allows for machining of micro-scale parts	3, 6
• smooth and continuous chip is formed over wide cutting conditions	3

Materials <ul style="list-style-type: none"> materials that aren't turnable by stationary diamond tools but are by VAM (Ra < 50 nm) <ul style="list-style-type: none"> Optical Glass (1D – Resonate System) Steel (All Systems) Hardened (HRC 39) Steel (2D – Resonate System) Stainless Steel (1D – Resonate System) shear angle increases with cutting frequency 	4, 5, 6, 7, 8 7
Tool Wear <ul style="list-style-type: none"> correlation between diamond tool wear, effective tool / workpiece contact time and tool motion acceptable tool life on steel, 1500 m cut with Ra < 50 nm acceptable tool life on stainless steel, 1600 m cut with Ra < 26 nm tool life increased 4 to 5 times over standard turning over 1000 m tool life is longer for 2D cutting than it is for 1D cutting tool clearance angle needs to always be positive, requires larger angle than on std turning diamonds 	4 4 8 5 6 7

1.4 RESEARCH GOALS

Although significant results have been recorded (Table 1.1), the physics enabling these improvements is for the most part still unknown. The effect has been recorded, but the cause has yet to be quantified. Basic questions remain unanswered;

“Why are the forces reduced?”

“How does tool motion relate to surface finish?”

“What surface finish is possible with VAM?”

“What cutting speed will produce a benefit?”

“Why is diamond tool life increased?”

“What is the best servo design for a given application?”

The research described here is focused on answering these questions and quantifying the mechanisms by which the reported advantages take place. To this end, four areas will be addressed: servo mechanics, surface feature characterization, cutting forces and tool wear. To address each of these issues in more detail, the plan described below was developed.

1.4.1 Servo Mechanics

As discussed earlier, VAM path motion is either 1D or 2D. Moriwaki has shown that 2D vibration cutting produces lower cutting forces and longer tool life than 1D vibration

assisted cutting [6,7]. But what makes elliptical vibration cutting superior? What is the relationship between elliptical path, surface finish and tool forces? It is by understanding the dynamics and mechanics of an elliptically driven tool servo that these questions will be answered.

1.4.2 Surface Feature Characterization

Study of the cause and effect relationships involved in this machining process starts with the surface features that will be generated by the 2D elliptical path swept by the diamond tool. Surface feature characterization involves studying the chip shape, the effect of overlapping cutting / chip volumes, the effect of tool deflection and material deformation as well as the surface roughness based on tool path radii, velocity ratios and material properties.

1.4.3 Force Model

Establishing the cross-sectional geometry of the chip at any point in time thus allows for the prediction of tool cutting forces via a PEC developed model based on plasticity theory and shear angle [18]. Knowledge of the component forces vectors produced for a given chip shape on a particular material will allow for the combination of several research efforts (subsurface damage, temperature effects, etc.) and help establish a unified model of VAM and its application.

1.4.4 Diamond Wear of Subsonic Cutting

Knowing the forces produced and the surface that results from a given set of VAM operational parameters will help in the understanding of tool wear. The high quality of a diamond turned surface is accompanied by a high cost of tool ownership. Therefore being able to predict the life expectancy of a diamond tool for a desired surface finish on a given material is of great importance to industry.

CHAPTER TWO: ELLIPTICAL MOTION

2.0 DIAMOND TURNING BASICS

Initial investigation into vibration assisted machining focused on vibration assisted turning, a logical starting point given the high precision capability of modern day diamond turning machines [5, 6, 8]. A diamond turning machine (DTM) is a high precision version of a computer-numerically-controlled (CNC) lathe. The axis positioning capability is to within a few nanometers of the desired path. To minimize vibration effects, diamond turning machines employ sophisticated metrology systems as well as linear motors and air bearing spindles. These differences aside, the arrangement of tool and spindle on a DTM is identical to that of a standard metal lathe. Figure 2.1 illustrates this arrangement.

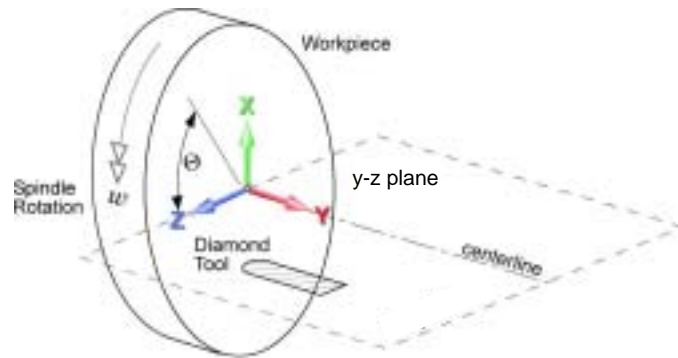


Figure 2.1: Tool / Workpiece Arrangement on a DTM

2.1 VAM BASICS: PROCESS TECHNOLOGY

Vibration assisted turning utilized single axis vibration mechanisms such as those described in Section 1.3.2. The basic components of such early devices were an ultrasonic transducer, typically a lead zirconate titanate (PZT) ceramic, an amplification horn and a diamond tool. The kinematics of such systems, and the basis for all vibration assisted machining, involves moving the diamond tool into and out of contact with the workpiece.

2.1.1 One Dimensional Vibration Assisted Machining

During the turning operation on a three-degree of freedom (y, z, θ) DTM, the conventional planer motion of the tool created by the articulation of the y and z axes in relation to the workpiece and the spindle (Figure 2.1), is supplemented by an independent tool motion. As pictured in Figure 2.2, the tool motion is parallel to the surface of the workpiece and in the direction of the cut.

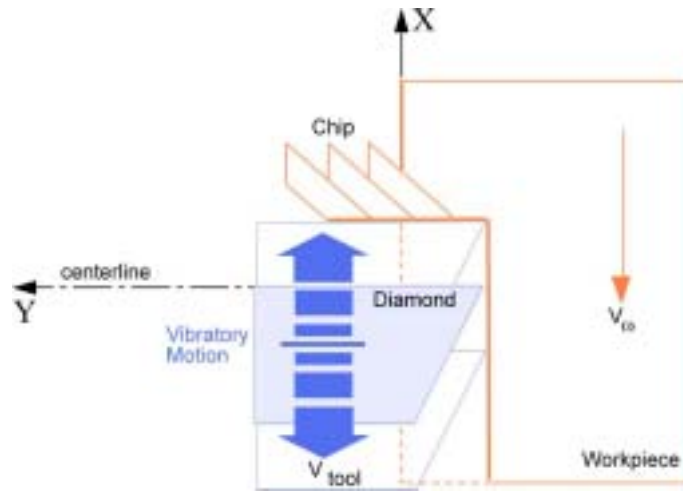


Figure 2.2: 1D Vibration Cutting

Assume that the tool velocity is an order of magnitude greater than the tangential velocity of the workpiece. The position of the tool at any point in time with respect to the centerline, as pictured in Figure 2.2, can be written mathematically as,

$$x(t) = A \cos(\omega_{drivefreq} t) \quad (1)$$

with,

$$\omega_{drivefreq} = 2\pi F_{drive} \quad (2)$$

where A is the amplitude, $\omega_{drivefreq}$ is the oscillation frequency in radians per second and F_{drive} is the frequency in Hz of the PZT transducer. The velocity of the diamond tool is then found by differentiating Equation (1) with respect to time.

$$\frac{d}{dt}x(t) = v_{tool} \quad (3)$$

$$v_{tool} = \omega_{drivefreq}A \cos(\omega_{drivefreq}t) \quad (4)$$

The tangential velocity, v_{ω} , of the workpiece at a given radius from the center of the spindle, $r_{spindle}$, can be described by,

$$v_{\omega} = \omega_{spindle}r_{spindle} \quad (5)$$

where $\omega_{spindle}$ is the rotational velocity of the spindle in radians per second. Taking a macroscopic view of the system shown in Figure 2.2, the total cutting velocity, v_{total} , during the machining operation is a summation of both the tangential velocity of the workpiece, v_{ω} , and the oscillating velocity of the diamond tool, v_{tool} .

$$v_{total} = v_{\omega} + v_{tool} \quad (6)$$

The component parts of the total velocity, v_{total} , are what distinguish standard diamond turning from vibration assisted diamond turning. In fact VAM is more akin to milling or flycutting, with its independent part and tool speeds, than to turning.

To transition from standard cutting to vibration assisted machining, the tool must break contact with the part by having a velocity greater than and opposite in direction to the part velocity. Although the magnitude of the tool velocity needs only to be greater than

the part velocity for the cycle to take effect, the larger the separation, the more accurate equation (1) is to predicting the tool location. Chapters 3 and 4 will show that a greater velocity ratio between the tool and the part is accompanied by reduced machining times.

Having established the component velocities of one-dimensional VAM, the relative directions and magnitudes of these two velocity components and the effect they have on the length of contact between the tool and the workpiece have been used to construct a cutting cycle for vibration assisted machining. This cycle is presented in Figure 2.3.

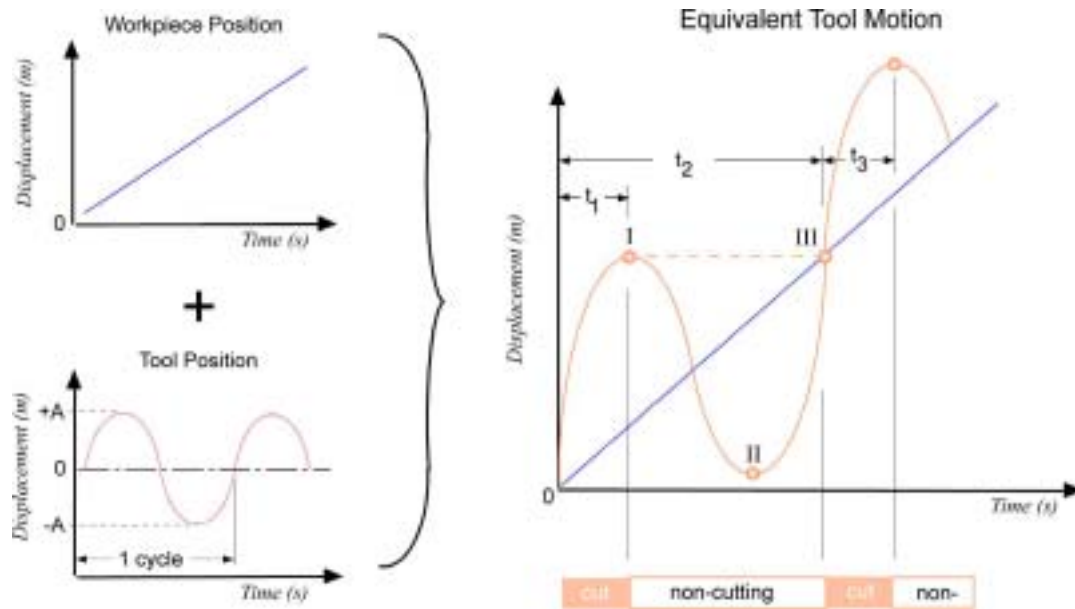


Figure 2.3: Cutting Cycle for Vibration Assisted Machining (VAM)

Starting at time equals zero, the diamond tool and workpiece are in contact. The instant that time begins, the workpiece, rotated by the spindle, is displaced at a uniform velocity. In Figure 2.3, this is depicted as a diagonal line with a constant slope starting at the origin and extending to infinity. Since the slope of this displacement line never changes, the velocity is constant. Between times zero and t_1 (on the right hand side of Figure 2.3), the tool displaces an amount greater than the part. During this time, the velocity of the tool

exceeds the constant velocity of the part. The physical interpretation of this relative motion is the tool moving into the workpiece to produce a chip (Figure 2.4). At the point labeled I ($t = t_1$) in Figure 2.3, the slope of the displacement curve (or velocity) goes to zero. Just after this point the direction of the tool velocity vector changes to a negative value and the tool retracts from the workpiece. The tool proceeds opposite to the motion of the part until point II when the velocity changes sign and the tool moves back toward the part. Contact is reestablished at point III and the cycle repeats. Figure 2.4 provides a snapshot pictorial of the critical points in the 1D VAM cutting cycle.

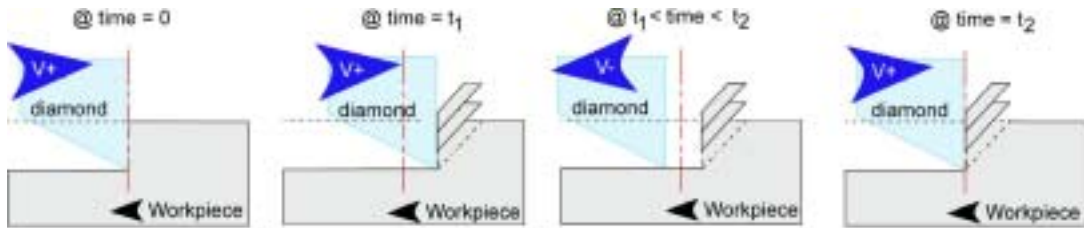


Figure 2.4: Contact Snapshot

2.1.1.1 Duty Cycle for One Dimensional Cutting

The amount of time that the rake face (Figure 2.5) of the tool, is in contact with the workpiece needs to be quantified. The percentage of contact time is referred to as the “Duty Cycle” for 1-D VAM. While the duty cycle concept was mentioned in the Fraunhofer study [5], the implementation of the process has yet to be explored.

In standard diamond turning, the duty cycle is 100 % since the tool never leaves contact with the workpiece. Not until $v_{tool} > v_{\omega}$ in magnitude and opposite in direction when the tool disengages from the part does the percentage start to drop. The duty cycle can be defined mathematically as,

$$DC = \frac{t_{period} - (t_{leave} - t_{enter})}{t_{period}} \quad (7)$$

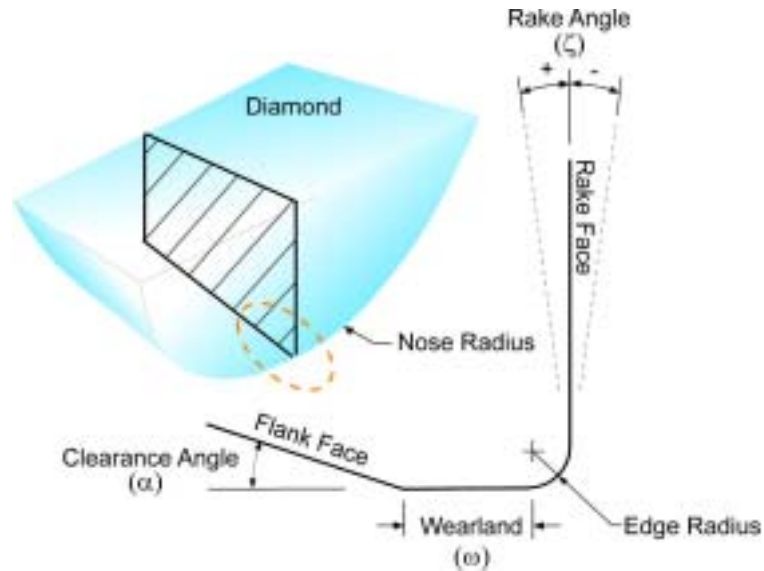


Figure 2.5: Diamond Cross-Section

where,

$$t_{period} = \frac{2\pi}{\omega} = \frac{1}{f} \quad (8)$$

t_{enter} is the time in seconds when the tool rake face makes contact with the part, and t_{leave} is the time at which the tool rake face breaks contact with the newly created chip. Noting that the duty cycle is a function of contact time and that contact time is dependant on the velocity ratio between the tool and the workpiece, a program (see Appendix A) was written to calculate the percentage contact times or duty cycle for velocity ratios from 0 to 1. The output of this program is plotted as Figure 2.6. The ratio of the workpiece velocity to the tool velocity is called the Horizontal Speed Ratio (HSR).

$$HSR = \frac{v_w}{v_{critical}} \quad (9)$$

Where v_w is the workpiece velocity, defined by Equation (5) for turning applications and $v_{critical}$ is the maximum tool velocity derived from Equation (4).

$$v_{critical} = v_{tool} = \omega_{drivefreq} A \cos(0) = 2\pi F_{drive} A \quad (10)$$

The duty cycle forms the base for calculating the theoretical surface roughness, cutting / thrust force and tool wear. How these factors are controlled by the duty cycle will be addressed in Chapters 3 and 4.

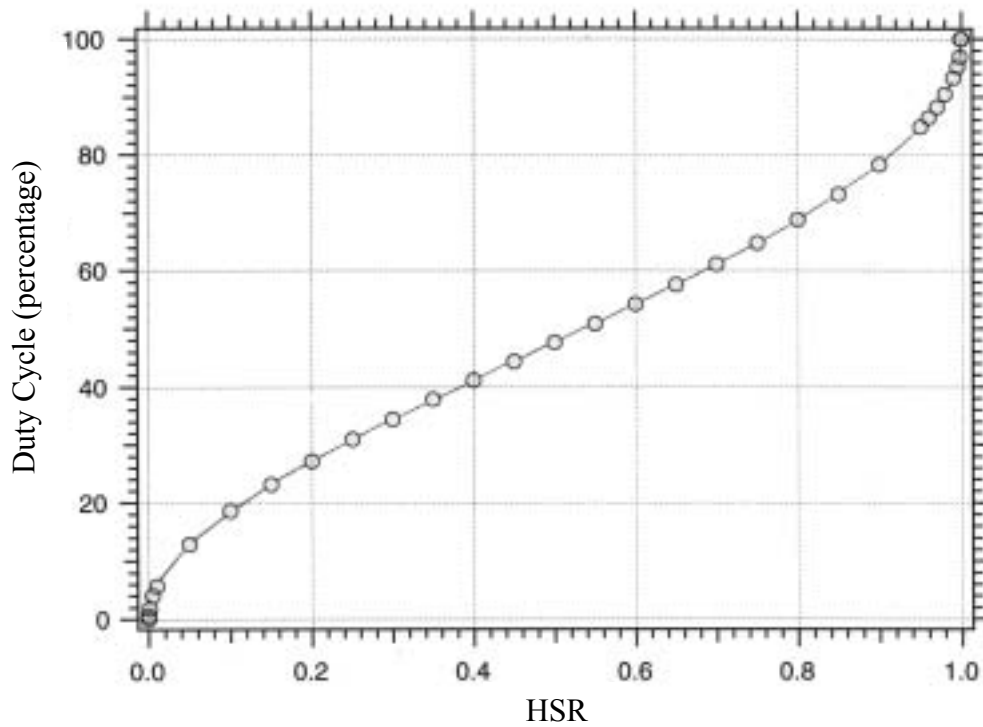


Figure 2.6: 1D Duty Cycle Chart

2.1.2 Two Dimensional Vibration Assisted Machining

The addition of a sinusoidal y-axis displacement to that of the 1D x-axis displacement results in the tool tracing an elliptical tool path. The mathematical equation of an ellipse is,

$$\frac{x^2}{a^2} + \frac{y^2}{b^2} = 1 \quad (11)$$

where x is the x-axis displacement of the tool, originally defined in Equation (1),

$$x = A \cos(\omega_{drivefreq} t) = a \cos(\omega_{drivefreq} t) \quad (12)$$

and y is the y-axis displacement of the tool.

$$y = b \sin(\omega_{drivefreq} t) \quad (13)$$

The terms a and b in Equations (12) and (13) are the major and minor axis of the ellipse respectively. The axial components of an ellipse are illustrated below in Figure 2.7.

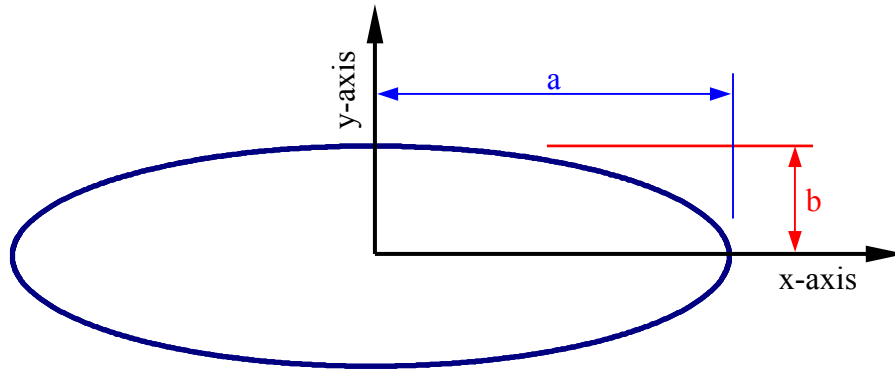


Figure 2.7: Ellipse

Two dimensional vibration assisted machining, as 1D VAM, can be expressed in terms of horizontal displacement, x , by solving Equation (10) for y in terms of x .

$$y(x) = \pm \sqrt{\left[1 - \left(\frac{x^2}{a^2}\right)\right]} b \quad (14)$$

All vibration assisted machining involves bringing the tool into and out of contact with the workpiece. In 1D VAM the contact is broken between the rake face of the tool and the workpiece while the wearland maintains continuous contact. In 2D all surfaces of the

tool disengage from the workpiece. 2D VAM can be modeled as a series of overlapping ellipses. This is illustrated in Figure 2.8.

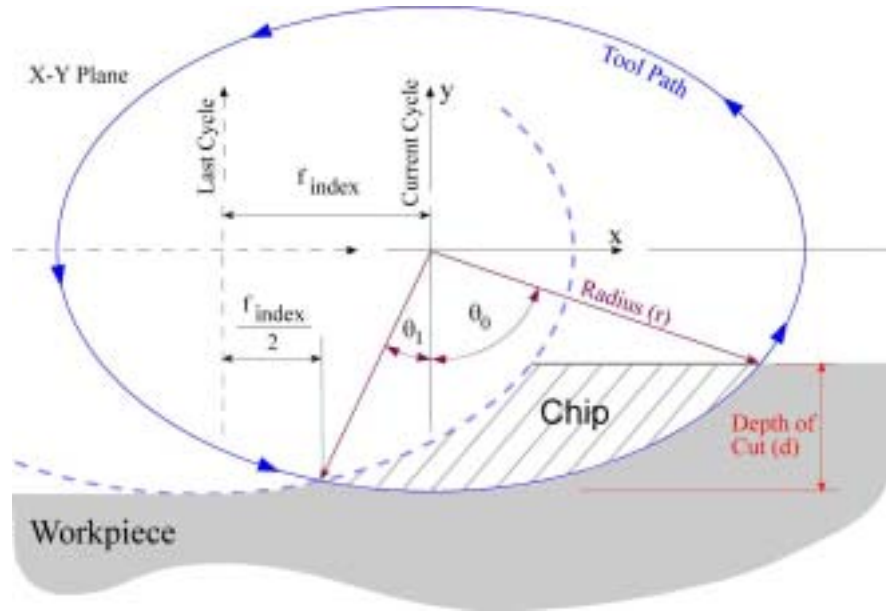


Figure 2.8: Basic 2D VAM – Overlapping Ellipses

The amount the elliptical tool paths overlap is a result of the distance indexed between cutting cycles. This index distance is defined as,

$$f_{index} = 2 \cdot \pi \cdot a \cdot HSR \quad (15)$$

where HSR is the horizontal speed ratio defined in Equation (9) and a is the major axis of the ellipse. The intersection point on the surface of the workpiece is half the index distance.

2.1.2.1 Duty Cycle for Two Dimensional Cutting

Whereas the duty cycle for 1D VAM was defined as the percentage of time that the rake face maintains contact with the workpiece, 2D VAM defines the duty cycle as the percentage of the elliptical path that the tool is in contact with the workpiece. Changing from time of contact to distance of contact simplifies the study of tool wear.

The 2D duty cycle is found by comparing the length of tool/workpiece contact in the xy-plane to the total perimeter of the elliptical tool path. Referring back to Figure 2.8, the contact length is that part of the tool path swept over angles θ_1 and θ_2 . The angles are defined by,

$$\theta_1 = \sin^{-1} \left(\frac{\frac{f_{index}}{2}}{a} \right) \quad (16)$$

$$\theta_2 = \cos^{-1} \left(1 - \frac{d}{b} \right) \quad (17)$$

where d is the depth of cut and a and b are the major and minor axis of the ellipse respectively. The radius of curvature, ρ , is used to approximate the radius of the ellipse, r . The radius of curvature is defined as,

$$\rho(x) = \frac{\left[1 + \left(\frac{d}{dx} y(x) \right)^2 \right]^{\frac{3}{2}}}{\frac{d^2}{dx^2} y(x)} \quad (18)$$

Used in conjunction with the total angle swept by the tool during which material is removed, the length of contact can be calculated.

$$L_{contact} = \rho(\theta_1 + \theta_2) \quad (20)$$

The 2D duty cycle is then derived by comparing the length of contact, $L_{contact}$, to the perimeter of the ellipse, $L_{ellipse}$.

$$L_{ellipse} = 2\pi\rho \quad (21)$$

$$DC_{2D} = \left(\frac{L_{contact}}{L_{ellipse}} \right) \cdot 100 \quad (22)$$

Figure 2.9 plots the duty cycle as a function of the HSR and the ratio of the depth of cut to the minor axis of the ellipse.

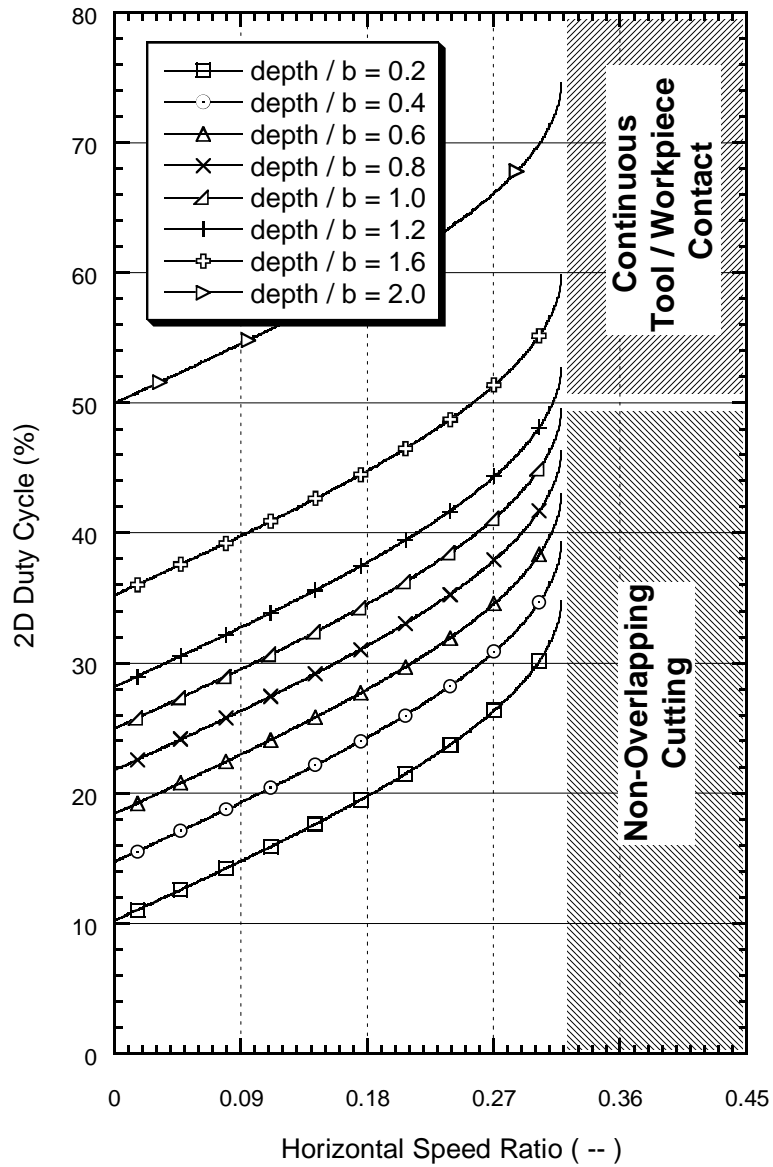


Figure 2.9: 2D Duty Cycle Chart

In 2D VAM, the depth of cut is typically less than the minor axis of the ellipse ($depth/b < l$ in Figure 2.9). As will be shown in Chapters 3 and 4, this is because a lower duty cycle correlates with a reduction in cutting force and increased tool life. The HSR, while also influencing the machining forces and tool life, controls the theoretical surface roughness of the finished part by increasing the amount of tool path overlap, i.e. a small f_{index} . As the HSR increases the amount of overlap diminishes until it is zero at $HSR = 0.32$. This is characterized in Figure 2.9 as the “non-overlapping” region. If the HSR is held greater than 0.32 and the depth of cut is made larger than the minor axis the “continuous contact” region is entered. In this region, the tool never breaks contact with the workpiece and by definition; VAM is no longer in effect.

2.2 SERVO MECHANICS: PEC ULTRAMILL

Having established the rudimentary principals of VAM, it is important to study the mechanics behind the tool’s oscillatory motion because tool motion is the key to VAM. Based in part on previous studies that reported lower cutting forces and greater tool life of 2D vibration machining over 1D vibration machining (see Table 1.1), a 2D “elliptical” servo was developed at the PEC.

The PEC elliptical servo falls within the non-resonant class of servo designs. For research purposes of analysis and control of the elliptical motion, a low-speed servo with an operation bandwidth was developed. Bandwidth is the frequency span over which a servo is able to operate at full stroke. Resonate systems operate at a single frequency, thus their



Figure 2.10: UltraMill-LS Reflected in a Turned Aluminum Sphere

bandwidth is zero. Non-resonant systems are capable of operating from DC to 80% of the servo's first natural frequency. This servo was designated the UltraMill-LS (UMLS) and is pictured in Figure 2.10.

2.2.1 Components

Figure 2.11 illustrates the component parts of the UltraMill. A steel frame (A) capable of mounting on both a vacuum chuck and micro-height adjustable tool post forms the base of the UltraMill-LS. Enclosed within the base is a cam mechanism used to apply approximately 10 lbs of tension to a 0.010" diameter music wire (B) that serves a two-fold purpose. One is to preload the piezoelectric ceramic stacks and the other is to keep the head firmly seated on the stack ends while it undergoes the rapid acceleration changes associated with the UMLS motion. Two 44-layer piezoelectric actuators (C) form the engine of this tool servo. These 6.35 mm diameter stacks measuring 25.4 mm in overall length are each capable of producing 22 μm of displacement at 1000 volts. Seated on the end of each piezoelectric stack is a 6 mm long, 1.58 mm diameter half round hardened

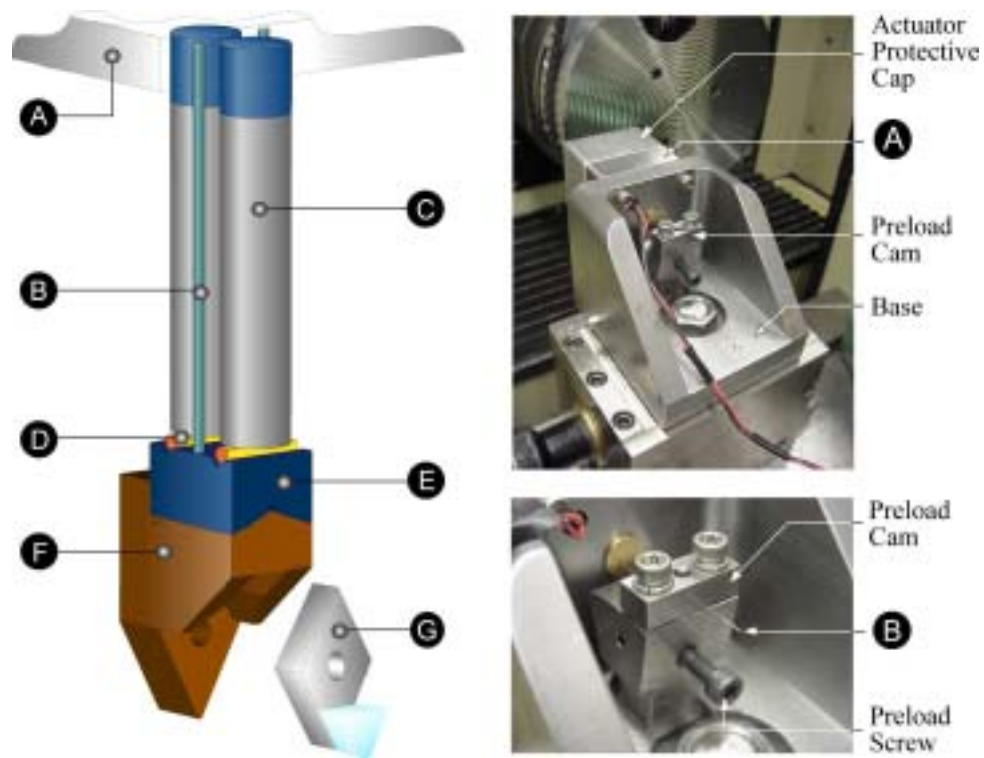


Figure 2.11: Low Speed Prototype

steel pivot pin (D). That mates to a v-notched groove in the tool head mount (E). Utilizing a three sided seat arrangement for precise realignment without over constraint, the mount connects to the tool head (F). The tool head is machined out of 6061-T6 aluminum and accepts diamond shaped tool inserts (G).

2.2.2 Linkage Motion

The UltraMill produces a cyclical elliptical cutting motion that resides in the 2D space of the x-y plane. The basis of the ellipse can be found in the UMLS’s linkage system shown in Figure 2.12.

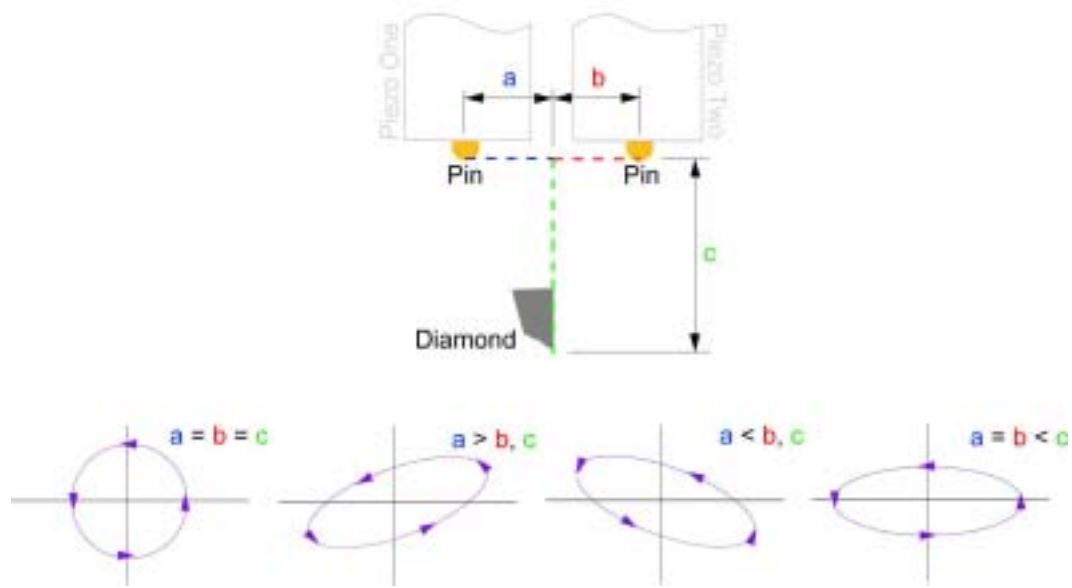


Figure 2.12: Linkage and Path Shapes

Assuming the linkage arms “a”, “b” and “c” are equal, driving the piezo stacks 90° out of phase with respect to each other will result in the tool traversing a circular path. By varying the relationship between the arms, the path can be modified. Referred to as a “T” shaped linkage, holding the trunk of the “T” or arm “c” constant and adjusting the relationship between arms “a” and “b” will result in tilting the path. Equating the lengths “a” and “b” while elongating arm “c” generates a level elliptical path.

The direction of the travel shown in Figure 2.12 is counter-clockwise or forward. However, forward or reverse is controlled by which piezo actuator receives the $+90^\circ$ phase addition to its supply voltage. In the case of forward motion, the second stack, denoted “Piezo Two” in Figure 2.12, receives the phase adjustment. Referring back to Figure 2.10, “Piezo Two” is also designated the “red” stack.

Since piezoelectric ceramics vary almost linearly with voltage, the motion of the end of the stack, P , can be modeled with a cosine function.

$$P_1 = A \cos(\omega t) \quad (23)$$

$$P_2 = A \cos(\omega t + \phi) \quad (12)$$

Coupled with the “T” linkage, the component position location Δx and Δy , can be calculated. β describes the amount of tilt between the two stacks.

$$\beta = \frac{P_2 - P_1}{a + b} \quad (13)$$

$$\Delta x = c \times \beta \quad (14)$$

$$\Delta y = \frac{P_1 \times b + P_2 \times a}{a + b} \quad (15)$$

Figure 2.13 reveals the theoretical tool path of the UMLS with $a = b = 3.150$ mm and $c = 22.962$ mm. Due to the phase shift, only 70% of the piezo stack elongation is exhibited in the y-axis displacement. This varies from 100% at 0° phase separation to 0% at 180° separation. This reduction in stroke is illustrated in Figure 2.14. As the phase difference between the two motions increases, the intersecting points, I_1 and I_2 , which bound the maximum ΔY displacement, approach one another. When the relative phase shift is 180° , the intersection points lie on the same horizontal line, thus ΔY is zero.

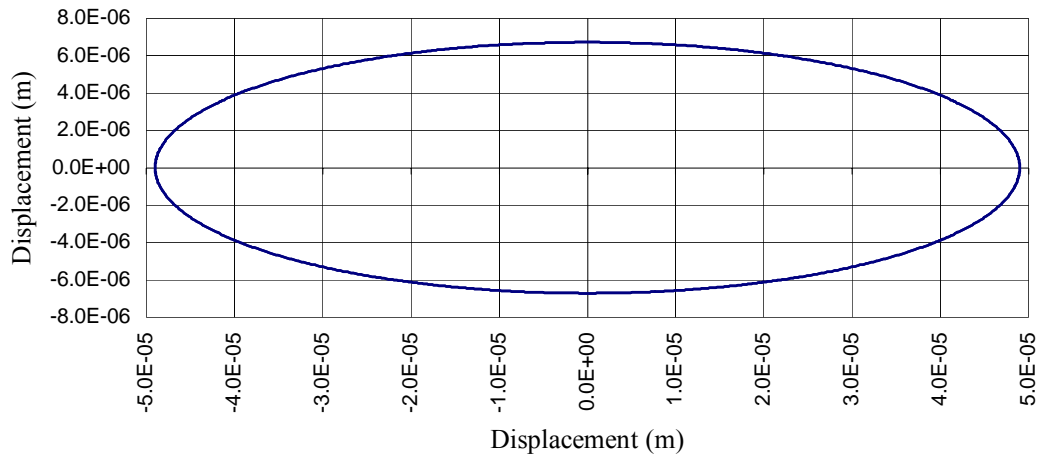


Figure 2.13: Calculated Elliptical Tool Path of UMLS

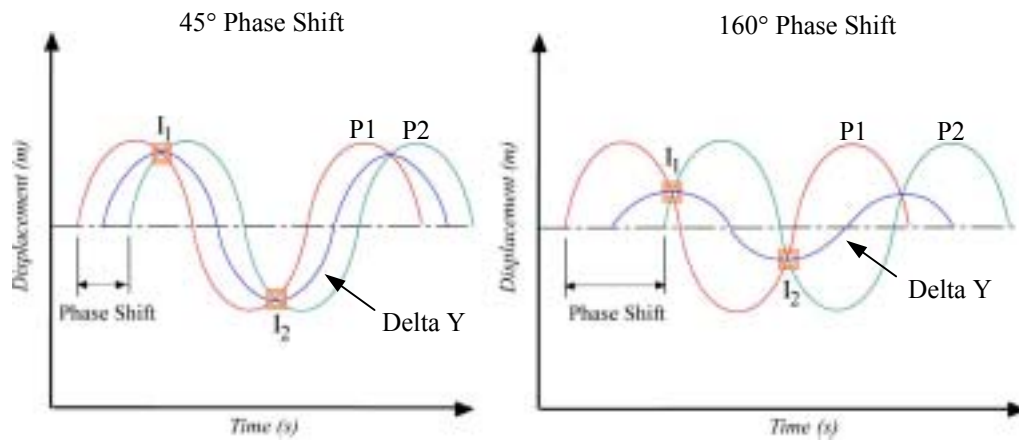


Figure 2.14: Y-axis Relationship to Phase Separation

2.2.3 Support Equipment

The signal to the PZT actuators of the UMLS tool servo are generated by a HP[®] 8904 multi-function synthesizer, which is capable of not only supplying a uniform cosine wave to each stack but also providing the 90° phase shift between the two. The ± 4 -volt sinusoidal output of the synthesizer is summed with a 4-volt dc source using a Kepco[®] PCX 40-0.5 voltage regulator. This is done to shift the signal upwards, producing a 0 to +8 volt swing and avoiding negative voltage that would damage the stacks. The supply

voltage is then amplified 100x by routing the signal through a Trek[®] model 50/750 amplifier.

2.2.4 Path Measurement

System behavior is broken into two categories: motion and natural frequency. The path motion of the UMLS was measured by replacing the diamond insert with a specially constructed reflective insert that conformed to the same weight, thickness and length specifications of a 1 mm diamond insert. Weight was a critical factor because this same reflector would be used for measuring the natural frequency of the system (covered in Section 2.2.5). Agreement in length and thickness were important to correctly measure the displacement of the cutting tip. A dual channel fiber-optic displacement gage (Opto-Acoustics[®] Angstrom Resolver[®]) with nanometer resolution was used to decompose the tip motion into its x and y components. The two light probes were aligned perpendicular to each other and focused on the location where the diamond tip would reside. This arrangement is pictured in Figure 2.15.

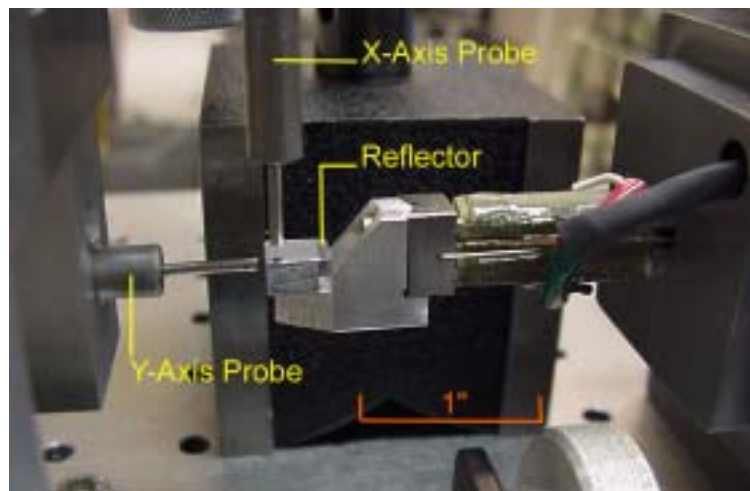


Figure 2.15: Motion Measurement Set-up for UMLS

Driving the stacks with their normal 800-volt signal, the output of the optical gauges was recorded on a Stanford Research Systems[®] Model 780 Spectrum Analyzer. The result of one of these tests is presented in Figure 2.16. The shifted minor axis peak of this

particular assembly is due to a slight difference in the stack properties: elongation and hysteresis. The tilt is a result of small differences (5-10 μm) in the overall lengths of the two stacks. Despite the minor variance from the ideal waveform, the tool path is acceptable for cutting purposes. The directional notes on the motion plot help to orient the ellipse to how it would be during actual cutting. Front refers to the part of the ellipse that would be involved in material removal, i.e. chip formation (see Figure 2.4). The part of the ellipse labeled “bottom” would be the portion in contact with the workpiece surface. Therefore, it is the shape of the ellipse in the 4th quadrant or “cutting zone” that is of most importance.

Depending on preload, stack lengths and the alignment of the various components, the measured shape of the tool path will differ slightly from a true ellipse between assemblies. After each build of the UMLS, the tool path was measured. The path was then measured after a series of cutting trials. On average, the path was found to vary from its pre-cutting path by less than 2% after 40 hrs of continuous duty.

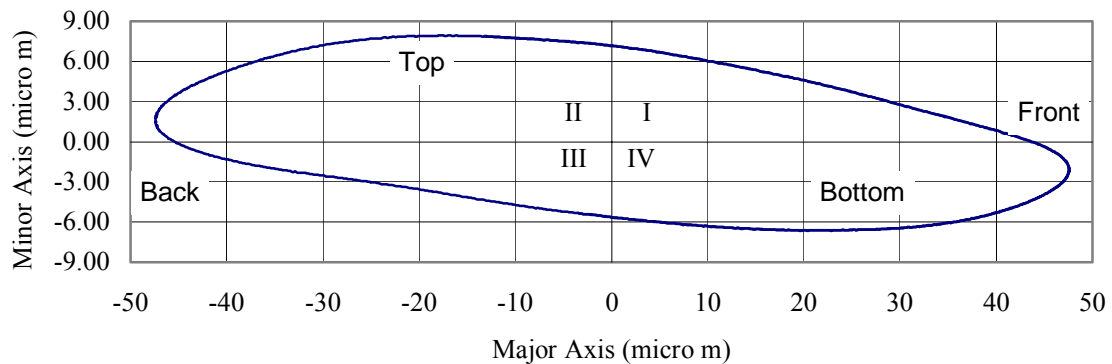


Figure 2.16: Tip Motion of UMLS (Below 1st Natural Freq.)

2.2.5 Natural Frequency and Operational Parameters

Since this is a non-resonance system, the maximum operating frequency is set by the 1st natural frequency of the system. Using the same arrangement and equipment as in the path measurement, the natural frequency was recorded by replacing the standard dual 8-volt drive signals with a single swept sine wave signal into one of the PZT stacks. Initial

comparative testing showed less than a 1% deviation in system response for excitation of either piezoelectric stack. The results of this testing, listed in Table 2.1, put the first natural frequency at 525 Hz. The first mode shape involved both stack elongating in unison. Due to the alignment of the stacks on the base of the tool head mount (Figure 2.11), this caused the head assembly to move back and forth in the x-z plane. The 2nd natural frequency saw the stacks oscillating 180° out of phase with respect to each other. As predicted in Section 2.2.2, the phase separation resulted in the head assembly rotating with no y-axis displacement. The upper limit of the UMLS was set to 400 Hz to stay away from the effects of the first mode shape.

*Table 2.1: UMLS Operational Parameters for Build
Shown in Figure 2.16*

Operational Parameters		
Bandwidth	0 – 400	Hz
Drive Voltage	0 – 800	VAC
Active Mass	7.2	grams
Natural Frequency		
1 st (out of plane)	525	Hz
2 nd (rotational)	700	Hz
Motion		
Major Axis	47.501	μm
Minor Axis	7.295	μm
Tilt of Ellipse	-2.411	°
Axis Ratio	6.51	--

CHAPTER THREE: DEVELOPMENT OF ELLIPTICAL MODEL

3.0 SURFACE TOPOGRAPHY

The end product of vibration assisted machining is the result of two independent motions. These two motions plus the tool nose radius produce the three dimensions, or topography, of the workpiece surface. Two of the dimensions are captured in the surface roughness equation of standard single point turning,

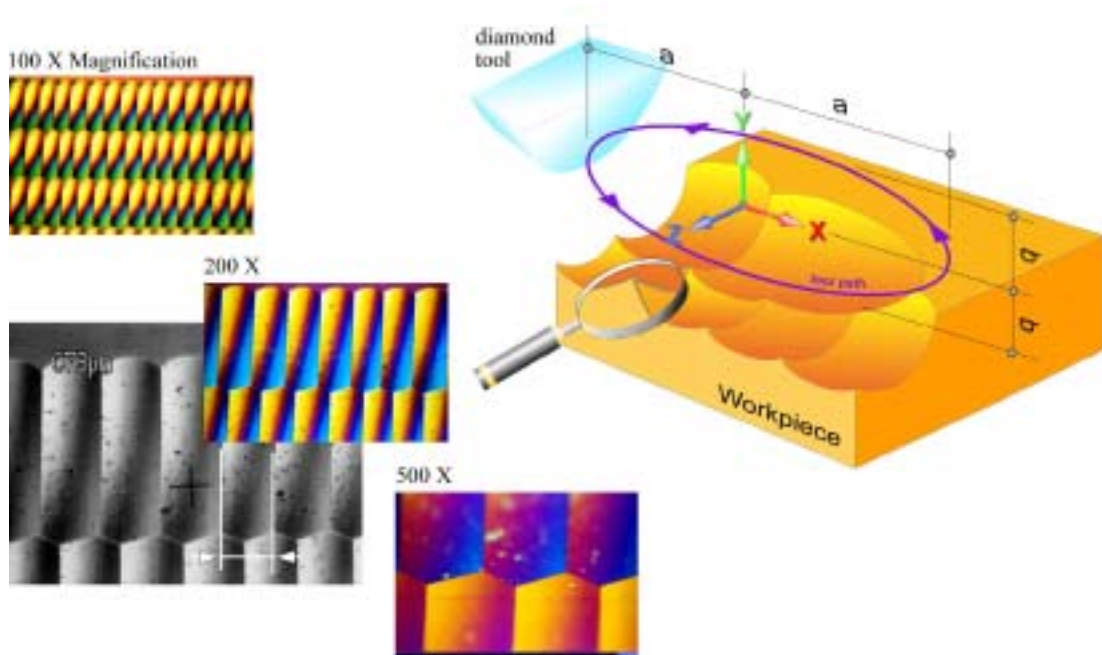
$$Rt_{zy} = \frac{f^2}{8R} \quad (16)$$

where Rt_{zy} stands for the Peak-to-Valley surface roughness, f is the cross-feed or rate at which the tool is moved in the z-y plane across the surface of the turned part given in distance per revolution and R is the nose radius of the diamond tool. The surface roughness of third dimension is an artifact of the shape and the amount of overlap between successive elliptical paths. Defined by Equation (17),

$$Rt_{xy} = \frac{bf_{index}^2}{8a^2} \quad (17)$$

it predicts the roughness in the x-y plane. The terms b and a are the minor and major axis elliptical tool path. f_{index} , defined by Equation (15), is the x-axis distance indexed between cutting cycles.

For both standard turning and 1D vibration machining, the tool never breaks contact with the workpiece surface and material removal is accomplished through plowing and shearing the material away from the workpiece. For 2D VAM, contact with the surface is intermittent and material is removed through what can best be described as a scooping motion illustrated in Figure 3.1. Also shown in Figure 3.1 are surface magnifications of an aluminum surface turned with the UMLS. The details of this surface features will be explained later in this Chapter.



*Figure 3.1: Resultant Surface Finish via “Scooping” Motion
 (1000 Al, UM frequency = 55 Hz, Diamond Nose Radius = 1 mm, Spindle
 Speed = 2 rpm, Part Radius = 22 mm)*

3.1 CHIP SHAPE

The topography of the vibration turned surface is a result of overlapping chip segments. Superimposing two ellipses can approximate the geometry of each chip and the surface features caused by its removal. The elliptical tool path was defined in Equation (11) where x and y are the displacements in the x - y plane and a and b are the respective major and minor axis of the tool path set by the servo design.

$$\frac{x^2}{a^2} + \frac{y^2}{b^2} = 1 \quad (11)$$

The use of Equation (11) assumes the forces generated during actual cutting do not distort the tool path and that the distance indexed per cycle is small compared to the major axis of the ellipse ($f_{index} \leq 25\%$ of $2b$).

3.1.1 Controlling Parameters

The parameters that control the size and shape of the chip removed per cutting cycle are the following,

- Ellipse shape (major and minor axis)
- Depth of cut
- Cross-Feed (f)
- Up-Feed (f_{index})
- Radius of tool

The ellipse shape is set by the tool trajectory and establishes the outer edge of the chip. The second parameter, depth of cut, determines the point during the ellipse at which the tool disengages from the workpiece. The depth of cut is also responsible for determining if the chip is continuous or segmented. When the depth of cut is such that the workpiece surface is “below” the centerline of the ellipse, a segmented or “Class B” chip is formed. Conversely, when the surface is “above” the centerline of the ellipse, a continuous chip results. This type of chip is defined as a “Class A” chip. Figure 3.2 illustrates the two classes of VAM chips.

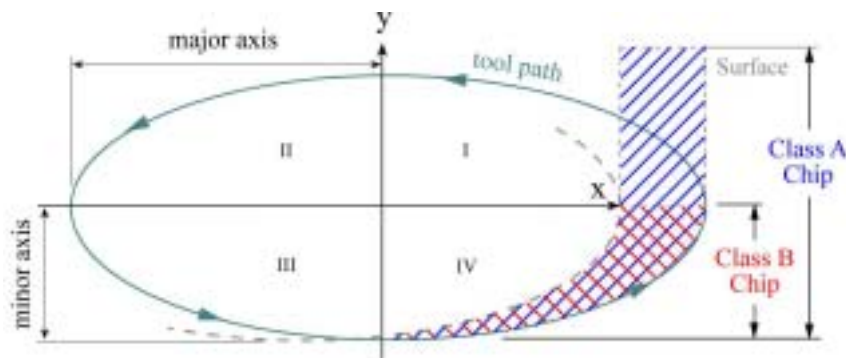


Figure 3.2: Chip Classification

The up-feed establishes the amount by which two consecutive elliptical cycles overlap. Up-feed is the distance per cycle that the ellipse is indexed or moved forward. In combination with the depth of cut, it determines the starting point of the current chip. With this information, the upper boundary, set by the previous cut, and lower boundary, set by the current cut, are known for every point in the x-direction. Thus subtracting the two provides the chip thickness in the x-y plane. Tool radius adds the third dimension. Knowing the chip thickness at each point in the cutting cycle, the tool radius sets the width and establishes the x-z cross-section of the chip.

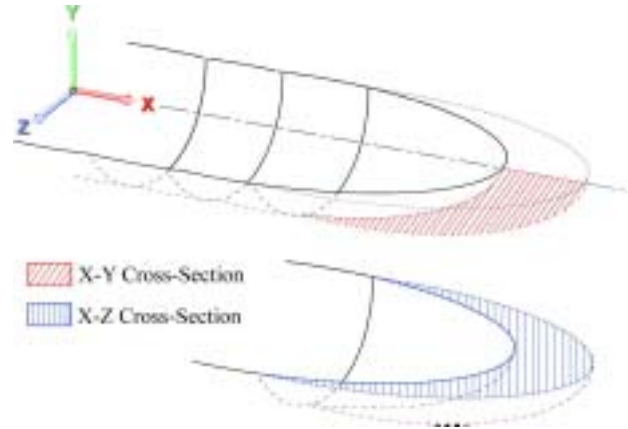


Figure 3.3: Chip Cross-Section

Figure 3.3 shows the chip cross-section for an in-line cut. This means that overlapping of chip segments takes place only in the x-direction assuming that the cross-feed is equal to zero. This is typically not the case since most applications call for a surface to be produced and not simply a groove. Cross-feed, f , is the distance by which individual rows overlap, just as in standard metal turning. Cross-feed will reduce the volume of material removed per cutting cycle and change the surface roughness. As a result, the forces produced during vibration assisted turning are reduced when compared to the straight-line cutting example illustrated in Figure 3.3. The effect that cross-feed has on surface finish will be addressed in Section 3.2.

3.1.2 Projected Tool Shape

In a turning arrangement, such as that illustrated in Figure 2.1, the radial distance from the part center to the tool is far greater than the major axis displacement of the oscillating tool (47.5 μm for the UMLS). The major axis displacement or tool swing can be considered stationary for the purpose of determining the theoretical surface roughness for the majority of the turned surface. However as the tool approaches the center of the part, the part radius falls to within the same order of magnitude as the major axis tool swing. In this case, the tool can no longer be taken as stationary and the nose radius a constant. Figure 3.4 shows the apparent increase in nose radius at the part center.

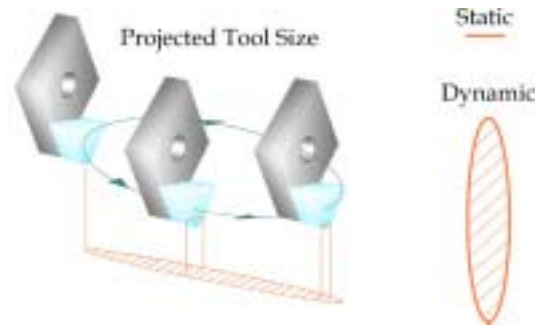


Figure 3.4: Projected Tool Size

The contact line, a function of the nose radius and depth of cut, of a stationary diamond is labeled in Figure 3.4 as “static.” The static contact area is only a fraction of that of the “dynamic” contact area, Figure 3.4, resulting from the elliptical motion of the oscillated tool. The projected tool size serves to reduce surface roughness at the center of turned parts just as if the nose radius of the tool were increased. It does so by knocking off the previous row’s peaks as the part radius gets smaller.

3.2 PHASE

In addition to having the advantage of lowering the cutting force per cycle, cross-feed produces a surface feature relationship called phase. Phase is the alignment of one row’s features to that of its neighbors and is controlled by the ratio of the up-feed to the cross feed.

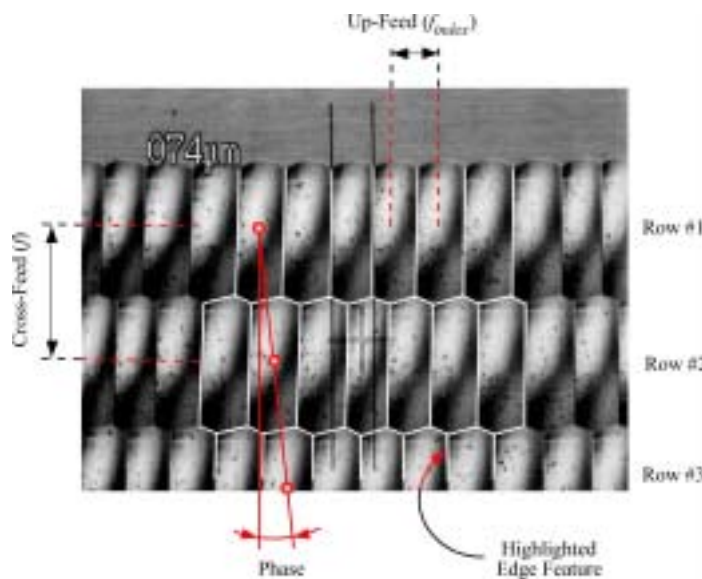


Figure 3.5: Row Alignment ~ Phase

Figure 3.5 is a close-up look at a vibration cut aluminum surface. Note the highlighted boundaries between the individual rows. The “zigzag” pattern of the row edge is a result of phase offset between rows. Figure 3.6 illustrates phase the benefits of manipulating it for a reduction in overall surface roughness, $R_{t,xyz}$.

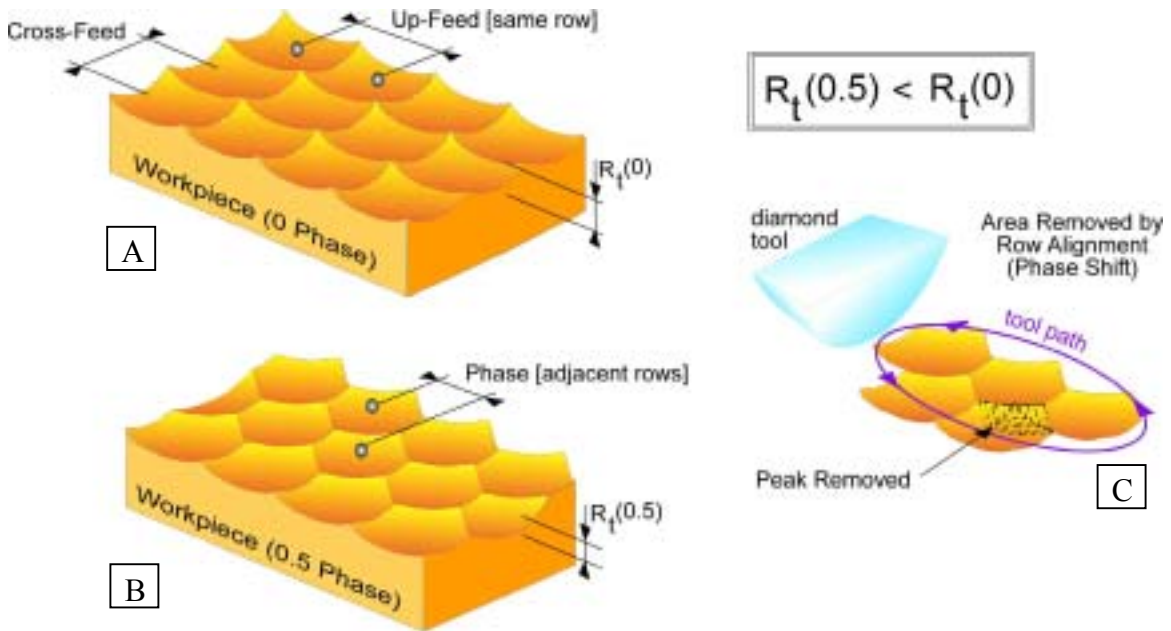


Figure 3.6: Surface roughness and Phase

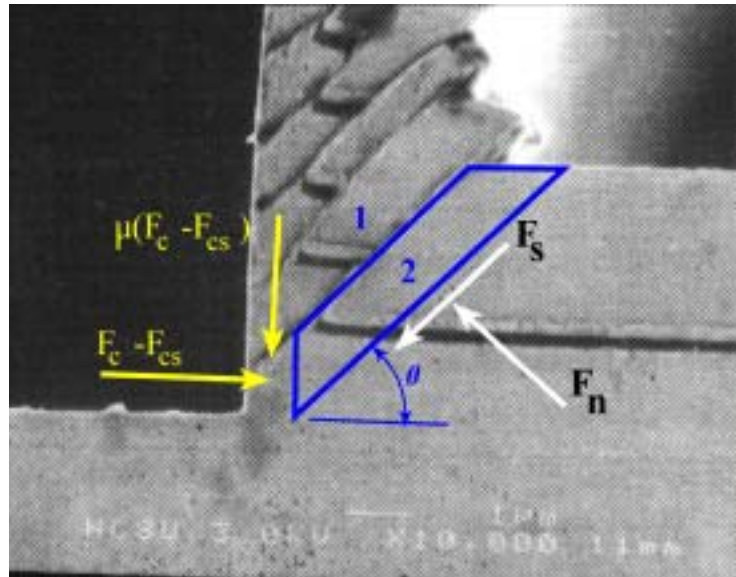
Phase can range between 0 and 0.99. Shown in illustration A of Figure 3.6, a phase value of 0 results in surface feature alignment of consecutive rows. To produce a surface with 0 phase requires both a uniform up-feed, f_{index} , between rows and the matching of tool/workpiece inception points. Maintaining a uniform up-feed while shifting the inception point results in a phase shift. Illustration B of Figure 3.6 shows a part with a phase of 0.5. Controlling the phase alignment of rows can result a lower surface roughness. Seen in illustration C of Figure 3.6, the sweep of the tool in a phase shifted row results in the tool removing the peak of preceding row that would have remained if the phase shift were 0. Since phase manipulation does not require adjustment to the horizontal speed ration (HSR), surface roughness can be reduced without a reduction in machining time by controlling phase.

3.3 LINEAR CUTTING MODEL

The elliptical cutting model is based on a linear model developed by Dr. Christopher Arcona while at the Precision Engineering Center [18]. Figure 3.7, is a SEM image of the root of the chip. Segment 1 is the shear band just created, while segment 2 is the shear band that will form when the tool is indexed another $0.7 \mu\text{m}$ forward. Overlaid on this image are the forces acting on cross section 2. The total cutting force acting on the tool is F_c . F_{cs} is the force associated with the sliding of the tool over the workpiece. F_s and F_n are the component forces acting at a shear angle of ϕ on the shear zone. Lastly, μ is the coefficient of friction between the diamond face and the chip. Performing a force balance on element 2 results in equations for the cutting force and thrust force.

$$F_c = F_s \cos(\phi) + F_n \sin(\phi) + F_{cs} \quad (18)$$

$$F_t = \mu(F_c - F_{cs}) + Ft_{sliding} \quad (19)$$



*Figure 3.7: Cross-Section of Plated Copper Chip
w/ Segment and Forces Overlaid*

The coefficient of friction at the tool/chip interface; μ , can be calculated from the summation of forces in the vertical direction. The result is Equation (20)

$$\mu = \frac{\cos(\phi) - \frac{\sin(\phi)}{\sqrt{3}}}{\frac{\cos(\phi)}{\sqrt{3}} + \sin(\phi)} \quad (20)$$

If the material hardness, H , and either the shear angle, ϕ , or the coefficient of friction, μ , is known, the tool forces can be calculated. Written in terms of cutting conditions and material data, the tool forces are given by,

$$F_c = \frac{HA_c}{3} \left(\frac{\cot(\phi)}{\sqrt{3}} + 1 \right) + \mu_f \sigma_f A_f \quad (21)$$

$$F_t = \mu \left[\frac{HA_c}{3} \left(\frac{\cot(\phi)}{\sqrt{3}} + 1 \right) \right] + \sigma_f A_f \quad (22)$$

$$\sigma_f = 0.62H \sqrt{\frac{43H}{E}} \quad (23)$$

with A_f equal to the area of friction between the tool and workpiece, A_c equal to the area of contact between the tool's rake face and the chip, E being the modulus of elasticity of the material and μ_f and σ_f being the coefficient of friction and average normal stress on the flank region of area A_f .

3.4 ELLIPTICAL CUTTING MODEL

Adapting the linear model for use in elliptical vibration cutting offered a unique set of challenges. The first challenge was converting the force equations to accept data based on two variables, displacement in the x and y-axis, instead of one. Since the velocity was always in a single direction, the standard model makes no attempt to address variations in path motion. The second challenge was to determine what effect a varying velocity vector would have on the model. Lastly, the idea of varying shear angle needed to be address. Previous trials have suggested conflicting methods of shear angle prediction, one based on cutting frequency and the other on geometry [7, 10].

3.4.1 Development of Elliptical Cutting Model

As with the standard force equations, elliptical milling requires information regarding; 1) the cutting parameters (UltraMill frequency, depth of cut, path axis, etc.), 2) the material being machined (hardness, modulus, etc.) and 3) the diamond tool (size and sharpness). Table 3.1 summarizes the information needed, the symbol for each and the preferred unit. Figure 3.8 is a schematic of the chip formation pictured in Figure 3.7 with the relevant cutting parameters identified

The cutting parameters are selected depending on the desired surface finish. Given a depth of cut, the HSR is selected. The HSR relates the cutting speed to the theoretical surface roughness through the index distance, f_{index} . A low surface roughness, Rt_{xy} , requires a small f_{index} . Table 3.1 lists HSR's and their corresponding theoretical surface roughness for the UMLS. The material properties, hardness and modulus of elasticity, can be obtained from a standard material handbook. The tool manufacturer establishes the nose radius and clearance angle. The remaining material and characteristic tool values are not as easily found. For this reason, experimental values (Tables 3.2, 3.3) have been assembled from past studies carried out at the PEC [18].

Table 3.1: Example of Elliptical Duty Cycle Numbers

Theoretical Surface Finishes ($f_{UM} = 10 \text{ Hz}$, $d = 6 \text{ }\mu\text{m}$)				
HSR	2D Duty Cycle	f_{index} (μm)	Up-feed (mm/min)	Rt_{xy} (nm)
0.0100	22%	2.985	1.80	3.601
0.0350	23%	10.446	6.26	44.099
0.0725	25%	21.638	13.00	189.219

Table 3.2: VAM Parameters for Force Model

Interface Parameters								
Cutting			Material			Tool		
item	symbol	unit	item	symbol	unit	item	symbol	unit
UMLS frequency	f_{UM}	Hz	vickers hardness	H	Pa	flank face friction	μ_f	--
depth of cut	d	m	modulus of elasticity	E	Pa	rake face friction	μ	--
major axis	a	m	material spring back	s	m	wear land width	ω	m
minor axis	b	m				edge radius	R_{edge}	m
duty cycle	f_{index}	m				nose radius	R	m
						clearance angle	α	radian

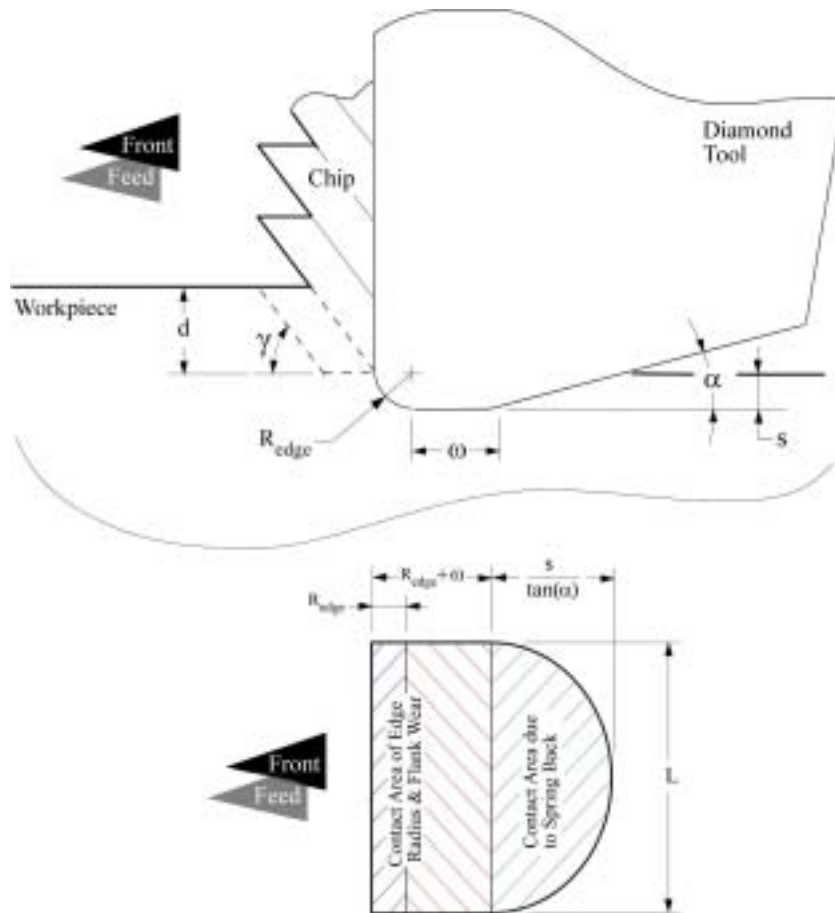


Figure 3.8: Standard Cutting Model Tool/Workpiece Interface

Table 3.3: Tool Geometry

Tool State		
Tool Feature	Sharp (nm)	Dull (nm)
wear land	0 - 50	2200
edge radius	50	270 - 400
μ_r	0.30	

Table 3.4: Measured Material Properties

Shear Angles and Material Properties						
Materials	Shear Angle	Friction	Vickers Hardness	Elastic Modulus	Spring Back	
	γ (deg)	μ (--)	(GPa)	(GPa)	Sharp Tool (nm)	Dull Tool (nm)
Electroless Nickel	22	0.78	5.3	200	60	330
Platted Copper	45	0.27	2.4	117	40	270
Aluminum 6061-T6	40	0.36	1.6	69	30	130
Aluminum 5086	30	0.58	1.0	71	20	120

The elliptical force model can be divided into two stages. The first stage involves calculating the cross-sectional areas of the chip. The second stage involves determining the thrust and cutting force, by combining the chip geometry with the tool and material properties.

Stage 1: Calculating the Chip Cross-Sectional Area

As stated earlier, aside from the tool path and tool radius, chip shape is a function of the HSR. From this ratio, the distance indexed per cycle, f_{index} , is calculated through the use of Equation (15). f_{index} can be combined with displacements of the major axis, a , and minor axis, b , of the tool path ellipse to establish the thickness (y-axis displacement) of the chip at every point in x. Figure 3.9 depicts the elliptical path of the current and previous cycles.

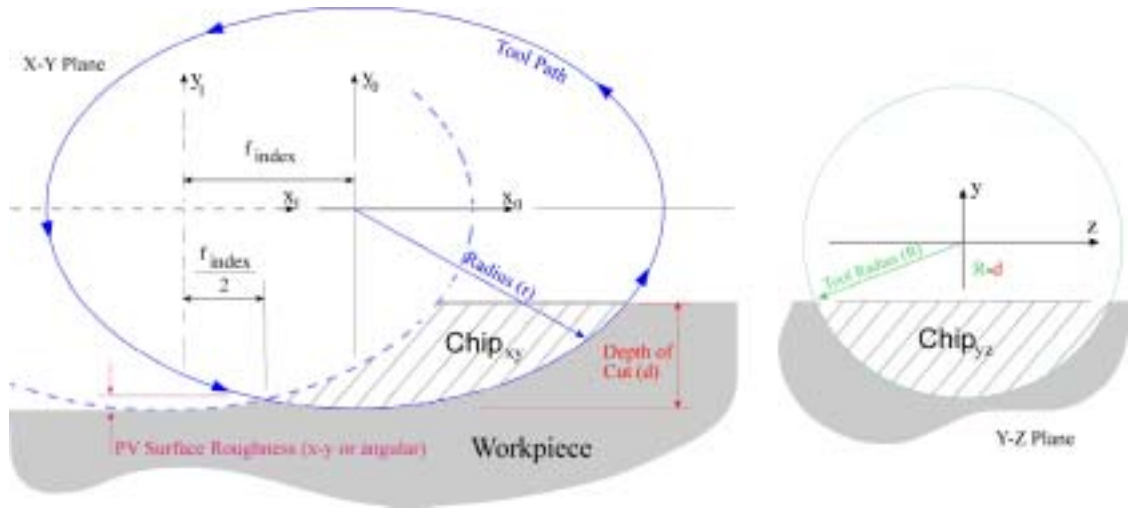


Figure 3.9: Basic Geometry in 2D “Straight Line” Elliptical Cutting

The y-component of each cycle is calculated by,

$$y_1 = \pm \sqrt{\left(1 - \frac{(x + f_{index})^2}{a^2}\right)} b^2 \quad (24)$$

$$y_0 = \pm \sqrt{\left(1 - \frac{x^2}{a^2}\right)} b^2 \quad (25)$$

where sub-scripts 1 and 0 denote the previous and current cycles respectively. The location of the surface is determined by subtracting the minor axis, b , from the depth of cut, d .

$$y_{surface} = b - d \quad (26)$$

The sign that results from Equation (26), determines whether a chip is Class A or Class B. A positive value signals a segmented chip or Class B chip. While a negative value calls for the surface to be above the centerline of the elliptical path, thus it is a Class A chip.

The depth of cut of both the current cycle and previous cycles are given by the following piecewise formulas.

$$depth_1(x) = 0 \quad \text{If} \quad x < -\sqrt{\left(1 - \frac{y_{surface}^2}{b}\right)a^2} - f_{index} \quad (27)$$

$$\dots = -y_{surface} + y_{current} \quad \text{If} \quad -\sqrt{\left(1 - \frac{y_{surface}^2}{b}\right)a^2} - f_{index} \leq x \dots$$

$$\dots x \leq \sqrt{\left(1 - \frac{y_{surface}^2}{b}\right)a^2} - f_{index}$$

$$\dots = 0 \quad \text{Otherwise}$$

$$depth_0(x) = 0 \quad \text{If} \quad x < -\sqrt{\left(1 - \frac{y_{surface}^2}{b}\right)a^2} \quad (28)$$

$$\dots = -y_{surface} + y_{current} \quad \text{If} \quad -\sqrt{\left(1 - \frac{y_{surface}^2}{b}\right)a^2} \leq x \dots$$

$$\dots x \leq \sqrt{\left(1 - \frac{y_{surface}^2}{b}\right)a^2}$$

$$\dots = 0 \quad \text{Otherwise}$$

Subtracting Equation (27) from Equation (28) results in the x-y thickness of the chip. However, since the desired end result is the area of the chip and not the thickness, the model doesn't subtract the two depth values at this point. Instead the cross-sectional area of the diamond tool that corresponds to each cycle's respective depth below the workpiece surface is determined. The geometrical relationship between nose radius, tool depth and tool / workpiece contact area is shown in Figure 3.10.

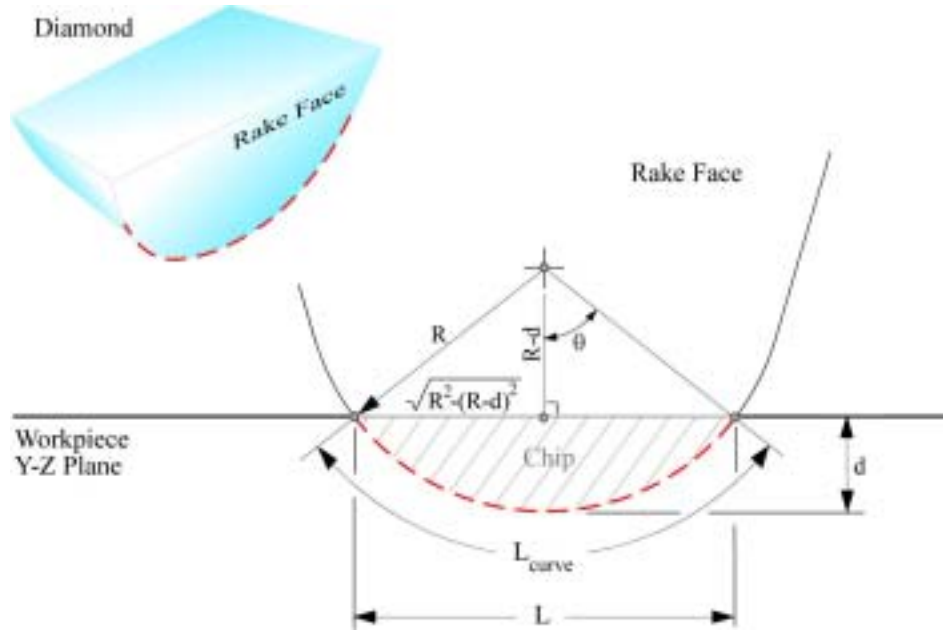


Figure 3.10: Tool Contact Area and Length

The y-z chip area is related to the depth by the angle of contact, θ , given in radians and the tool radius, R , by the following,

$$\theta_{1,0} = \cos^{-1}\left(1 - \frac{depth_{1,0}}{R}\right) \quad (29)$$

Recalling the subscript notion, the contact angle for the previous tool pass would be θ_1 and would use $depth_1$. The current pass would use terms with subscripts of θ . From this angle, the chip area is calculated.

$$A_{chip,0} = \left[R^2 \theta_{1,0} - (R - depth_{1,0}) \sqrt{depth_{1,0} (2R - depth_{1,0})} \right] \quad (30)$$

The two areas are now subtracted to achieve the cross-sectional area of the chip at each point in x.

$$\begin{aligned}
 Area_{chip} &= 0 & \text{If } x < \frac{-f_{index}}{2} & \quad (31) \\
 \dots &= A_{chip_1} - A_{chip_0} & \text{If } x \geq \frac{-f_{index}}{2} &
 \end{aligned}$$

Figure 3.11 shows the output of the preceding equations. It should be noted that graphs in Figure 3.11 are for a Class B “segmented” chip. A Class B chip is formed when the depth of cut is less than the minor axis of the tool path (see Section 3.1.1).

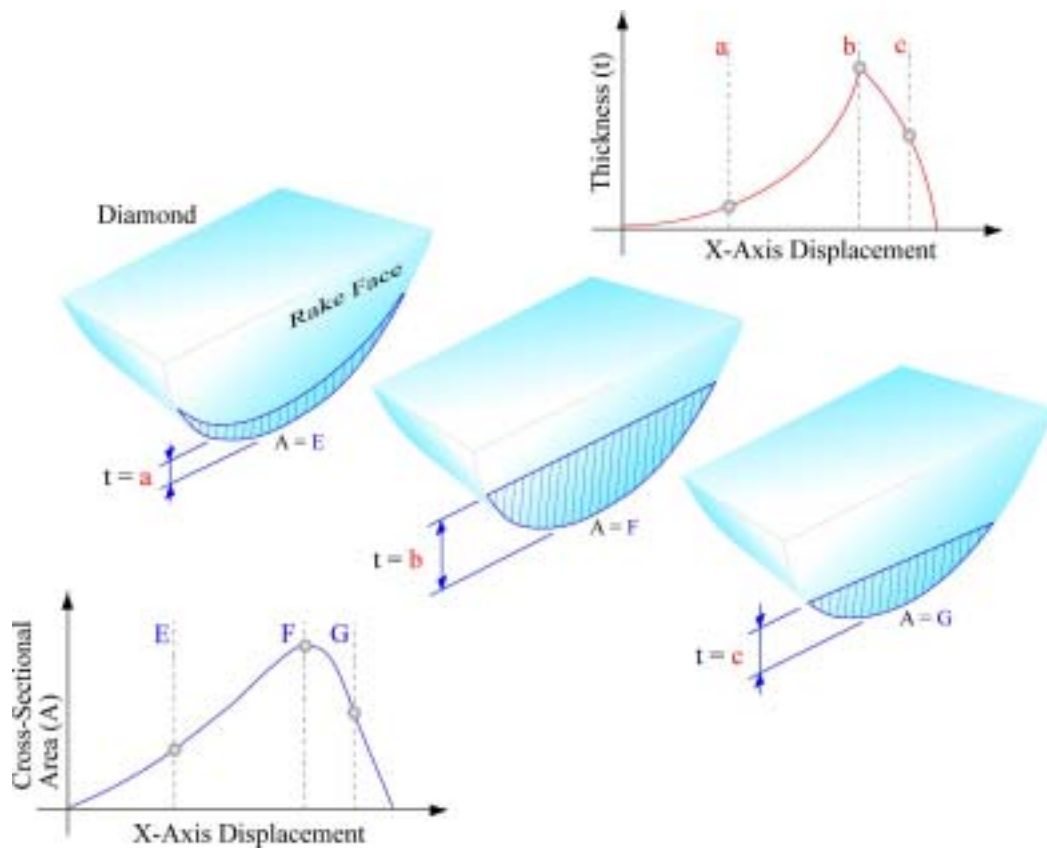


Figure 3.11: Chip Thickness and Tool Contact Area

Stage 2: Deriving the Force Components

Following the area calculation, the length of contact that the edge of the tool makes with the workpiece is now found by,

$$L_{curve_{1,0}} = 2R\theta_{1,0} \quad (32)$$

for each tool pass. The contact length is one of four components that determine the size of the contact patch where the tool and the material rub during the cutting cycle. This patch is referred to as the Area of Friction and denoted as A_f .

$$A_{f,0} = L_{curve_{1,0}} \left(R_{edge} + wear_{land} + \frac{2s}{3 \tan(\alpha)} \right) \quad (33)$$

The additional parameters are the edge radius, R_{edge} , the wear land, $wear_{land}$, and a material spring back term. Figure 3.12 illustrates the interaction between the diamond edge and the material during a tool pass. The edge radius is a function of the sharpness of the tool; Table 3.3 provides a range of 50nm for a sharp tool to 400nm for a dull tool. The wear land, $wear_{land}$, defines the amount of contact made between pre-existing wear and the changing slope of the workpiece. The last term in Equation (33), provides the width of contact between the tool's flank face and the workpiece resulting from the material spring back, s , the tool relief angle, α . This term also varies with tool x-axis displacement. The wear land is calculated by,

$$\begin{aligned} wear_{land} &= wl \quad \text{If } x \leq -\frac{f_{index}}{2} \\ \dots &= \left[wl \cdot \left(1 - \frac{x}{a} \right) \right] \quad \text{If } \frac{-f_{index}}{2} < x \leq a \\ \dots &= 0 \quad \text{Otherwise} \end{aligned} \quad (34)$$

The wear land the spring back terms decrease as the cutting progresses due to the increasing slope of the elliptical tool path. Therefore, the frictional area reaches a maximum at the x-axis displacement corresponding to the minimum depth of cut and then decreases to become only a function of the edge radius and the face height as the wear land and spring back terms tend to zero.

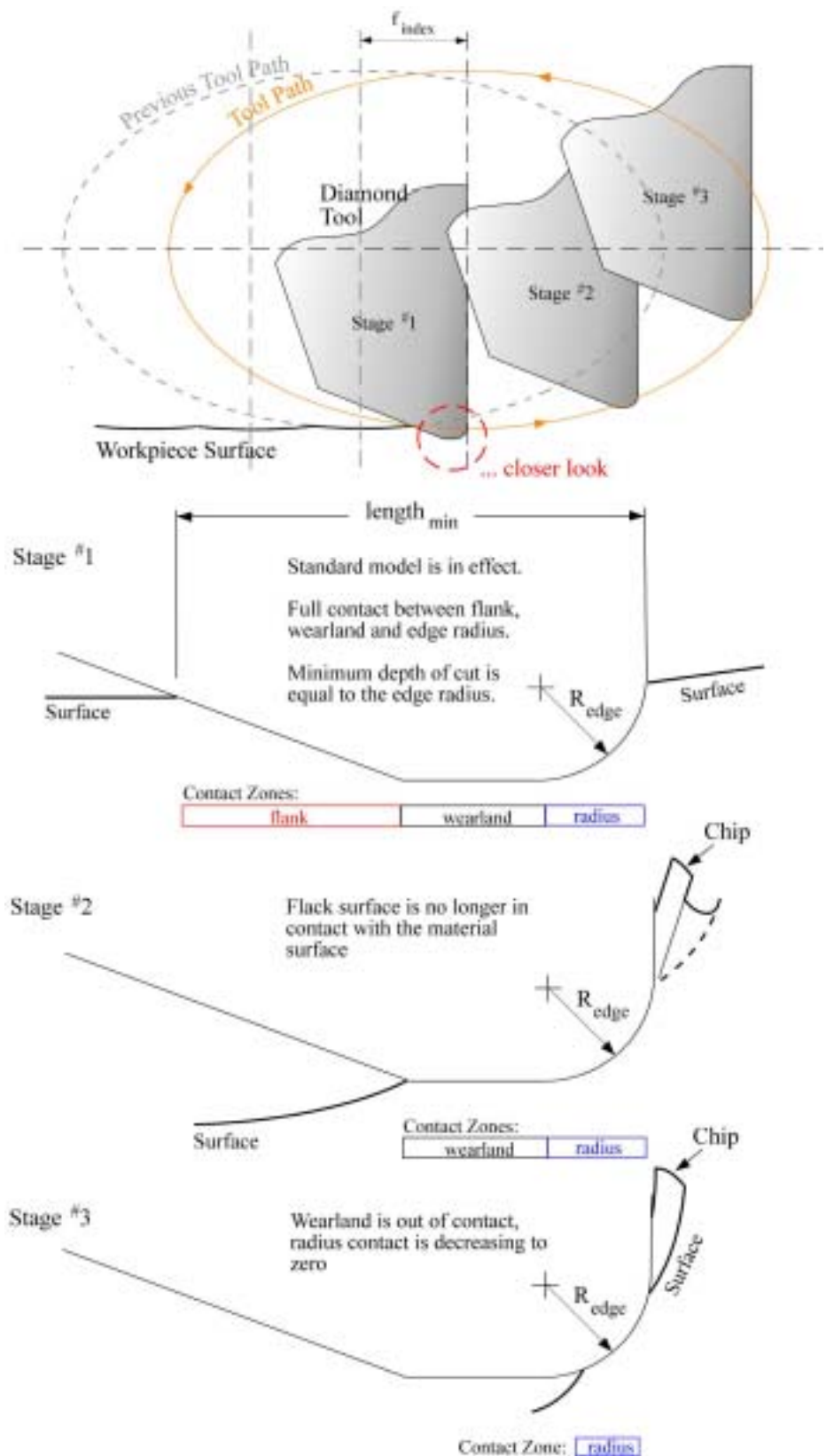


Figure 3.12: Tool Edge Components and the Elliptical Cutting Cycle

The interaction between the surfaces of the diamond and the workpiece, pictured in Figure 3.12, has been divided into three stages. At Stage #1, the depth of the diamond tip is not yet sufficient to initialize the formation of a chip. The material flows under the tool rather than shearing. All lower sections of the tool edge have contact with the workpiece. From Equation (33) this will yield a large frictional area, A_f , in turn producing high cutting and thrust forces, Equations (21) and (22). At Stage #2, the slope of the workpiece wall is such that the flank side of the tool is no longer in contact with the workpiece. This results in a lowering of the frictional area. Continuing to Stage #3, the wall's slope has increased to a point that only the edge radius, R_{edge} , is in contact. This last portion of contact fades to zero as the slope of the tool path approaches 90° at tool exit.

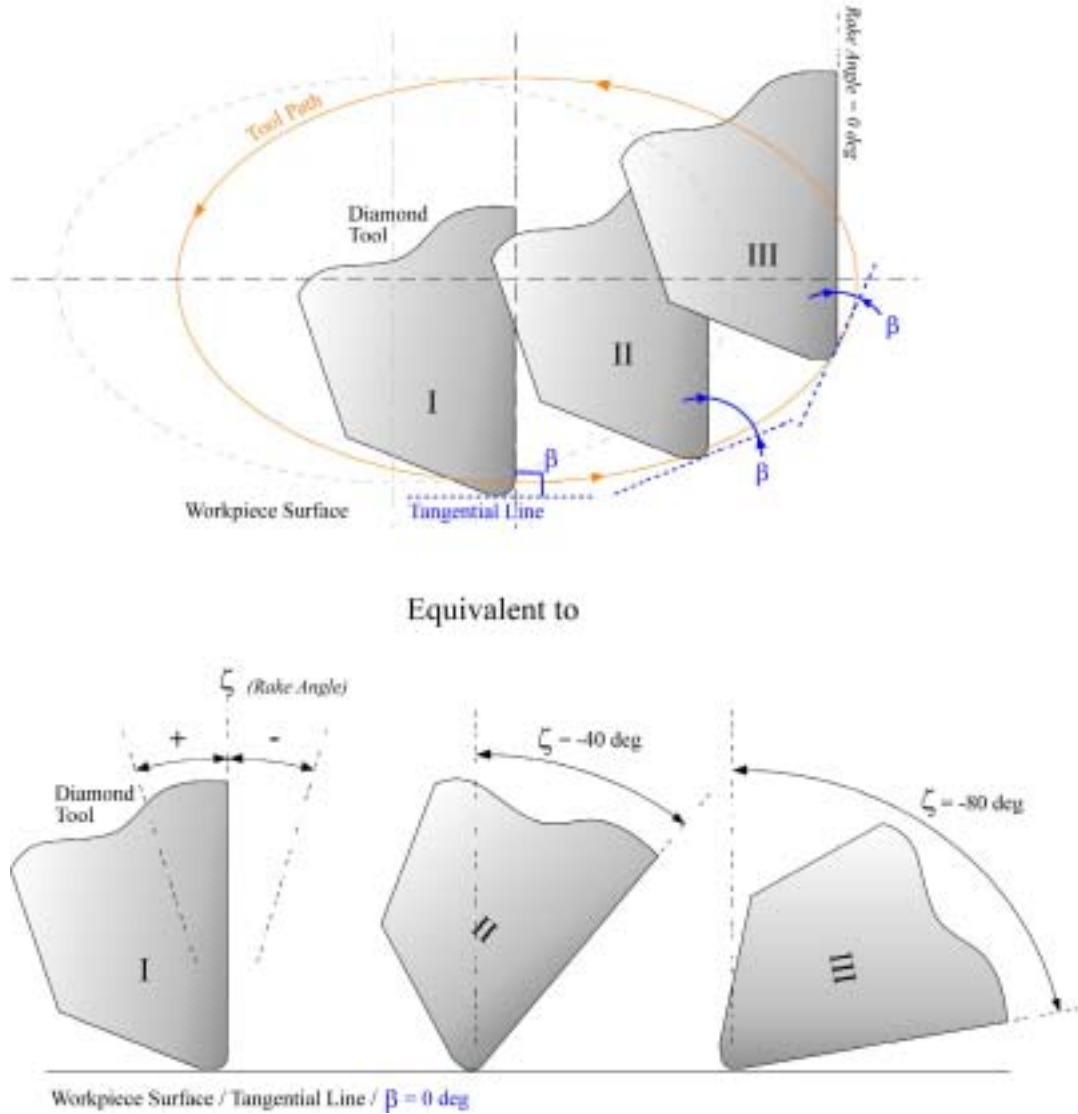
Unlike the chip area of contact, A_{chip} , which required subtracting the previous cycle's chip cross-section from the current cross-section, the frictional area, A_f is only a function of the current tool path and the tool area that rubs against material.

$$\begin{aligned}
 A_{friction} &= 0 & \text{If } x < \frac{-f_{index}}{2} & \quad (35) \\
 \dots &= A_{f_0} & \text{If } x \geq \frac{-f_{index}}{2} &
 \end{aligned}$$

The next component needed for the machining force model is the shear angle. Experimental trials have shown shear angles to be a result of material properties (hardness, shear stress) and tool rake angle [10, 18]. Typical values are presented in Table 3.4 for a tool with a 0° rake angle. Treating shear angle as a constant is not valid for elliptical cutting since the angle between the rake face and path tangential line is constantly changing. This geometry is analogous to decreasing the rake angle on a flat surface.

Figure 3.13 illustrates three discrete times in the cutting cycle. At Time I, the apparent rake angle, ζ , is zero because the material surface is perpendicular to the rake face of the tool. At Time II, the angle between the rake face and the workpiece surface, β , has decreased. This is the identical a negative rake angle tool on a flat surface. Finally at

Time III, the tool is nearing the exit of the workpiece and β has decreased to almost zero (or ζ has increased to almost 90°).



Many attempts have been made to predict the shear angle during machining. Two reports by Nakayama of Yokohama National University, Japan and another by Dautzenberg of the University of Technology Eindhoven, Netherlands, investigated shear angle formation due to rake angle geometry and material hardness [9,10]. While not highly accurate, the models and the subsequent testing data did point to shear angle decreasing

with negative rake. Therefore, an expression was developed that varied shear angle as a function of the tools path. The rake angle is found by taking the derivative of the tools path with respect to x-axis displacement.

$$\zeta = -\frac{d}{dx} y_0 \quad (36)$$

The shear angle, γ , is calculated by subtracting the rake angle, ζ , from 90° or $\pi/2$ radians.

$$\gamma = \frac{\pi}{4} - \frac{\theta}{2} \quad (37)$$

Equation (37) assumes that the shear angle is the bisector of the angle, β , formed between the rake angle and the tool rake face. These angles are shown in Figure 3.14.

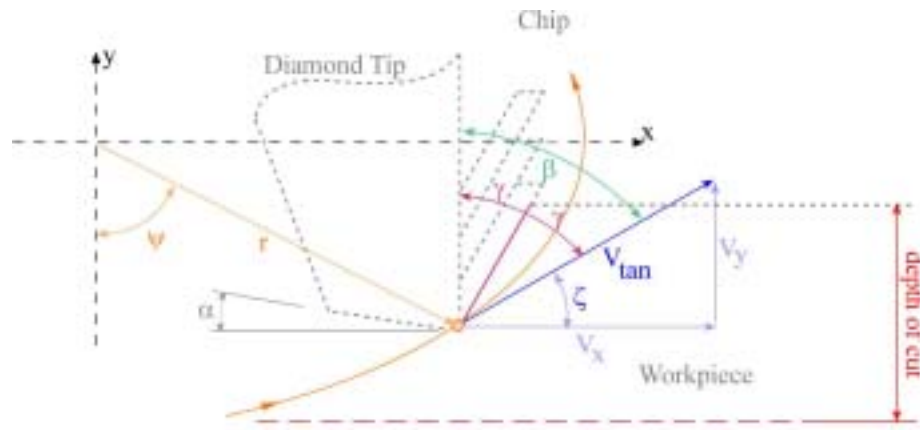


Figure 3.14: Shear Angle Geometry

The shear angle is plotted in Figure 3.15 as the tool increases in x-axis displacement. Note that at $x = 0 \mu\text{m}$, the rake face of the tool is perpendicular to the workpiece surface as in standard turning. The shear angle at this point is 45° , the approximate shear angle listed in Table 3.4 for copper and aluminum. As x-axis displacement of the tool approaches the major axis distance, a , the shear angle approaches 0° .

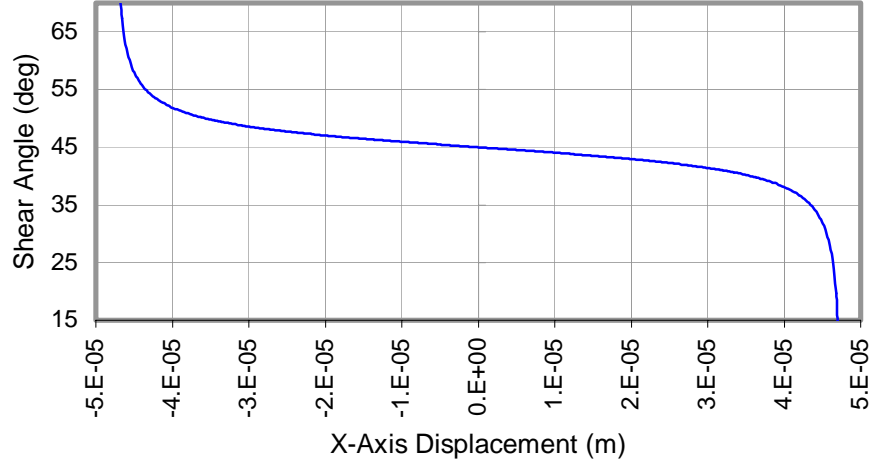


Figure 3.15: VAM Shear Angle

The last variable to be modified for 2D vibration assisted machining is that of the material hardness. Previous work has shown that when the depth of cut (chip thickness for 2D VAM) is on the same order of magnitude as the tool edge radius, R_{edge} in Figure 3.12, that work hardening of the material will take place [22, 23]. The effected distance into the workpiece surface that is affected by plastic deformation from the previous tool pass can be approximated by,

$$\rho = R_{edge} e^{\frac{H}{\sigma_y} - 0.5} \quad (38)$$

where ρ is the depth below the workpiece surface where work hardening becomes negligible, R_{edge} is the tool edge radius, σ_y is the yield stress and H is the bulk material hardness. If the chip thickness falls within this work-hardened layer, ρ , the hardness variable must be adjusted. When applicable, 2D VAM model utilized correction curves developed by Evans that varied the hardness according to the depth of cut and tool edge radius. As an example, the material hardness curve for 2D VAM of copper at a 6 μm depth of cut is plotted in Figure 3.16

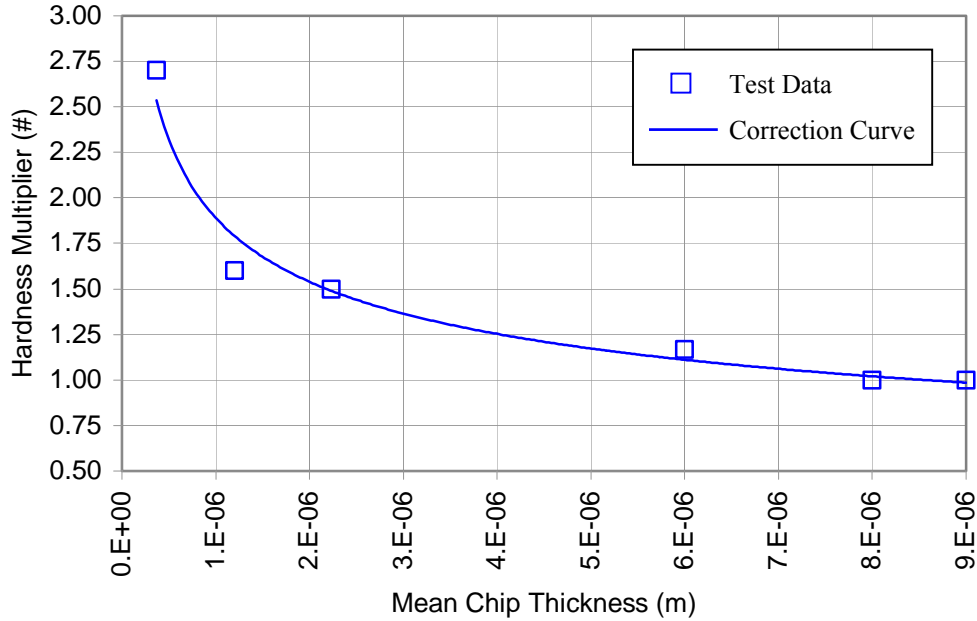


Figure 3.16: Hardness Correction Curve for Copper
($d = 6 \mu\text{m}$, $R_{edge} = 300 \text{ nm}$)

3.4.2 Complete Elliptical Cutting Model

With the variables known throughout the elliptical tool path, the force equations for cutting and thrust are assembled. To gain a better understanding of each term in the model, the cutting and thrust force equations have been divided into two parts.

3.4.2.1 Thrust Force

The first thrust component captures the thrust force in the y-z plane. It is caused by contact between the rake face and the cross-sectional area of the chip.

$$Force1_{thrust} = \mu \left(H \frac{A_{chip}}{3} \right) \left(1 + \frac{\cot(\gamma)}{\sqrt{3}} \right) \quad (39)$$

The second thrust component is controlled by the x-y geometry of the tool as it slides along the surface of the workpiece.

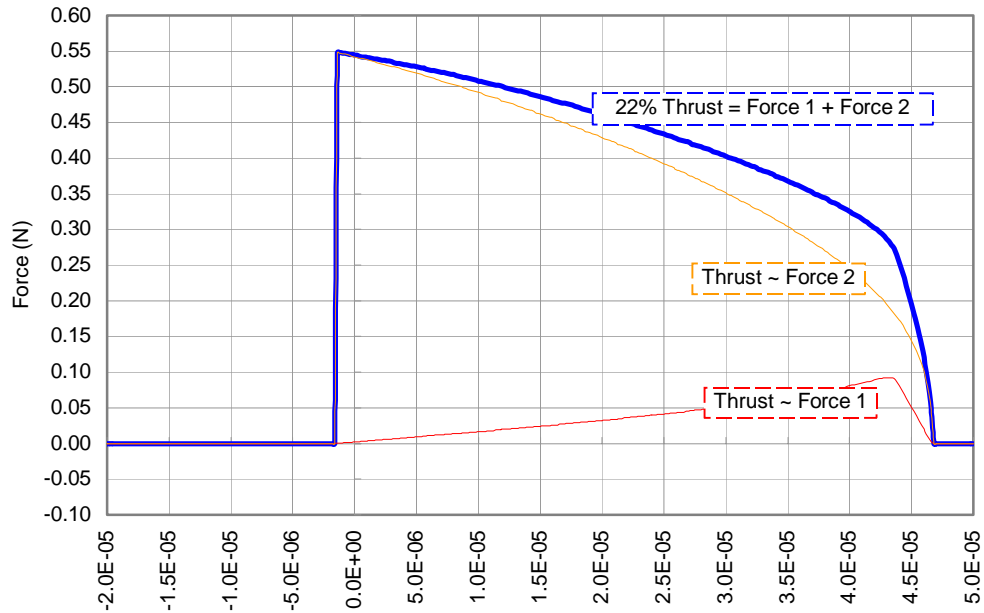
$$Force2_{thrust} = \sigma_f A_f \quad (40)$$

Summing the two thrust components gives the thrust equation for all 3 dimensions,

$$Sum_{thrust} = Force1_{thrust} + Force2_{thrust} \quad (41)$$

Figure 3.17 plots the components of the thrust force for a 22% 2D VAM duty cycle cut at a depth of 6 μm in C110 Copper. The machining parameters are indicated below the graph. The material parameters can be found in Table 3.4. The tool parameters are for a dull tool and listed in Table 3.3.

Note how each part of the thrust equation contributes to the overall thrust. $Force2_{thrust}$, which contains the frictional area term, A_f , provides the majority of the force. As illustrated in Figure 3.12, the thrust force decreases due to the reduction of contact between the edge of the diamond tool and the workpiece. The magnitude and shape of $Force1_{thrust}$ contains information on the chip size via its cross-sectional area, A_{chip} , and mirrors the growth and decay of the chip thickness.



Thrust Force for 22% 2D Duty Cycle
 (C110 Cu, $d = 6 \mu\text{m}$, $a = 47.5 \mu\text{m}$, $b = 7.3 \mu\text{m}$, $R_{edge} = 3 \text{ mm}$, $f_{UM} = 10 \text{ Hz}$, dull tool)

3.4.2.2 Cutting Force

The cutting force components, sometimes referred to as the “primary” force in other literature, are given as;

$$Force1_{cut} = \left(H \frac{A_{chip}}{3} \right) \left(1 + \frac{\cot(\Lambda_{shear})}{\sqrt{3}} \right) \quad (42)$$

$$Force2_{cut} = \mu_f \sigma_f A_f \quad (43)$$

The force perpendicular to the y-z plane opposing the tool moving through the material is captured in the $Force1_{cut}$ term. Parallel to the x-y plane, the $Force2_{cut}$ component is a result of the material deforming under the tool’s edge. Summing these two equations results in the complete cutting force equation,

$$Sum_{cut} = Force1_{cut} + Force2_{cut} \quad (44)$$

Figure 3.18 plots the output of the cutting force equation given the same input parameters as those used in the previous thrust calculation.

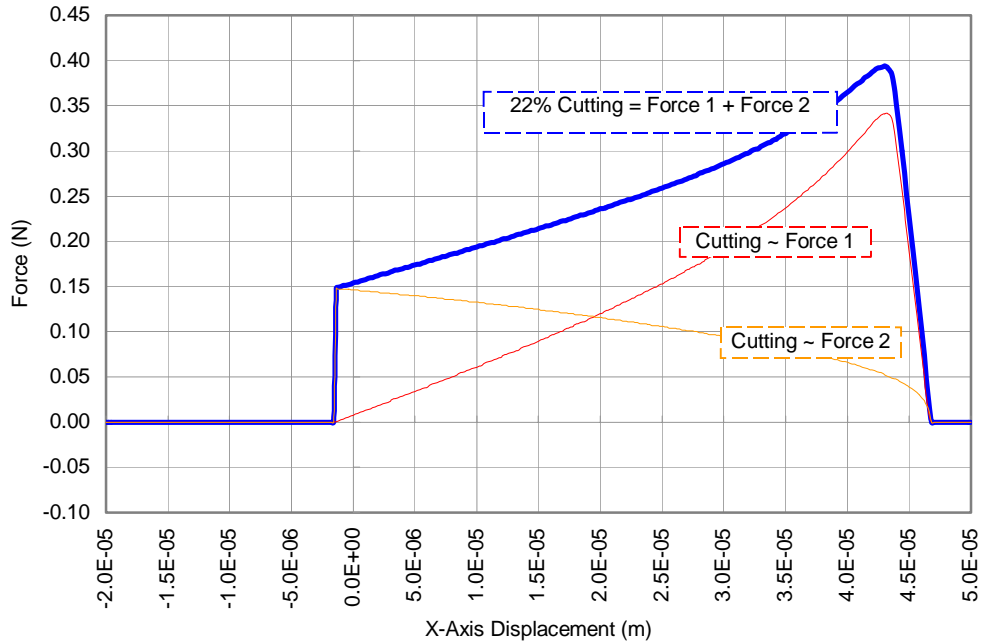


Figure 3.18: VAM Cutting Force for 22% 2D Duty Cycle
(C110 Cu, $d = 6 \mu\text{m}$, $a = 47.5 \mu\text{m}$, $b = 7.3 \mu\text{m}$, $R_{edge} = 3 \text{ mm}$, $f_{UM} = 10 \text{ Hz}$, dull tool)

Like thrust, the $Force2$ component controls the amount of force at the beginning of the chip. This is due to the depth of cut not being sufficient to cause the material to shear. Instead the material flows under the tool tip. Its magnitude decays as the slope of the wall drops away from the tool, decreasing A_f . However unlike the thrust equation, the cutting force components transition with the $Force1_{cut}$ component directing the total cutting force. The cross-sectional area of the chip, A_{chip} , controls this component.

Plotting both cutting and thrust components on the same graph, Figure 3.19, allows additional items to be observed. Note the starting point is to the left of zero. This is because the tool makes contact with the workpiece before reaching the vertical centerline of the ellipse. This was illustrated in Figure 3.9, where the starting point of chip formation is given as half of the index displacement, f_{index} . The crossover point between the cutting and thrust forces and far-right slope of the force curves are additional key features in this model.

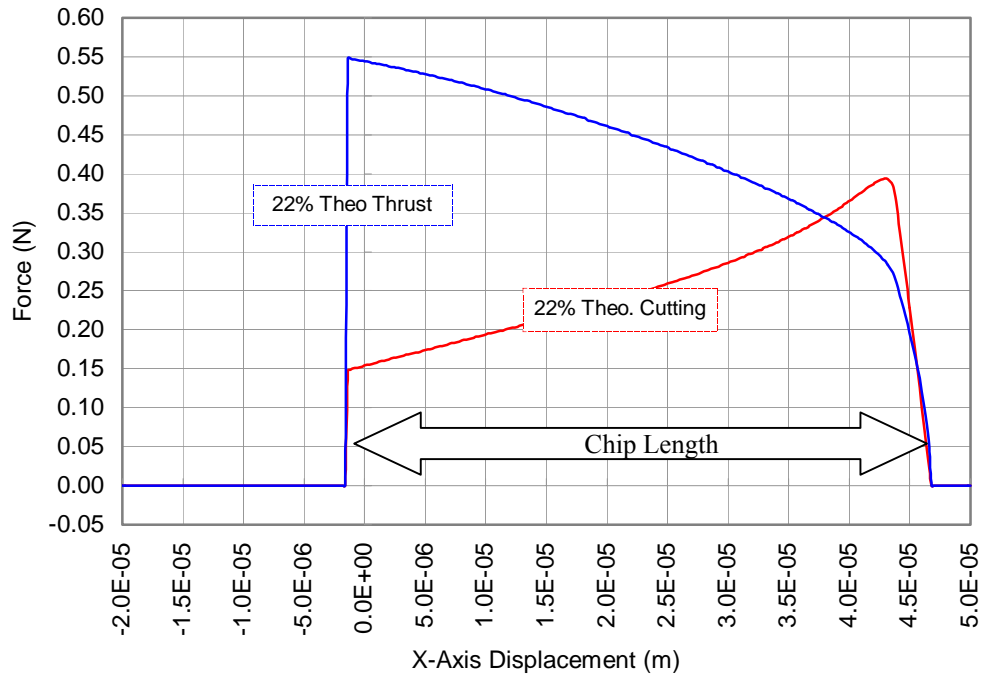


Figure 3.19: VAM Force for 22% 2D Duty Cycle
 (C110 Cu, $d = 6 \mu\text{m}$, $a = 47.5 \mu\text{m}$, $b = 7.3 \mu\text{m}$, $R_{edge} = 3 \text{ mm}$, $f_{UM} = 10 \text{ Hz}$, dull tool)

3.4.2.3 Force vs. Duty Cycle

Two additional 2D VAM cases are evaluated, 23% at 6 μm depth and 25% at 6 μm depth, to shown how the machining force should vary with increasing feed rates. Figures 3.20 through 3.22 depict the component forces, thrust and cutting, and combined forces respectively for 23% 2D Duty Cycle. The machining parameters for the additional case are identical to those of the 22% case.

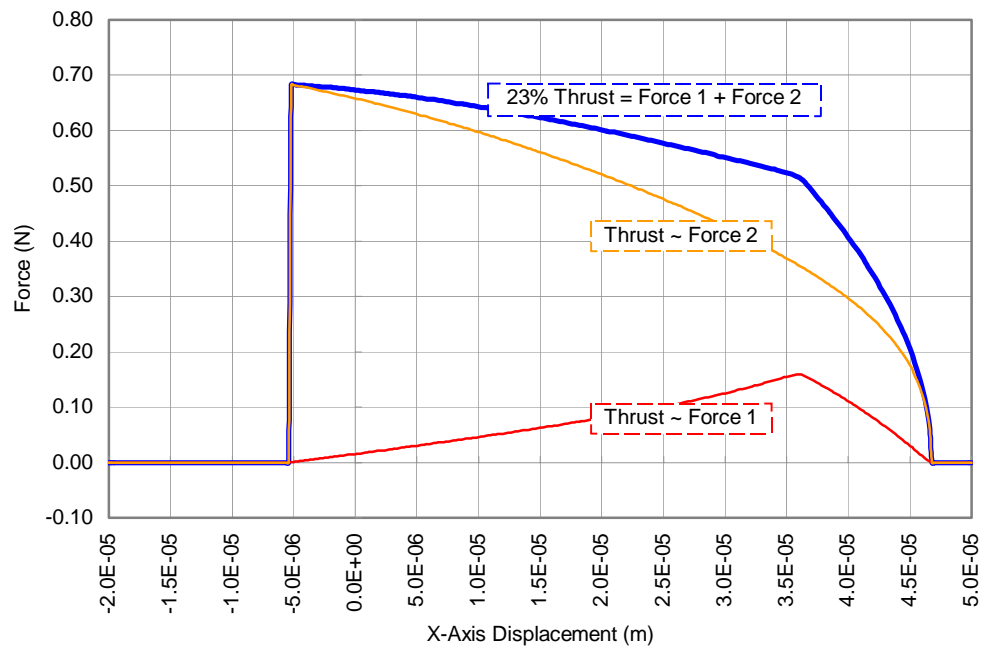


Figure 3.20: VAM Thrust Force for 23% 2D Duty Cycle

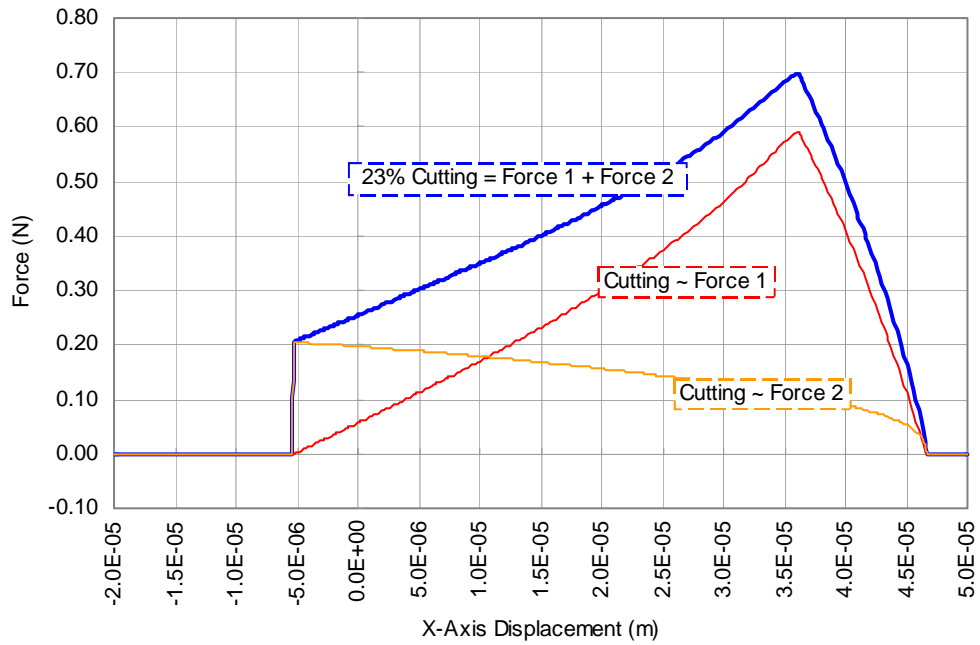


Figure 3.21: VAM Cutting Force for 23% 2D Duty Cycle

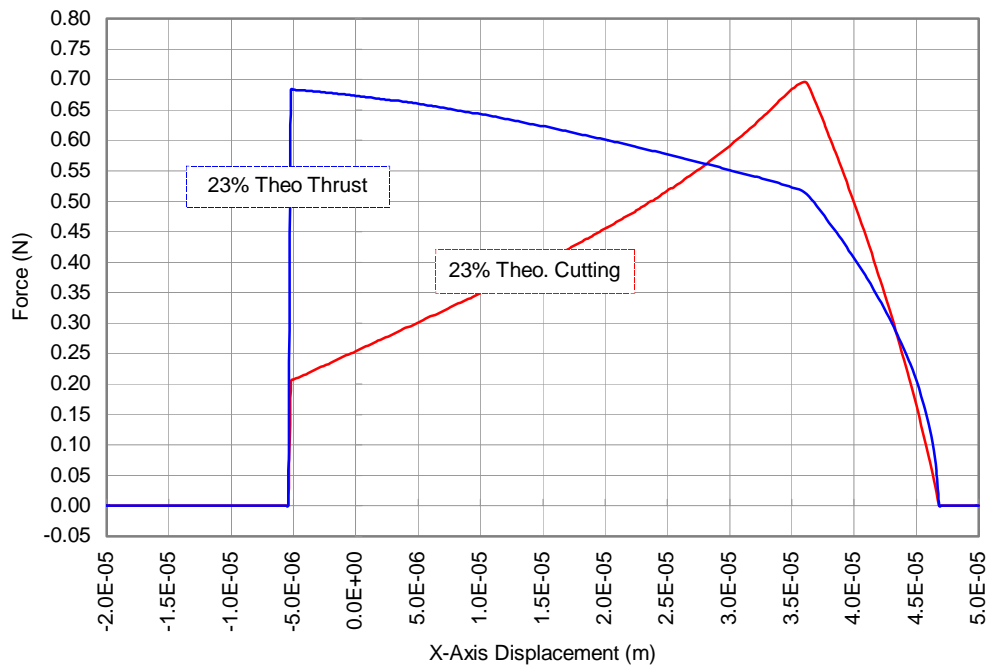


Figure 3.22: VAM Force for 23% 2D Duty Cycle

At 23%, Figure 3.22 shows that the peak values of the cutting and thrust are approximately the same. The point at which the thrust and cutting forces cross has shifted to the left compared to the transition point of the 22% cut. This shift continues with increasing duty cycles as shown in Figures 3.23-3.25. Given the same cutting parameters, the next three plots are for the 25% 2D duty cycle case.

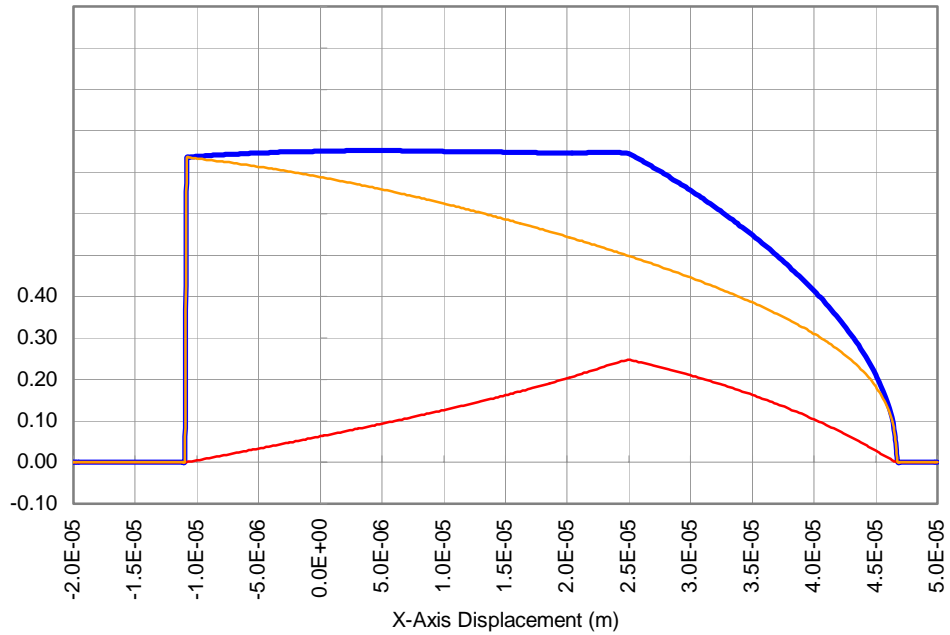


Figure 3.23: VAM Thrust Force for 25% 2D Duty Cycle

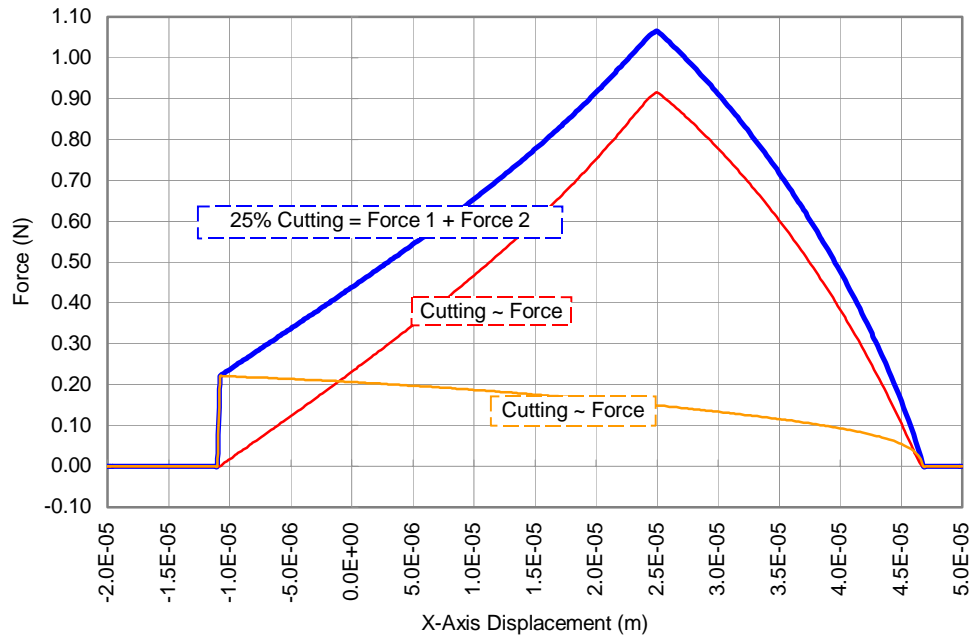


Figure 3.24: VAM Cutting Force for 25% 2D Duty Cycle

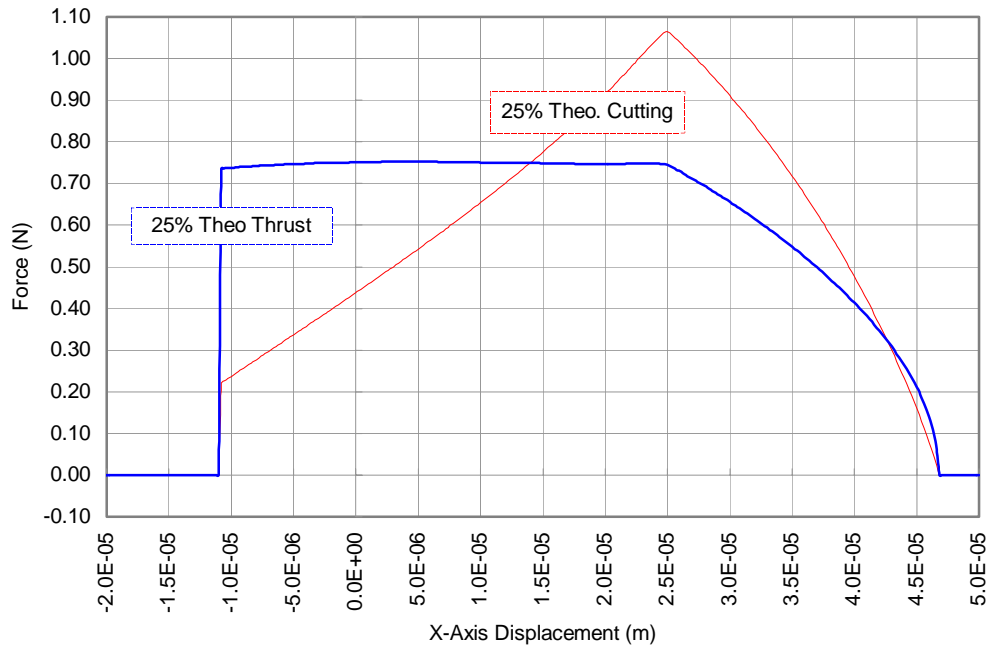
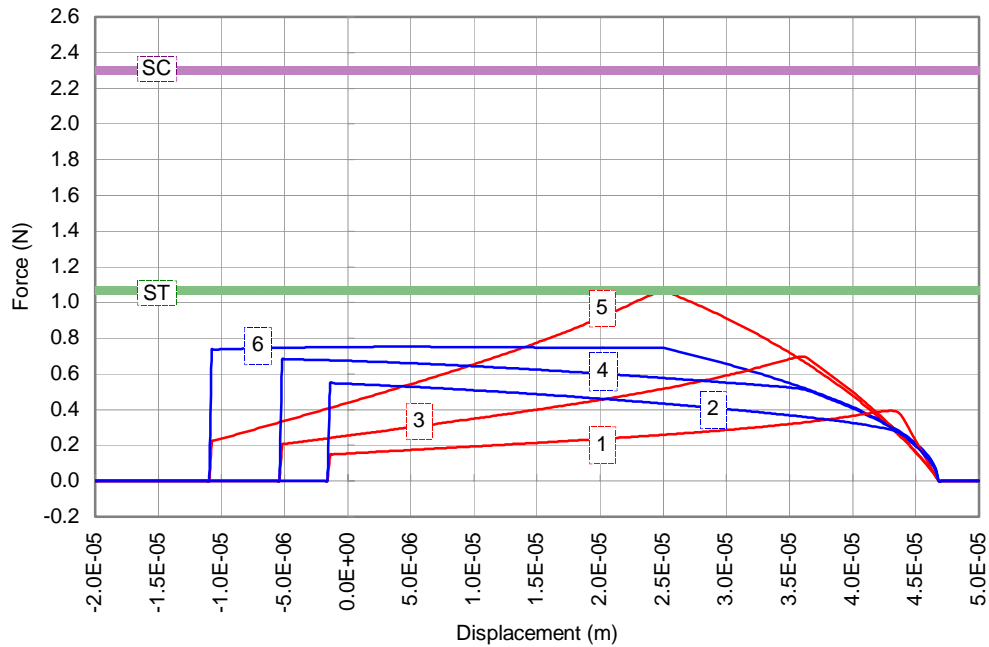


Figure 3.25: VAM Force for 25% 2D Duty Cycle

At 25%, the cutting force has exceeded the thrust force by 0.33N. The force crossover point is now midway between the beginning and end of the chip. Lastly, the chip starting point has continued to move to the left as the index distance, f_{index} , has increased.

Figure 3.26 plots the three cases just presented on a single chart. Overlaid, the trends (crossover point, ratio of cutting to thrust force increase, lengthening of chip) become more noticeable. How 2D VAM compares to conventional single point turning can also be seen in Figure 3.26 with the addition of conventional cutting and thrust forces. The parameters for both types of machining are the same with the exception of the shear angle and material hardness, both of which are constant for conventional machining but variable in VAM. For comparison purposes, the material hardness used to calculate the conventional forces was set equal to the maximum hardness of the three cases, $H(22\% \text{ DC}) = 2.7 \text{ GPa}$. The model predicts that 2D VAM will have will produce a reduction in both cutting and thrust force over the conventional machining of a material with the same hardness. An 80% reduction in cutting force and 48% reduction in thrust force for the 22% case.



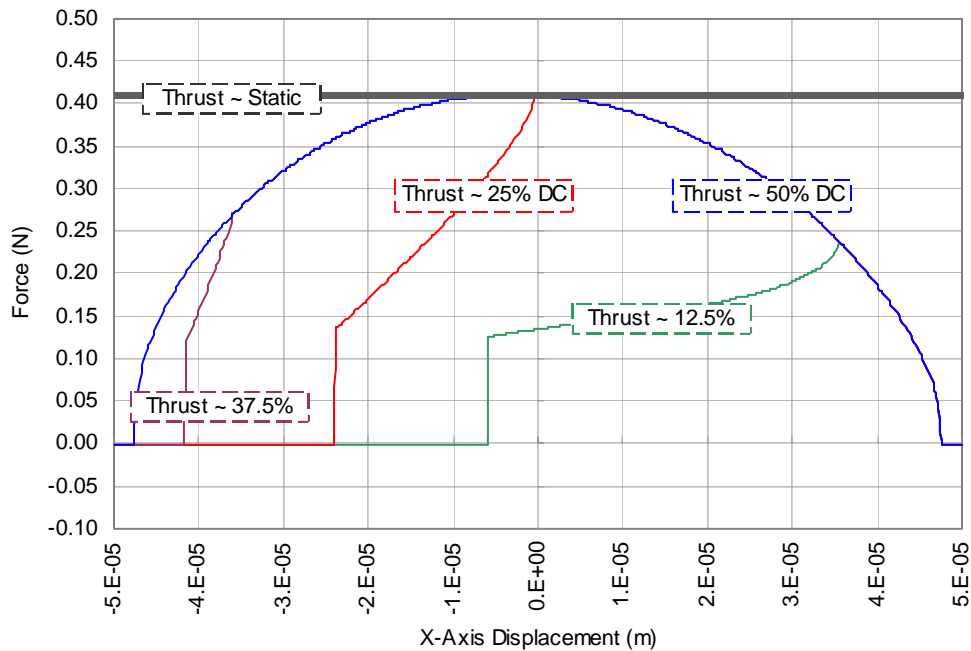
No.	Description	No.	Description
1	22% Cutting Force	5	25% Cutting Force
2	22% Thrust Force	6	25% Thrust Force
3	23% Cutting Force	SC	Standard Model Cutting Force Predict.
4	23% Thrust Force	ST	Standard Model Thrust Force Predict.

Figure 3.26: Comparison of 2D VAM and Conventional Machining Forces

3.4.2.4 Limits of VAM Force Advantage

The issue of work hardening can be negated through the use of a sharp tool. As shown in Figures 3.17, 3.20 and 3.23, the largest component of the thrust force term is Equation (40), which contains the fictional area term, A_f . Defined by Equation (33), A_f is controlled by the sharpness of the tool. A sharp tool would reduce the edge radius, the wearland and the amount of flank face contact via material spring back. It is this contact that is responsible for work hardening the material. Therefore replacing the dull tool, $R_{edge} = 300$ nm, with a sharp tool, $R_{edge} = 40$ nm, allows for a comparison utilizing identical material properties.

Figure 3.27 plots the thrust force of conventional machining; defined by Equations (22) and (23), along with the 2D VAM thrust forces at duty cycle increments of 12.5%.



*Figure 3.27: VAM Thrust Force Comparison @ 12.5% Increments
(Identical Material Properties, $d = 6 \mu\text{m}$, $f_{UM} = 10 \text{ Hz}$, $R_{edge} = 40 \text{ nm}$)*

From right to left in Figure 3.27, the 12.5% case shows an advantage of 0.17 N over the calculated standard thrust force. Note that all force slopes are bounded by the 50% 2D VAM curve. The reason for the force reduction is that the thickness of the chip is less than the depth of cut. It is at 25% that the chip thickness is equal to the depth of cut and the peak thrust forces equate. Once the duty cycle is larger than 50% no reduction in peak cutting forces are had. However, averaged over the whole chip length, 2D vibration machined parts result in reduced machining forces.

Similar to the thrust force graph of Figure 3.27, Figure 3.28 illustrates how the cutting force of 2D VAM never exceeds that of conventional machining. At 12.5%, the cutting force is reduced by 0.45 N.

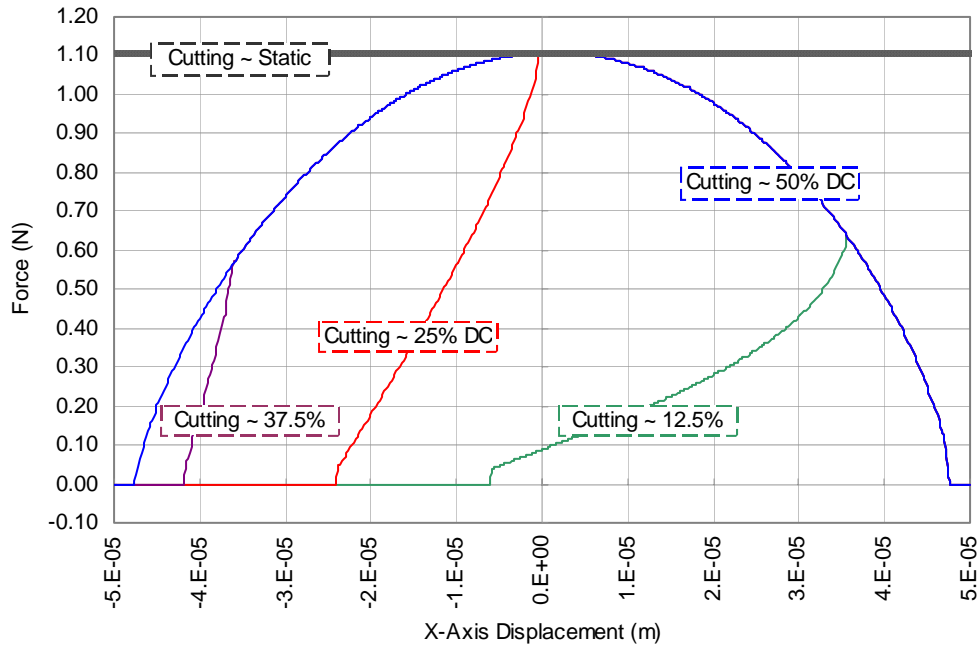


Figure 3.28: VAM Cutting Force Comparison @ 12.5% Increments (Identical Material Properties, $d = 6 \mu\text{m}$, $f_{UM} = 10 \text{ Hz}$, $R_{edge} = 40 \text{ nm}$)

3.4.2.5 Class A “Continuous” Chip

The examples plotted up until now have been for Class B or segmented chips. Figure 3.29 plots the predicted 23% 2D VAM force curves for a depth of cut ($d = 9 \mu\text{m}$) greater than the minor axis of the ellipse ($b = 7.3 \mu\text{m}$). Defined in Section 3.1.1, the chip produced is a Class A or continuous chip. All other material and tool parameters remain the same.

Immediately upon viewing this, the sharp increase in the cutting force component at distance f_{index} from the ending point is noticed. This is a result of a change in the contact area seen by the tool’s rake face. The increase in area is attributed to an increase in chip thickness. Figure 3.30 compares the thickness of a 23% 2D VAM Class A chip with a Class B chip.

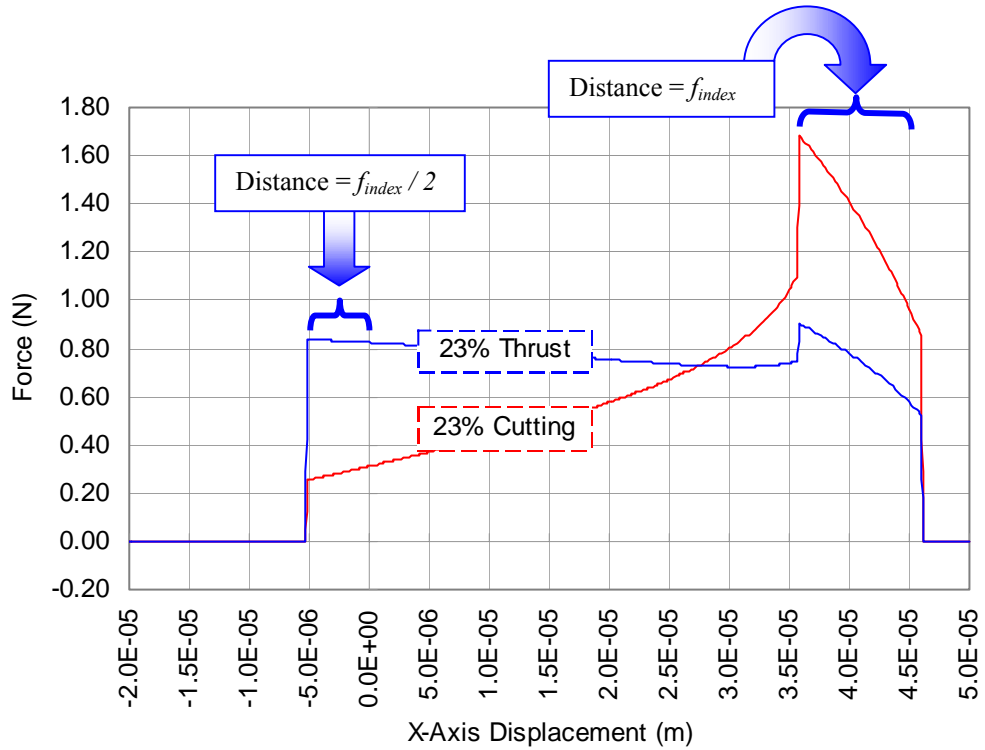


Figure 3.29: Class A Chip for 23% 2D VAM

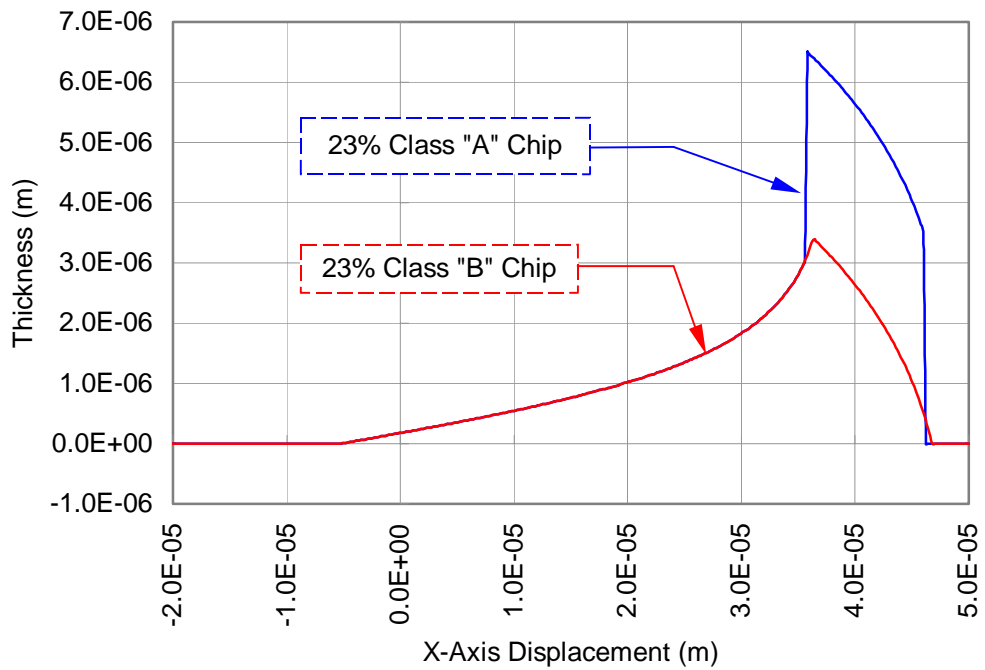


Figure 3.30: Chip Thickness Comparison

3.4.3 Reported “Lifting” Phenomena of Elliptical Machining

Presented in the paper, “Study of Elliptical Vibration Cutting,” Shamoto and Moriwaki found that elliptical machining produced a negative thrust force [7]. The oscillation of the thrust force from positive to negative is attributed to the tool lifting the chip away from the workpiece. Figure 3.31 is a plot of the thrust data from Shamoto and Moriwaki’s report.

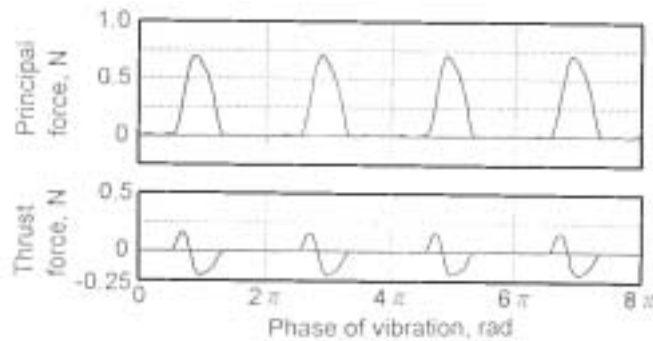


Figure 3.31: Chart from “Study of Elliptical Vibration Cutting”
The Lifting Phenomena

While reported, Shamoto and Moriwaki gave no explanation as to how this is possible. These results raise two interesting questions;

“What are the mechanics behind this phenomena?”

“If true, why is it not predicted in the PEC force model?”

3.4.3.1 Lifting Mechanics

The difference between 1D vibration machining and 2D vibration machining is that the velocity vector of the tool in 2D or elliptical machining is composed of two parts: vertical (y-axis) and horizontal (x-axis). The first step in understanding the mechanics behind the lifting phenomena is to understand the relationship between the velocity components of the tool.

The kinematics of the UMLS were illustrated in Figure 3.14. β is the angle formed between the rake face of the tool and the workpiece surface. γ is the shear angle defined by Equations (37). ζ is the slope of the tool path defined by Equation (36).

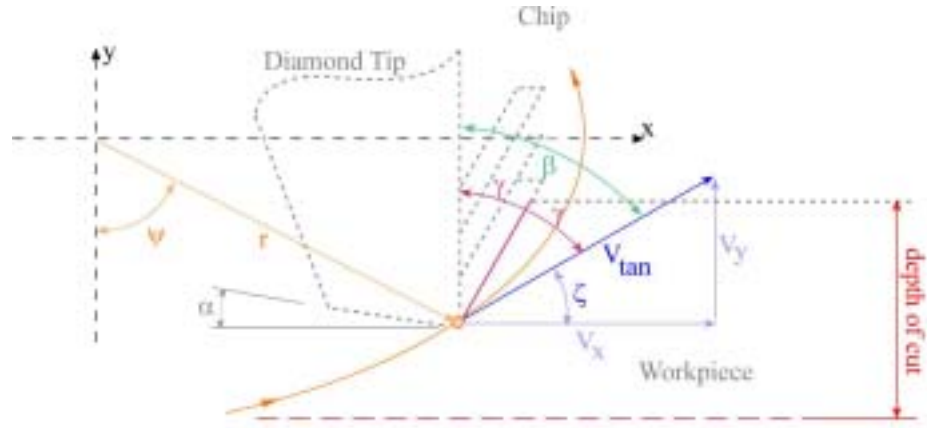


Figure 3.14: Shear Angle Geometry

In the force model derivation, tool motion was calculated as a function of x-axis displacement. To analyze velocity, the tool motion must be written as a function of time. Tool velocity components are given by,

$$V_x = \frac{d}{dt} x(t) + V_{workpiece} \quad (45)$$

$$V_y = \frac{d}{dt} y(t) \quad (46)$$

where $x(t)$ and $y(t)$, defined in Equations (12) and (13), are the tool position along the x and y-axis respectively at any point in time, t . $V_{workpiece}$ is the velocity or feed rate of the workpiece into the tool.

Lifting of the chip away from the workpiece is defined as anytime during the cutting cycle when the vertical velocity of the tool, V_y , is greater than the vertical velocity of the chip, V_{chip} . If V_y is ever greater than V_{chip} , the friction between the rake face of the tool and the chip result in a force that pulls the chip away from the workpiece. The chip velocity is defined as,

$$V_{chip} = V_x \tan(\zeta + \gamma) \quad (47)$$

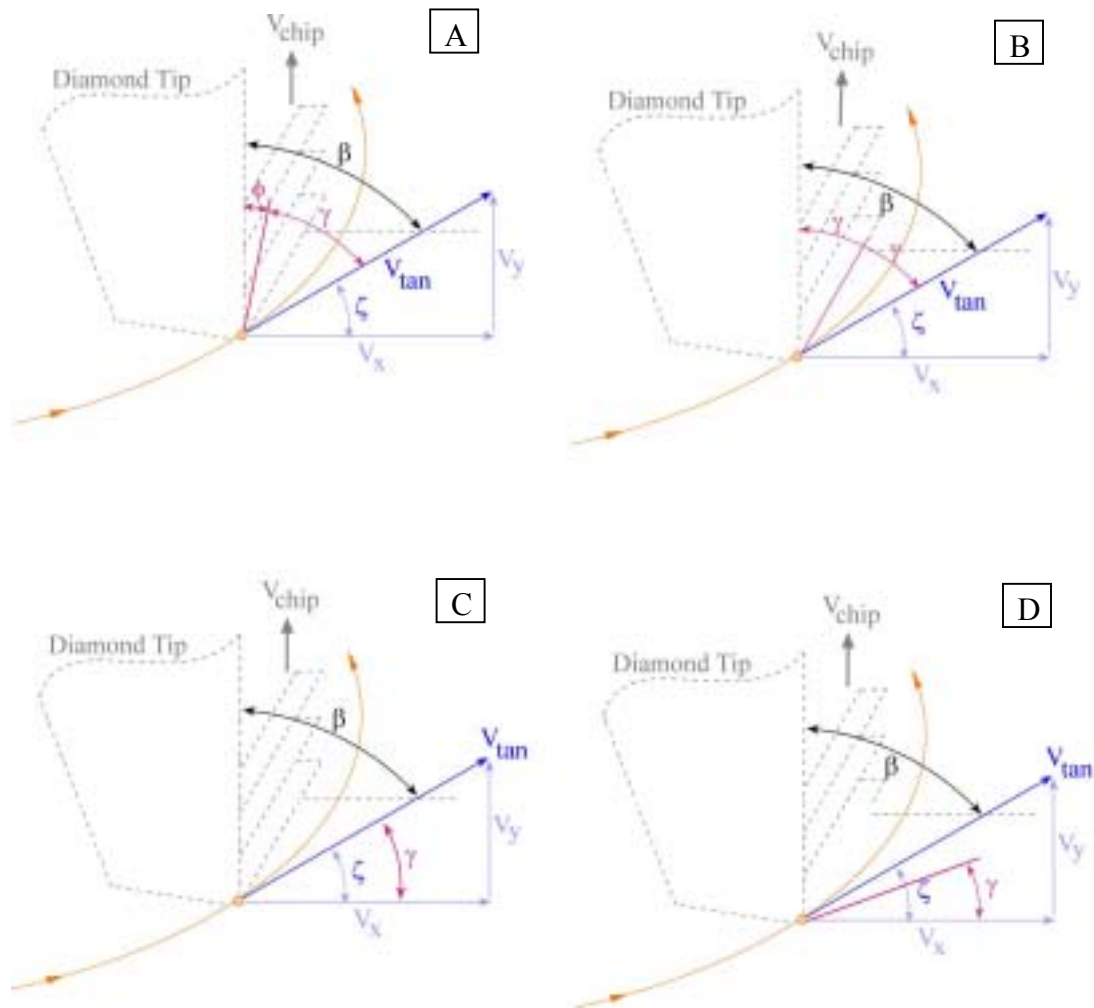


Figure 3.32: Shear Angle and Chip Velocity

V_{chip} is a function of the tools horizontal velocity, V_x , and the angle at which the material shears. The angle at which shear occurs is a combination of two angles, the material shear angle, γ , and the slope of the tool path, ζ . In order for $V_y > V_{chip}$ and lift to occur, that angle sum must hold the translated horizontal tool velocity to less than the vertical tool velocity.

With the tangential velocity of the tool, V_{tan} , constant along the path, Figure 3.32 illustrates the possible angle combinations. Note that Option B in Figure 3.32 is the assumption made in the 2D VAM model. Assigning V_{tan} an arbitrary value of 10, the component parts were calculated. The results are indicated in Table 3.5.

Table 3.5: Chip and Tool Component Velocities ~ Option Evaluation

V _{tan}	Angle		V _y V _{tan} sin (ζ)	V _x V _{tan} cos (ζ)	V _{chip}		Option (#)
	ζ	γ			V _x tan (γ + ζ)	V _x tan (γ)	
10	50	30	7.66	6.42	36.41		A
	45	22.5	7.07	7.07	17.07		B
	30		5	8.66		5	C
	60	25	8.66	5		2.33	D

As indicated in Table 3.5, the vertical tool velocity, V_y , only exceeds the chip velocity, V_{chip} , for Option D. This option depicts a material with a constant shear angle. As the slope of the tool's path, ζ , increases beyond that of the materials shear angle, γ , the velocity of the tool exceeds that of the chip and lift develops. Option B, that which the 2D VAM model employs would never show lift because the shear angle is always greater than the slope of the tool path.

3.4.3.2 Moriwaki's Lifting Phenomena

A solution does exist that would produce chip lift. However the assumption behind the solution, that the material shear angle is constant has as substantial body of evidence positioned against it [9,10]. The more likely explanation for the negative thrust force recorded in Moriwaki's experiment can be attributed to the depth of cut. In his experiment, the depth of cut was 10 μm . However the vertical displacement of the VAM servo was only 3.5 μm . This substantial mismatch caused the tool to undercut the surface of the workpiece. As the tool retracted from the workpiece the upper material was carried with it. This scenario can be seen in the force data of Figure 3.31. The force is plotted as a function of the angular tool path. Contact is maintained for π radians or 180° and negative thrust force is developed just prior to 90°. This alternate explanation is also supported by the illustration of the servo and tool path that accompanied the data, Figure 3.33. It shows the majority of the tool path falls under the surface of the workpiece.

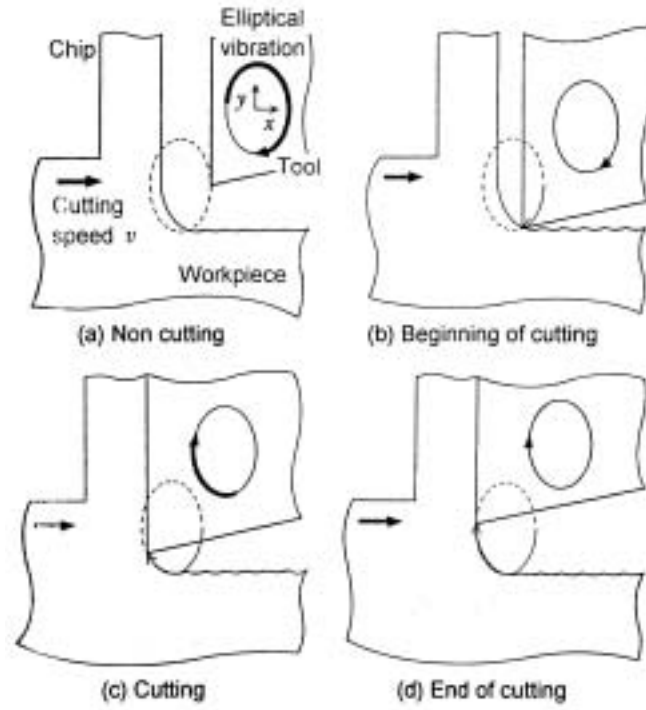


Figure 3.33: Orientation of the Moriwaki Servo Elliptical Path [7]

CHAPTER FOUR: VAM EXPERIMENTS AND TOOL WEAR

4.0 VAM RESEARCH PAST AND PRESENT

Past research has shown the benefits of 2D vibration assisted machining. 1) Surface roughness 3 and a half time lower than that of 1D vibration cutting [3]. 2) The elimination of burr due to the scooping motion of the tool [3,6]. 3) Force in the cutting direction is reduced by a half to a third as compared to that produced during conventional diamond turning [3,6]. The benefits of vibration assisted machining are not in question. What is in question is the “why.” The answer to which was explained in Chapter 3, with the analysis of cutting mechanics and development of the theoretical cutting model.

The cutting trials performed at the Precision Engineering Center were conceived to verify the geometric effects of VAM, such as projected tool shape and phase, as well to compare the cutting force model to the real force measurements.

4.0.1 Materials

Materials both typical and non-typical to diamond turning were chosen. Conventional materials with a low hardness, such as C110 copper and 6061-T6 aluminum were used for corroboration of the cutting model. Once these were understood, the material sphere was expanded to included ferrous metals which are normally avoided in diamond turning due to severe tool wear. The intermittent contact between tool and material is believed to inhibit the heat induced wear mechanism of chemical abrasion [1]. Table 4.1 lists the materials used in this investigation as well as their associated physical properties [20].

Table 4.1: Properties of Materials Used in Cutting Trials

Material Properties						
Type	Density (g/cc)	Tensile Strength Yield (MPa)	Modulus of Elasticity (GPa)	Thermal Conductivity (W/m-K)	Poisson's Ratio (--)	Vickers Hardness (GPa)
C110 Copper	8.92	217	123	388	0.33	0.841
1100 - O Aluminum	2.71	35	69	222	0.33	0.108
6061-T6 Aluminum	2.70	275	69	167	0.33	0.882
1018 Steel	7.87	370	205	52	0.30	1.574
AISI Type W2 Steel	7.83	750	205	--	0.30	2.152

Referring to the force model Equations (21) – (23) presented in Chapter 3, material hardness is one of the three important material properties, modulus of elasticity and shear angle being the other two. For this reason and to verify the referenced material properties with the materials used in the cutting trials, the Vickers hardness of each sample was measured.

$$F_c = \frac{HA_c}{3} \left(\frac{\cot(\phi)}{\sqrt{3}} + 1 \right) + \mu_f \sigma_f A_f \quad (21)$$

$$F_t = \mu \left[\frac{HA_c}{3} \left(\frac{\cot(\phi)}{\sqrt{3}} + 1 \right) \right] + \sigma_f A_f \quad (22)$$

$$\sigma_f = 0.62H \sqrt{\frac{43H}{E}} \quad (23)$$

Following the ASTM standard test method for determining the micro-hardness of materials, a Zwick[®] Model 3212 Vickers Hardness Tester was used [19]. The Vickers hardness number is computed from the following equation,

$$HV = \frac{P}{A_s} = \frac{2P \sin(\frac{\alpha}{2})}{d^2} \quad (48)$$

where P is the load in kilograms force, A_s is the surface area of indentation in mm^2 , d is the mean diagonal of indentation in mm, and α is the face angle of the indenter in degrees. For an indenter of 136° , Equation (48) can be reduced to,

$$HV = 1.8544 \frac{P}{d^2} \quad (49)$$

Figure 4.1 is the indentation left in the Type W2 Steel sample. The calculated hardness values of all the material samples are listed above in Table 4.1.

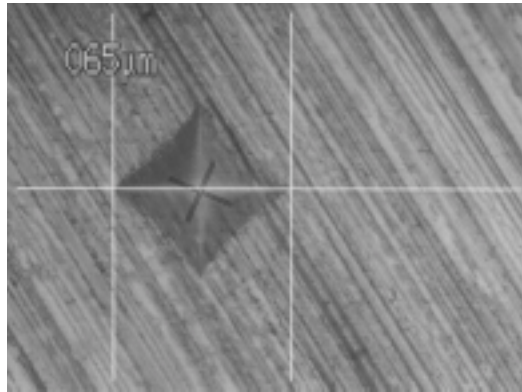


Figure 4.1: Indentation of a 0.5 kgf load in Type W2 Steel Sample (500x)

4.0.2 Experimental Setup for Surface Feature Measurement

The experiments were carried out on a Rank-Pneumo[®] ASG-2500 Diamond Turning Machine (DTM). Mated to a PEC designed controller, this 2-axis lathe has a positioning resolution of ± 2.5 nanometers. Figure 4.2, on the following page, shows how the DTM is outfitted with the UltraMill and various support equipment.

The UMLS is mounted transversely on the x-axis slide way carriage. It sits atop an adjustable base, labeled as “micro-height adjustable base” in Figure 4.2. This base is used for aligning the UMLS with the centerline of the air-bearing spindle and has $\pm 150\mu\text{m}$ of vertical travel. Also mounted on this x-axis stage are various pieces of video and lighting equipment as well as the BNC connectors that tie each piezoelectric stack to their drive amplifiers.

The air-bearing spindle, mounted on the z-axis, was rotated with a rubber timing belt, which in turn was driven by a stepper motor. The stepper motor was employed because the DTM spindle was not capable of running at the < 1 rpm rotational speed needed for the low-speed trails. The air-bearing spindle is standard equipment on a DTM due to its high mechanical stiffness and vibration free operation. It is designed to operate at speeds

greater than 500 rpm. The stepper motor is capable of rotations as slow as 0.06 revolutions per minute. The use of a rubber belt isolated the spindle from the pulse vibration of the stepper motor.

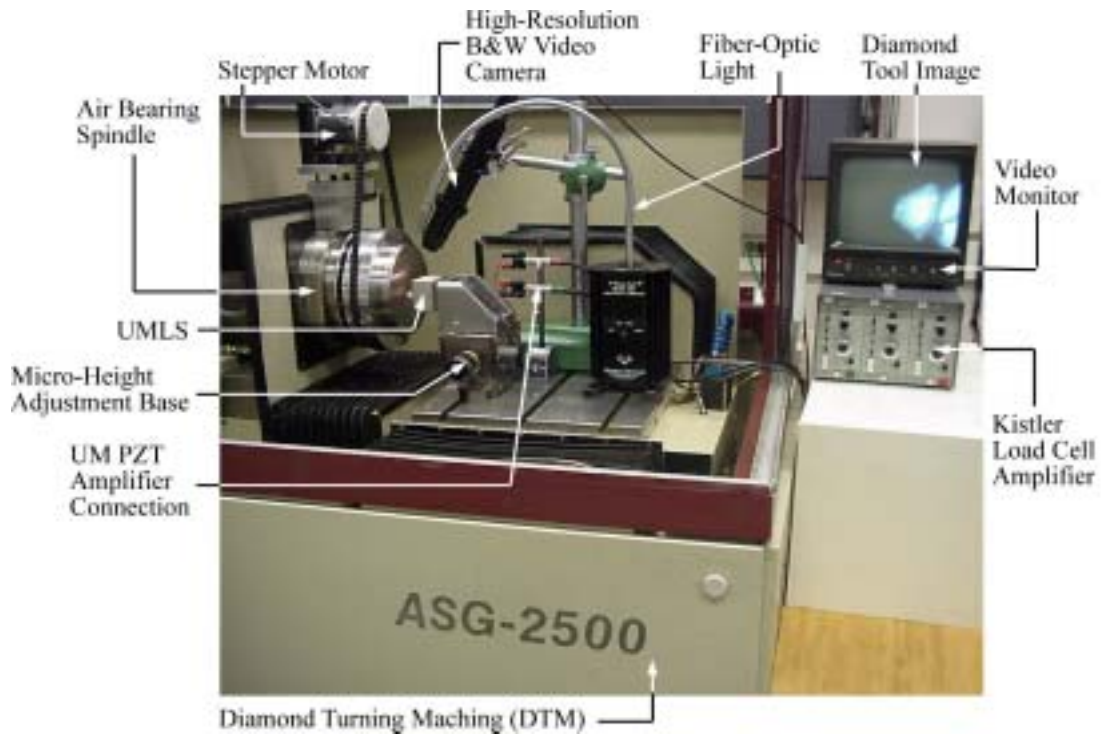


Figure 4.2: UMLS and Support Equipment on DTM

To the right of the DTM in Figure 4.2, two pieces of support equipment are shown. The first is a monochrome video monitor, used to visually inspect diamond / workpiece touch-off and to monitor testing progress. Below the monitor is the 3-channel amplifier. This amplifier was used with the 3-axis load cell to process the force signals during the cutting trials, and with an UM base mounted accelerometer to analyze and eliminate stray vibration frequencies during initial set-up.

Figure 4.3 is a close-up view of the UltraMill on the DTM. From this angle it is easier to see the diamond tool and its relation to the workpiece. The workpiece is mounted on the vacuum chuck of the air-bearing spindle. Also visible in Figure 4.3 is the labeling method of the PZT stack actuators. Recalling from Chapter 2, the two stacks of the UMLS are

denoted as stack #1 or red stack and stack #2 or green stack. Correct identification of each stack is important since the drive signals are separated by a 90° phase shift and incorrect connection will cause the tool tip motion to be in the wrong direction.

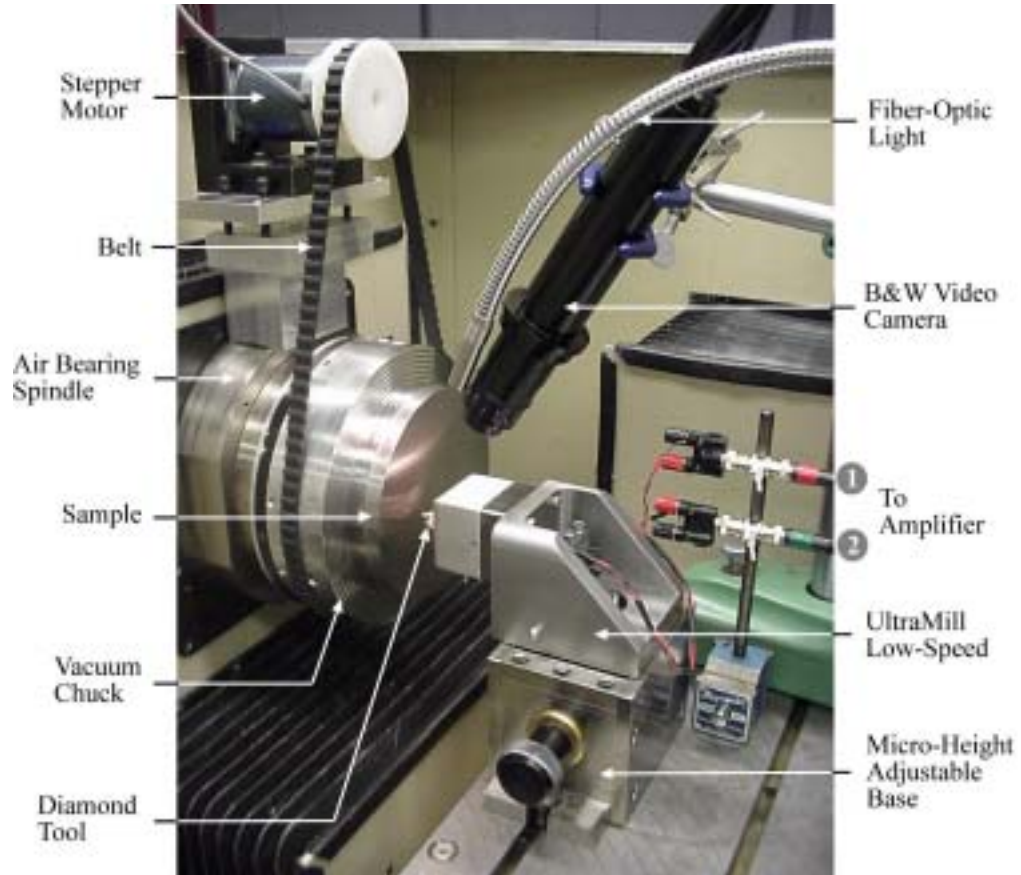


Figure 4.3: Close-up View of UMLS Mounted on DTM for Cutting Trials

The method used to generate the drive signal for stack #1 and #2 is illustrated in Figure 4.4. Operating the UMLS starts at the DC voltage source (for equipment information, model number, etc., see Section 2.2.3). The negative portion of the sinusoidal drive signal must be avoided because piezoelectric material has a low tolerance for tensile stress. PZT expansion and contraction is proportional to positive and negative voltages respectively. To offset the signal, +4-volt from a DC voltage source is added to both of the signals. The complete output signal of the function generator is illustrated in the “Scope” window. In the case depicted here, the UMLS would be running forwards (ccw) since

stack #1 has the 90° phase shift included in its signal. The signal is then amplified 100x and delivered to the actuators. Unlike in Figures 4.2 and 4.3, where the workpiece mounted directly on the vacuum chuck for use in turning, Figure 4.4 shows the adapter used in force experiments secured to the chuck. The specifics of this adapter will be discussed in Section 4.2.

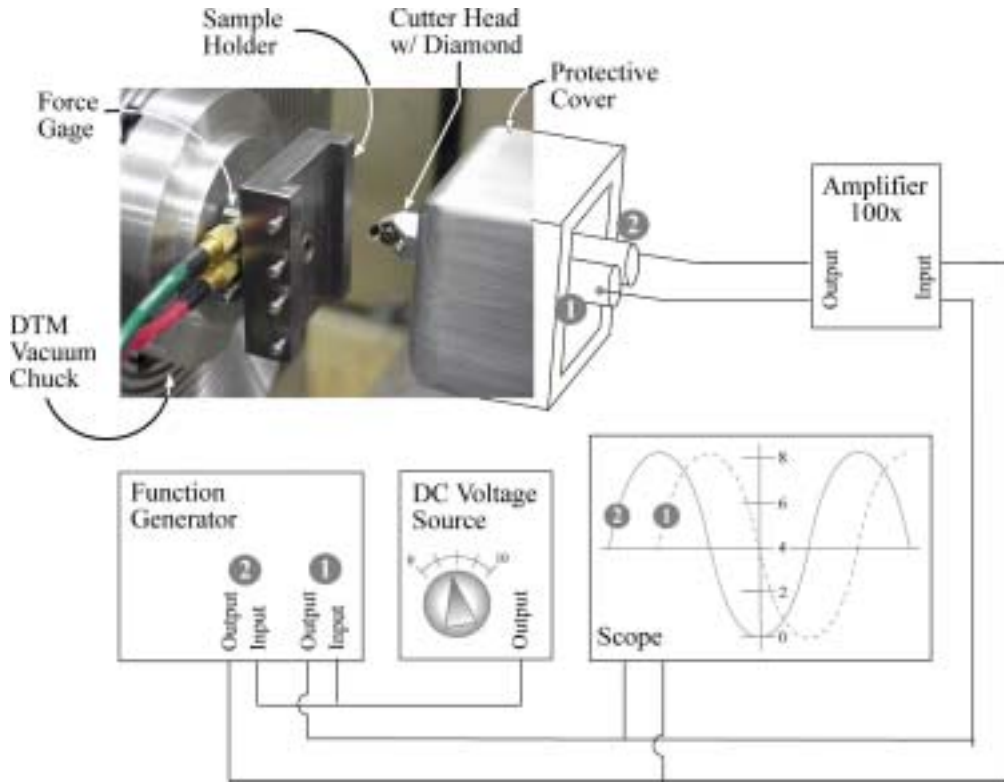


Figure 4.4: Wiring Schematic of UMLS

4.0.3 HSR Setup: Turning

Upon selecting a horizontal speed ratio (HSR) based on the 2D VAM duty cycle, the depth of cut and the desired surface finish, Rt_{xy} , the needed workpiece velocity can be calculated with Equation (9). Equation (50) replaces $v_{critical}$ with its mathematical expression, Equation (10), and solves for v_w . f_{UM} is the operational frequency of the UMLS and a is the major axis of the elliptical tool path.

$$HSR = \frac{v_w}{v_{critical}} \quad (9)$$

$$v_w = v_{critical} \cdot HSR = 2\pi f_{UM} \cdot a \cdot HSR \quad (50)$$

For use on the diamond turning machine, the spindle rotational velocity, ω_2 , at a given radius, r , from the spindle center must be determined. With a known cut radius and up-feed velocity, the spindle speed is found by,

$$\omega_2 = \frac{V}{r} \quad (59)$$

with the units being radians per second. However, since the stepper motor drives the air bearing spindle, the stepper velocity must be calculated. Figure 4.5 depicts the geometric relationship between the two spindles.

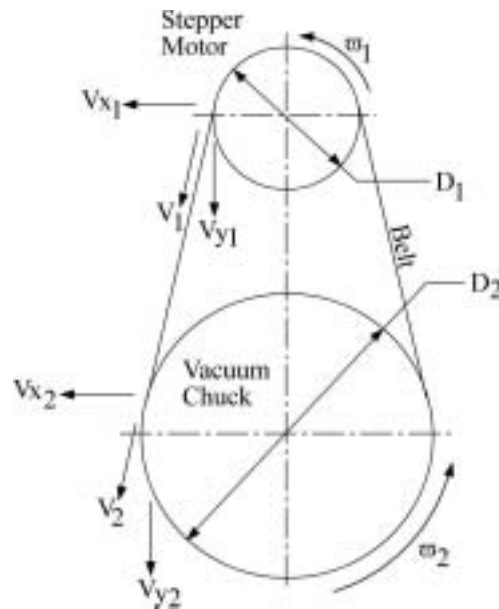


Figure 4.5: Schematic of Spindle Drive Arrangement

The spindle drive schematic (Figure 4.5) defines the stepper rotational velocity, ω_1 , equal the DTM spindle speed multiplied by a ratio of the two spindles radii.

$$\omega_1 = \frac{r_2}{r_1} \omega_2 \quad (63)$$

where ω_2 is in radians per second and,

$$r_n = \frac{D_n}{2} \quad (64)$$

is the radius of the spindle in mm for the either spindle, n=1 or 2.

4.1 SURFACE TOPOGRAPHY

Using the UMLS as a standard tool post, a flat (1100 aluminum) was turned with the tool stationary to establish a baseline surface roughness. With a 1 mm radius diamond tool, a cross-feed, of 0.5 mm per min and a spindle rotational speed of 500 rpm, a Peak to Valley surface roughness, Rt_{zy} , of 14 nm was obtained. The theoretical Rt_{zy} value given these machining parameters is 1.25 nm. With rotational speed of the spindle 2+ orders of magnitude greater than the spindle speed during vibration cutting, this surface roughness represents the best surface finish obtainable. Figure 4.6 is the surface profile of the flat as measured on a Zygo[®] White-light Interferometer.

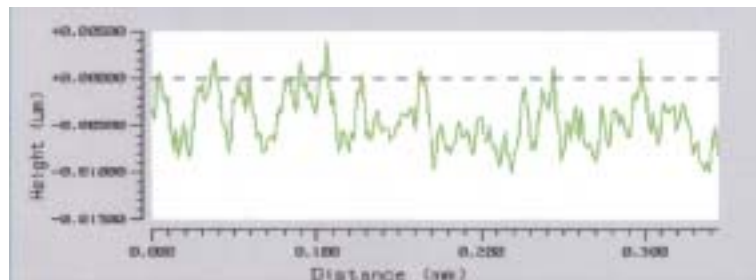


Figure 4.6: Surface Roughness of Turned 1100 Series Aluminum Surface
 ($Rt_{zy} = 14 \text{ nm}$, $rms = 3 \text{ nm}$, $Ra = 2 \text{ nm}$, $f = 0.5 \text{ mm/min}$, $\omega_2 = 500 \text{ rpm}$)

4.1.1 Surface Features

4.1.1.1 Phase

Holding constant the spindle rotation, the cross-feed, f , and the UM drive frequency, f_{UM} , the “scoop” features left in the surface of the workpiece begin to overlap as the distance between the tool and the lathe centerline decreases. How the surface features of adjacent rows relate to each other was defined as phase (Section 3.2). This progression is pictured in Figure 4.7.

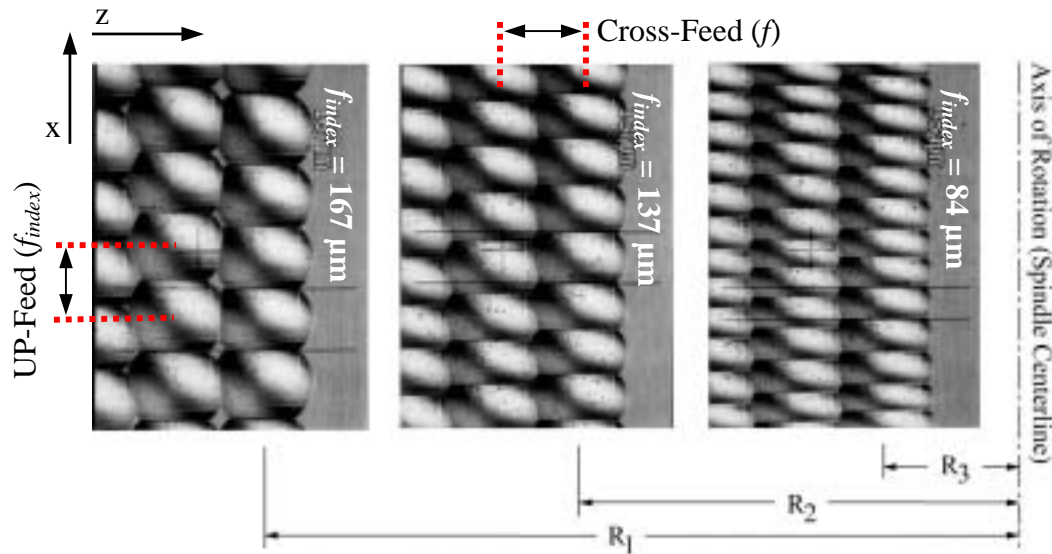
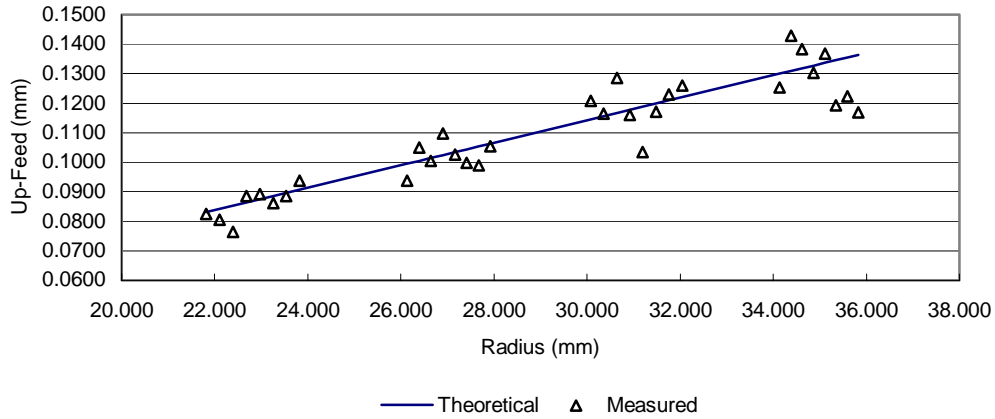


Figure 4.7: Overlapping of Surface Features w/ Decreasing Part Radius
($R_1 = 38 \text{ mm}$, $R_2 = 30 \text{ mm}$, $R_3 = 22 \text{ mm}$)

The overlap in the direction of cross-feed, decreasing z -axis, remains constant. The extent of the overlap depends on the ratio of the cross-feed to the width of the cut, which is controlled by the radius of the tool and the depth of cut. As long as this ratio is less than or equal to one, the cuts will overlap in the z -axis.

For a constant rpm, the further away the tool is from the center of the part (increasing radius, $R_1 > R_2 > R_3$) the greater the distance (circumference) that must be traversed per spindle rotation. With a fixed amount of cuts per second (example: $f_{UM} = 400 \text{ Hz} = 24000 \text{ cuts per min.}$), this increasing circumference results in an increasing up-feed, f_{index} . After adjusting for the increased up-feed distance, it was found that the f_{index} length was

maintained to within 6.3% of the theoretical value. Figure 4.8 plots the up-feed variation from theoretical for the corresponding radius from the part center.



*Figure 4.8: Up-Feed Variation From Theoretical Value
 $(f_{UM} = 55 \text{ Hz} / \omega_2 = 2 \text{ rpm} / 1100 \text{ Aluminum})$*

Since the up-feed is not held constant, the amount of phase between rows shifts. At R1, the relation of up-feed to cross-feed produces a surface with 0 phase. As the part radius decreased, up-feed increased until at R3, the feed ratio produced a surface with a phase of 0.5. From the discussion of the effects of phase on surface roughness, Section 3.2, the surface roughness at R1 will be greater than that at R3.

4.1.1.2 Up-feed

To remove the effects of phase and perform a more detailed comparison between the theoretical up-feed and that produced by the UMLS, multiple straight line cuts were made in both 6061 Aluminum and C110 Copper samples. The theoretical up-feed distance was given by Equation (15). The operational frequency of the UltraMill was 10 Hz and the HSR was varied between 0.01 and 0.075, a duty cycle variation of 22% to 25%. Figures 4.9 and 4.10 picture the in-line cuts with their corresponding surface profile measurement taken with the Zygo[®] Interferometer down the center of the cut for 0.350 and 0.075 HSR respectively

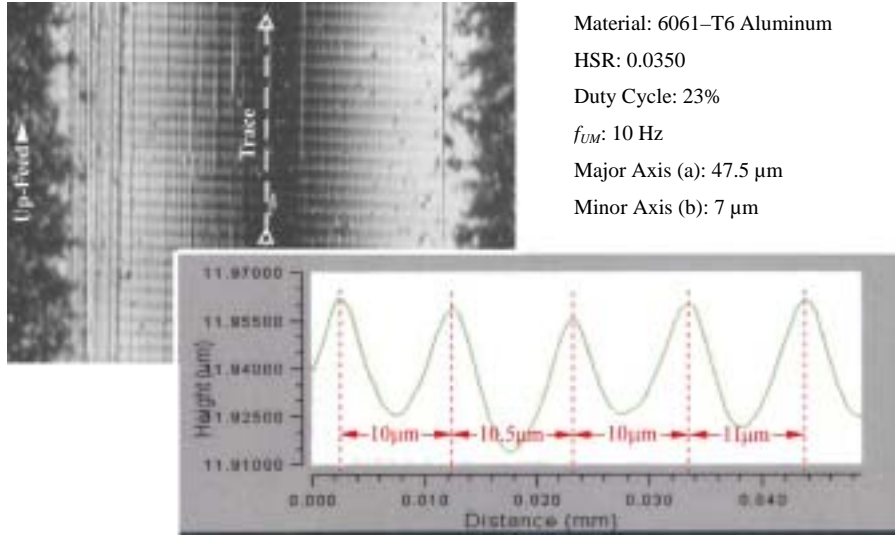


Figure 4.9: Surface Profile of a 0.035 HSR, 23% Duty Cycle Cut

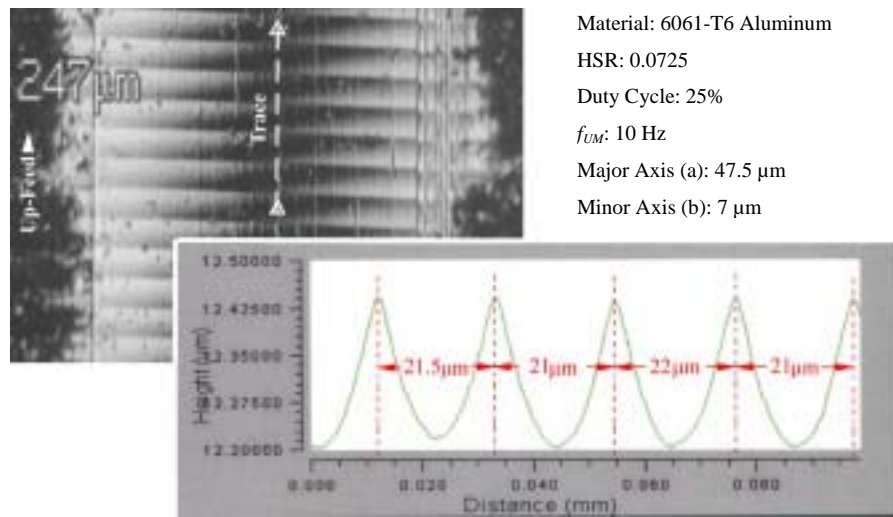


Figure 4.10: Surface Profile of a 0.075 HSR, 25% Duty Cycle Cut

On top of the surface profile measurements is the spacing between peaks. This spacing is the distance indexed per cycle, f_{index} . For a 0.035 HSR with the indicated cutting frequency and major axis displacement, Equation (15) states that index distance should be 10.446 μm . As can be seen, this agrees with the measured values in Figure 4.9. The same can also be said of the 0.0725 HSR cut in Figure 4.10, where the theoretical index distance is 21.638 μm .

4.1.1.3 Apparent Tool Radius

The last surface feature to be examined is that of the projected tool shape, discussed in Section 3.1.2. To investigate the oscillatory effect of the tool as it approaches the center of the part, fourteen 12 mm flats (7 copper and 7 aluminum) were turned, half with the UltraMill acting as a standard tool holder (static) and half with the UltraMill in operation (active). Figure 4.11 compares two representative samples, a standard turned piece and a vibration turned piece.

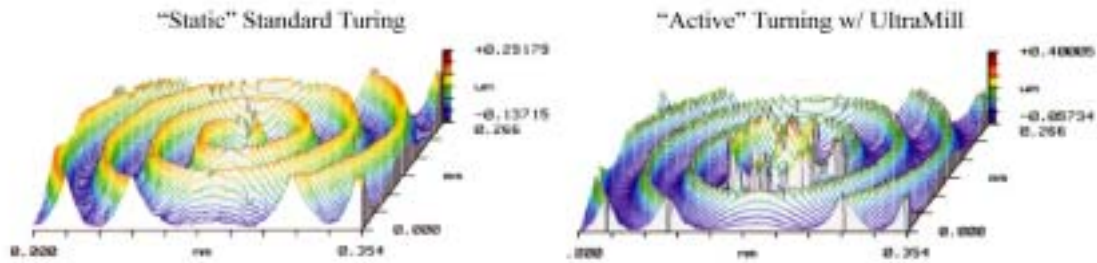


Figure 4.11: Oblique Plots of Turned Copper Flats
(1 mm radius tool, 2 rpm, $x\text{-}f = 0.1$ mm/min, depth = $1\ \mu\text{m}$, $f_{UM} = 200$ Hz)

All the flats were turned using a 1.02 mm radius diamond tool at a spindle speed of 2 rpm, a cross-feed of 0.1 mm per min and a depth of cut approximately $10\ \mu\text{m}$. The cutting frequency for the “active” cuts was 200 Hz. The standard turned surface had a peak to valley surface roughness, R_t , of $0.427\ \mu\text{m}$. The vibration turned surface had an R_t of $0.331\ \mu\text{m}$. A 22 % reduction is peak to valley surface roughness. As predicted in Chapter 3, the projected tool shape of the VAM servo reduces the surface roughness at the center of the part by removing the peaks of the preceding rows. The complete surface roughness values are presented in Section 4.1.2.

4.1.2 Metrology: Surface Roughness and Form Error

The surface roughness of all fourteen copper flats was measured in two directions: Angular and Radial using a Zygo® White-light Interferometer. Figure 4.12 illustrates the trace orientations.

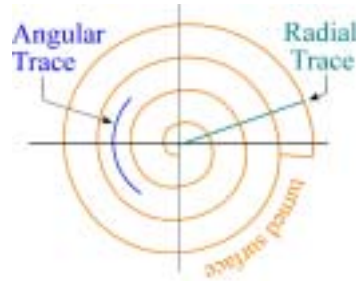


Figure 4.12: Definition of Trace Paths

The trace data showed a 19% reduction in radial peak-to-valley surface roughness and a 74% percent reduction in angular peak to valley surface roughness when the UltraMill was active. Figures 4.13 and 4.14 are surface profiles of the angular traces of the two samples shown in Figure 4.11. The peak-to-valley surface roughness decreased from 17 nm for the standard sample to 4 nm for the VAM sample.

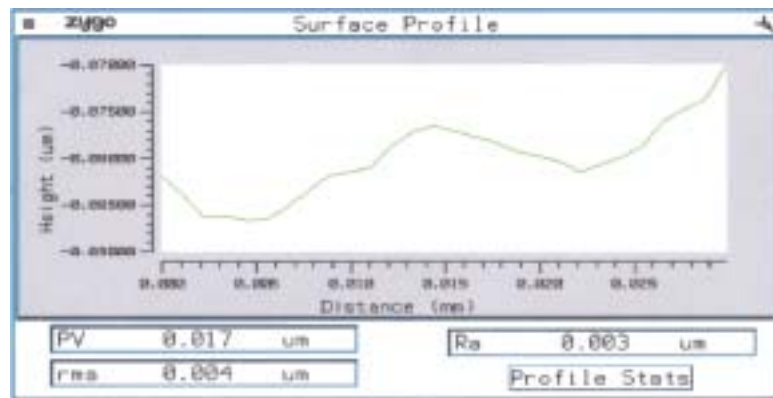


Figure 4.13: Angular Trace of Standard Turned Flat
(Copper, 1 mm radius tool, $f = 0.1$ mm/min, 2 rpm, depth = $1\mu\text{m}$)

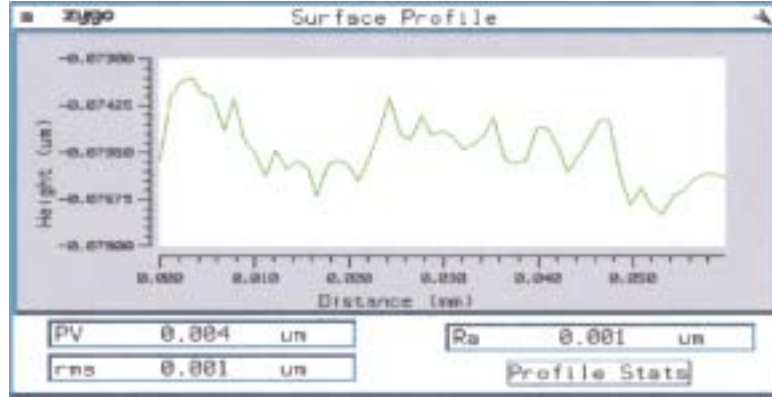


Figure 4.14: Angular Trace of VAM Turned Flat
(Copper, 1 mm radius tool, $f = 0.1$ mm/min, 2 rpm, depth = $1\mu\text{m}$)

Form measurements were taken of these parts using a Zygo[®] GPI Laser Interferometer. For the parts turned with a stationary tool, the surface / wavefront profile data ranged from $0.21\ \mu\text{m}$ to $0.84\ \mu\text{m}$ peak to valley and $0.04\ \mu\text{m}$ to $0.23\ \mu\text{m}$ RMS over a radius of 0.25 mm from part center. The form error of the VAM turned flats was slightly larger, ranging from $0.25\ \mu\text{m}$ to $1.14\ \mu\text{m}$ peak to valley and $0.08\ \mu\text{m}$ to $0.31\ \mu\text{m}$ RMS.

The extent to which the actual up-feed surface roughness mirrors the theoretical value established by Equation (17) was determined by making in-line cuts for HSR's of 0.010, 0.0350 and 0.0725. The results are tabulated in Table 4.2.

$$Rt_{xy} = \frac{bf_{index}^2}{8a^2} \quad (17)$$

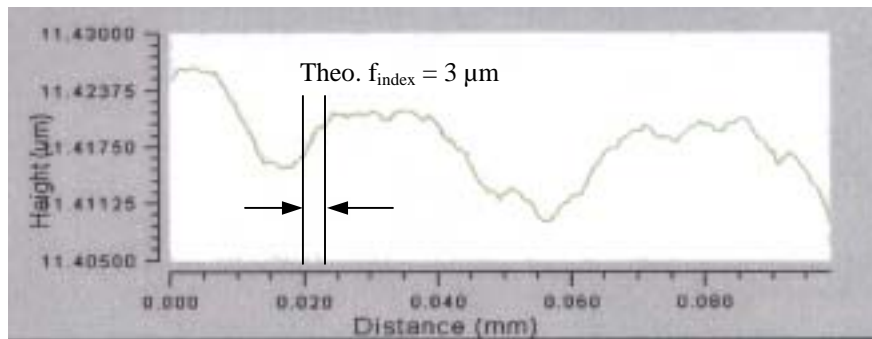
Table 4.2: Surface Roughness Comparison (Angular)

HSR / Duty Cycle	f_{index} (μm)	Theoretical	Measured	
		Rt (nm)	Rt (nm)	Ra (nm)
0.01 / 22%	2.985	3.6	17	3
0.035 / 23%	10.446	44.1	45	13
0.0725 / 25%	21.638	189.2	244	68

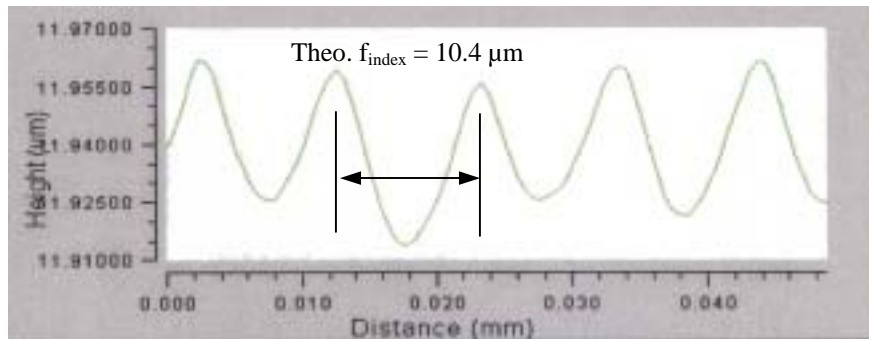
While informative, the surface roughness numbers fail to give a complete picture of duty cycle based vibration assisted machining. Figure 4.15 shows the surface trace associated

with each HSR in ascending order. At HSRs of 0.035 and 0.0725, the dominant feature is due to the elliptical tool path, the major and minor axis of the ellipse and the up-feed. At 0.01 HSR however, this is not the case. There is no trace of the tool path geometry. The surface roughness is a result of the material shearing from the workpiece as it is in standard diamond turning. So at 0.01 HSR, the surface finish of a vibration cut part is identical to that of a non-vibration cut part.

A) HSR = 0.0100



B) HSR = 0.0350



C) HSR = 0.0725

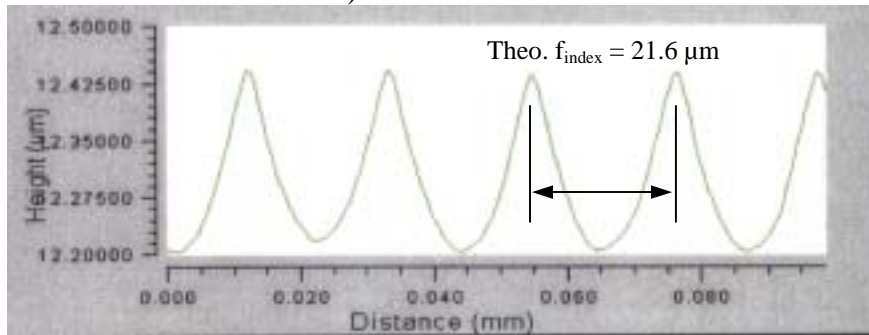


Figure 4.15: Change in Surface Profile with HSR

The surface finish at 0.010 HSR shows that 2D VAM is capable of creating surface finishes without imprinting the elliptical tool path into the workpiece. This surface finish could be obtained at higher HSRs if the major to minor axis ratio of the elliptical tool path were increased (7:1 for the UMLS). Increasing the HSR would also reduce the machining time by increasing the feed rate, f_{index} .

4.2 FORCE MEASUREMENT

Elliptical cutting force measurements were taken for three materials, C110 Copper, 6061-T6 Aluminum and 1018 Steel. The physical properties of which are tabulated in Table 4.1. Sample work pieces were fabricated out of standard bar stock. These material segments had dimensions 3 inches long x 1 inch wide x ¼ inch thick. The ASG-2500 DTM was used in order to capitalize on its high level positioning accuracy. A steel plate was used to secure the air-bearing spindle and keep it from rotating.

A specially designed sample holder was mounted on the vacuum chuck. This holder is pictured in Figure 4.4. Figure 4.16 provides an exploded view of the sample holder.

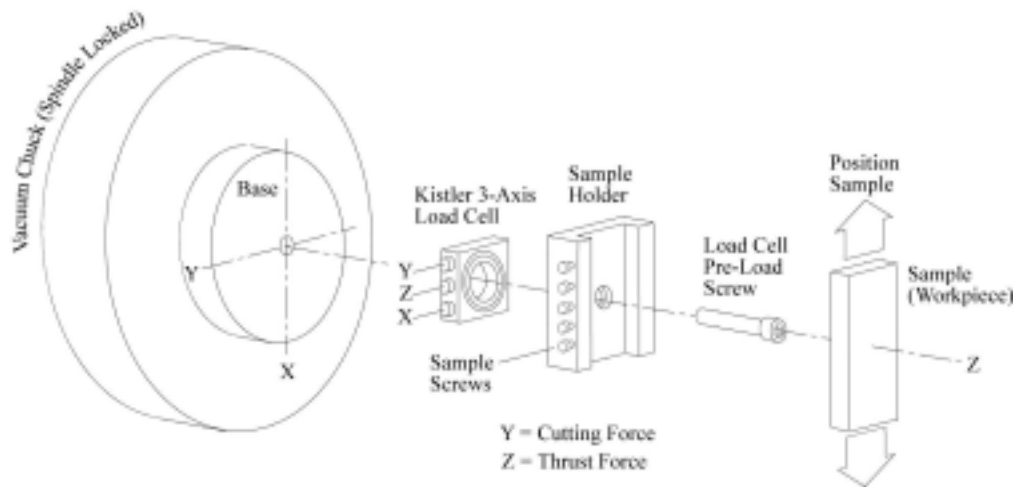


Figure 4.16: Exploded View of Sample Holder Used to Measure Cutting Forces

The sample holder consists of four parts: base, load cell, sample holder and load cell pre-load screw. The base is a turned steel disk that was designed with sufficient area to securely mount on the vacuum chuck. Its thickness, approximately 1 inch, mitigates any base deflection resulting from cutting forces. Centered on the base is a Kistler Model 9251A 3-axis load cell. The “y” and “z” axis of the load cell are aligned with the cutting and thrust force directions respectively. The load cell is wedged between the base and the sample holder. All three components are tied together with a steel screw. The screw serves a dual purpose by also providing the manufactures recommended preload to the load cell. Since the load cells stiffness is several orders of magnitude greater than the screw, any influence the screw may have on the force reading is negligible. The sample holder allows for the workpiece to be adjusted vertically and then locked into position with a series of screws.

4.2.1 Elliptical Vibration Machining Force Data

Cutting trails were performed for 22%, 23% and 25% 2D duty cycles at a depth of cut equal to 6 μm . For these tests, the UMLS was driven at 10 Hz. Mounted in the head of the UltraMill was a 3 mm radius diamond tool with an estimated edge radius of 300 nm. Figure 4.17 plots the recorded data for a Class B in-line chip.

Aluminum and steel cutting trails produced cutting and thrust force plots similar to that of the copper trial shown in Figure 4.17. As a result of the material hardness and material shear angle, different peak forces were produced. The peak values of all the materials as well as the calculated conventional turning forces for work-hardened material are compiled in Table 4.3.

*Table 4.3: Recorded Peak Elliptical Cutting Forces
(6 μm depth of cut, 3 mm radius tool, worn tool edge)*

Peak Force Data						
HSR / Duty Cycle	Copper (C110)		Aluminum (6061-T6)		Steel (1018)	
	Cutting [N]	Thrust [N]	Cutting [N]	Thrust [N]	Cutting [N]	Thrust [N]
0.0100 / 22%	0.40	0.67	0.48	0.88	0.70	1.21
0.0350 / 23%	0.70	0.71	0.83	0.93	1.23	1.28
0.0725 / 25%	1.05	0.83	1.26	1.09	1.85	1.49
Standard Turning	2.44	1.29	2.51	1.52	3.82	2.00

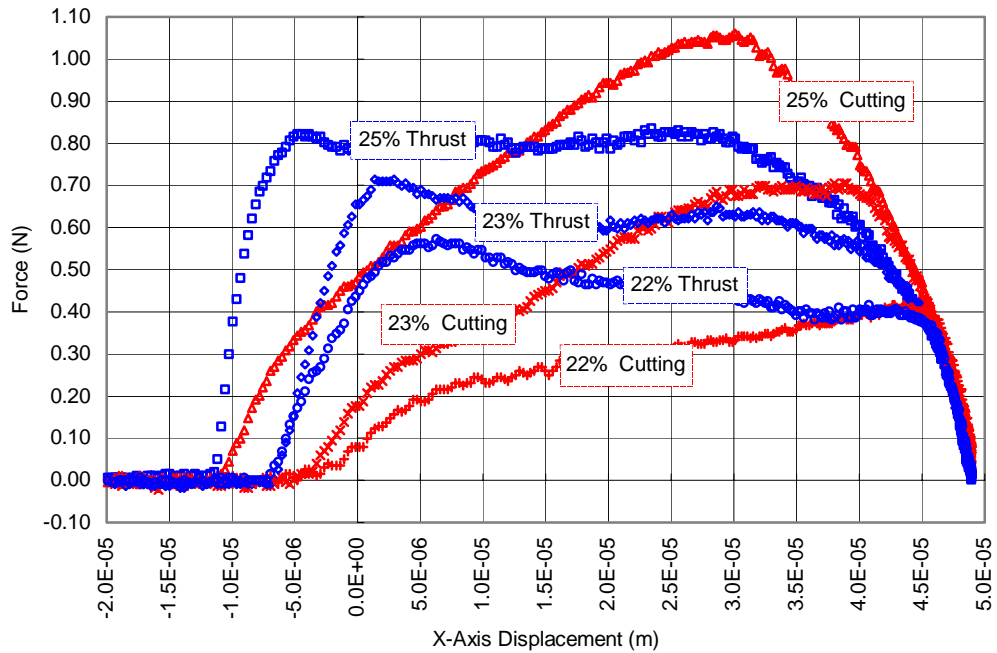


Figure 4.17: Duty Cycle Force Data for C110 Copper
 (6 μm depth of cut, 3 mm tool nose radius, $f_{UM} = 10$ Hz, worn tool edge radius,
 DAQ freq. = 10 kHz per channel)

4.2.2 Comparison to Model

The measured copper force data presented in Figure 4.17 separated and plotted with the predicted machining forces for each individual duty cycle: 22% (Figure 4.19), 23% (Figure 4.20) and 25% (Figure 4.21). The key features to note when comparing the model to the test data are:

- The transition point between the cutting and thrust force.
- The shape of the back slope.
- The length of the cut, starting point and ending point
- The large thrust force
- The thrust force top slope

Figure 4.18 illustrates the key features. The point in the cutting cycle where the thrust force and cutting force exchange force dominance is the transition point. The shape of the

back slope is representative of the elliptical tool path. The start of the chip is at the predicted f_{index} distance to the left of $x = 0$. Lastly, the large thrust force resulting from the minimum depth of cut not being meet. Followed by its decay as the tool's frictional area, A_{fric} , is reduced with the diminishing tool edge contact area.

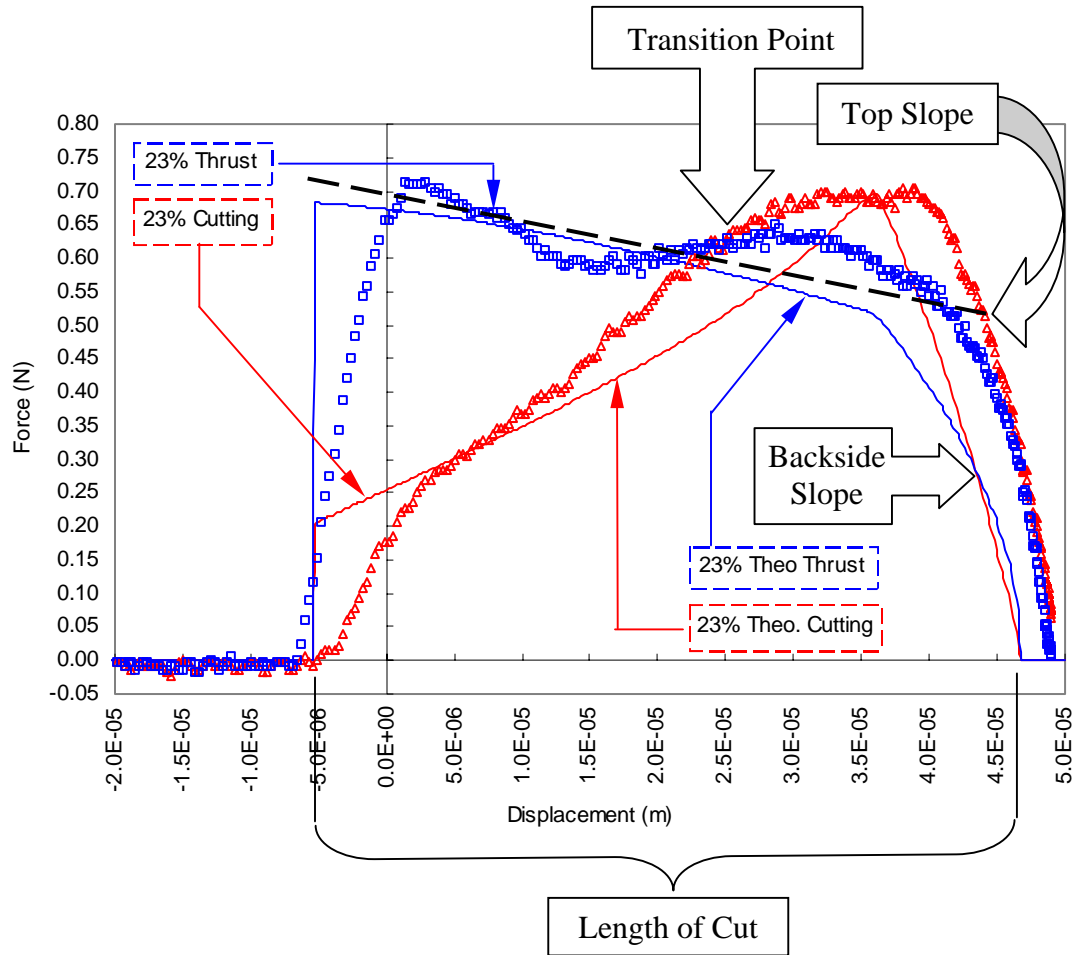


Figure 4.18: Illustration of Key Machining Force Features
23% 2D VAM Copper Case

Agreement between the measured machining forces and the predicted forces is good. The theoretical length of cut also proved to be representative of the recorded data. The accuracy of the predicted peak forces and predicted chip length is compiled in Table 4.4.

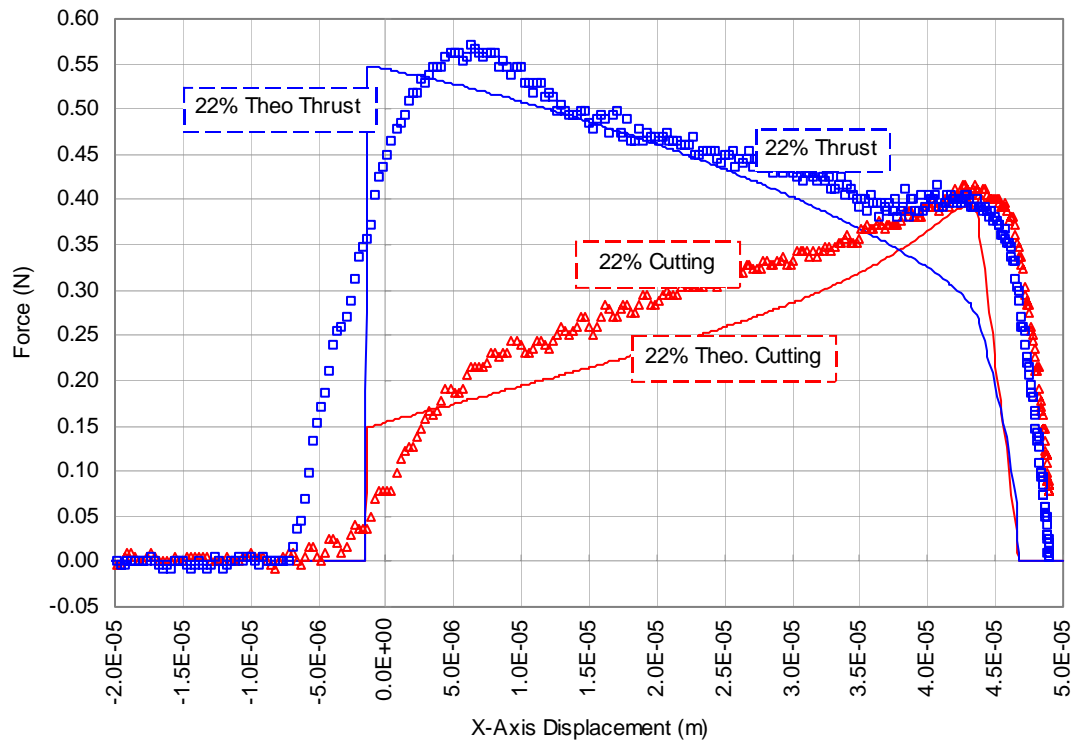


Figure 4.19: Measured / Predicted Forces for 22% 2D VAM

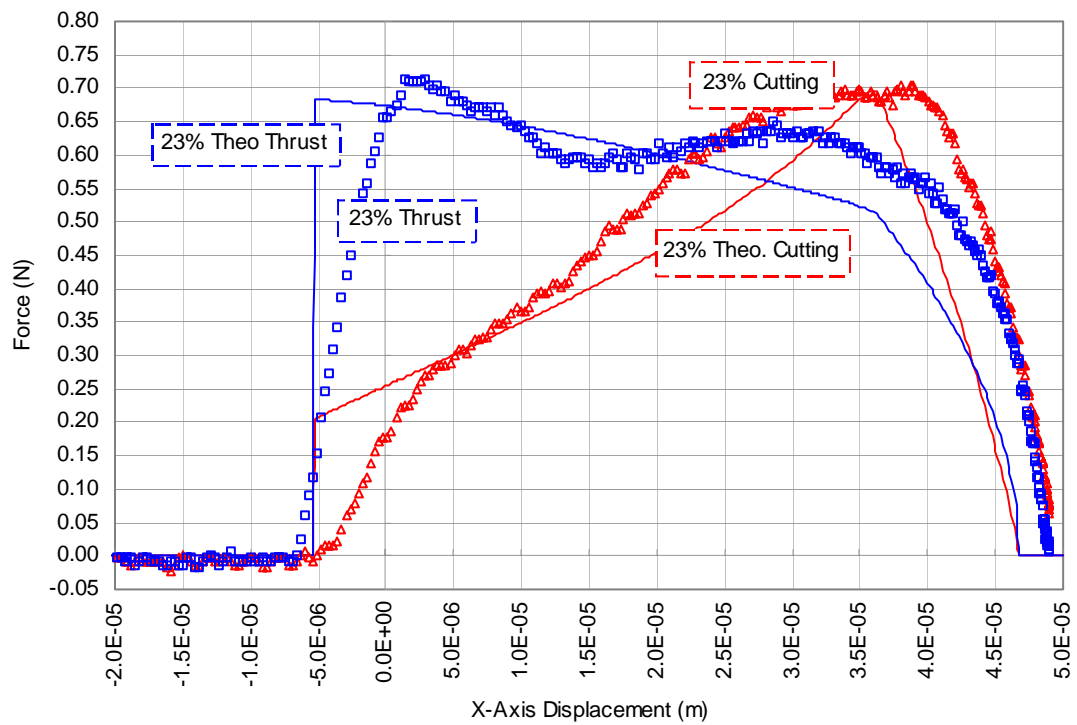


Figure 4.20: Measured / Predicted Forces for 23% 2D VAM

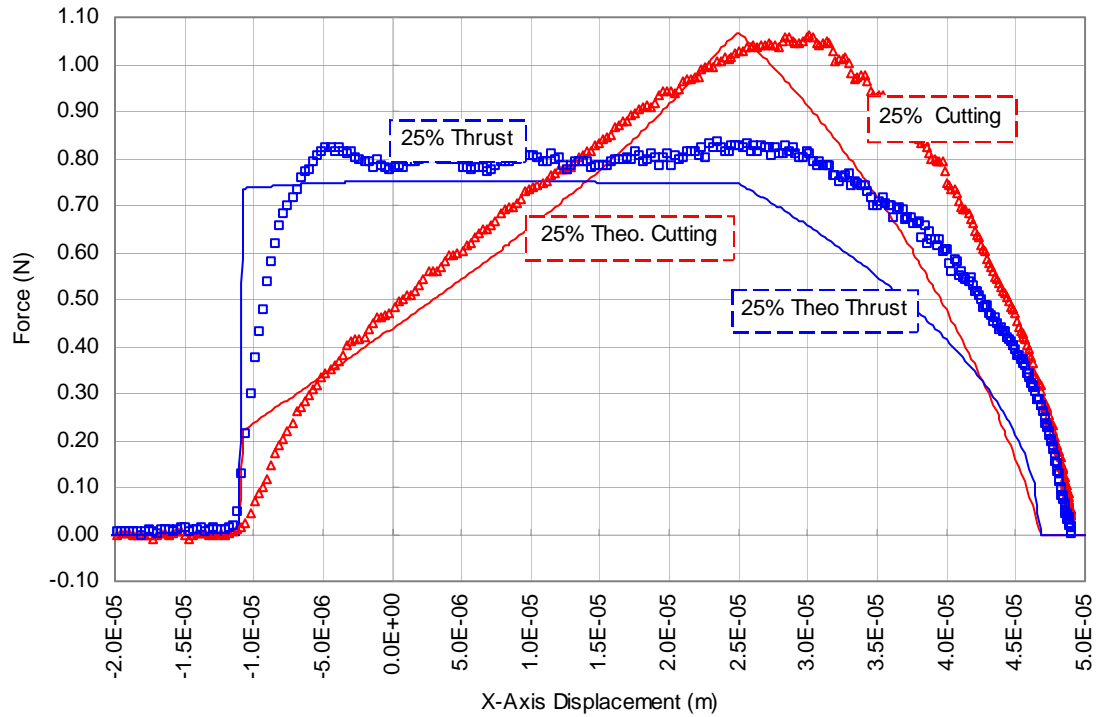


Figure 4.21: Measured / Predicted Forces for 2D VAM

The model predicted the force transition point to within 6 μm of the measured value. For 22%, 23% and 25% the measured transition points were 42 μm , 25 μm and 13 μm respectively. The measured chip length for each duty cycle varied by no more than 8% from the theoretical. Deviation between the chip length measured data and the prediction is most likely a result of minor deflection of the servo's tool head. Lastly, the elliptical cutting model correctly predicts both the shape of the back slope and the top of the thrust force curve.

Table 4.4: Prediction Accuracy for Peak Machining Forces and Chip Length

HSR / Duty Cycle	Peak Cutting Force [%]	Peak Thrust Force [%]	Chip Length [%]
0.0100 / 22%	98	96	90
0.0350 / 23%	99	95	96
0.0725 / 25%	99	89	95

Along with the key shape features, the Figures 4.19 – 4.21 show the ability of the PEC VAM model to predict the magnitude of the machining forces. The peak cutting forces agreed with the predicted values to within 4%. While good, the accuracy of the thrust force prediction tended to lessen as the HSR increased, from 96% at 0.01 to 89 at 0.0725. Since optical quality surface production ($PV < 50$ nm) requires an HSR of 0.035 or less, Table 4.2, the cutting geometry approximations, such as shear angle, made in the PEC VAM model prove adequate.

4.2.3 Benefits of a “Sharp” Tool

The preceding cuts were made with a moderately worn tool, a tool with an edge radius of approximately 300 nm. The machining model presented in Chapter 3 states a sharper tool, one with an edge radius of 40 to 60 nm, would result in lower machining forces. To verify the validity of this statement, the 3 mm radius diamond tool used in the above experiments was replaced with a new 0.5mm radius diamond tool and a 23% 2D VAM cut was made in copper. The results of this trial are plotted in Figure 4.22.

Figure 4.22 shows agreement between the force model and the measured data. Note that unlike the trial with the “used” tool, the cutting and thrust forces never transition. The cutting force is always dominant. This is to be expected since the “sharp” tool, with an estimated edge radius, R_{edge} , of 40 nm, starts to shear the material at a shallower material penetration depth than that of a used tool. Illustrated in Figures (3.8) and (3.12), reducing the depth at which the tool’s edge is below the surface of the material would reduce the frictional contact area, A_f . Recall from Equations (21) and (22) that machining forces are directly proportional to frictional area, thus a smaller A_f would produce lower machining forces. A smaller edge radius will lower all machining forces due to reduced work hardening

The prediction accuracy of machining forces using a sharp tool was 94% in both the cutting and thrust directions. Although this percentage is not as high as the trials involving

a dull tool, this trial required no adjustment in material properties for work hardening. Using the accuracy of this trial as a base, the predicted peak cutting and thrust forces for a “sharp” 3 mm diamond tool operating at 0.035 HSR and a 6 μm depth of cut in C110 Copper are 0.38 N and 0.13 N respectively. Compared with the recorded trial data, Table 4.3, using a 3mm “dull” tool shows the sharp tool to reduce machining forces by 46% in the cutting direction and 82% in thrust direction.

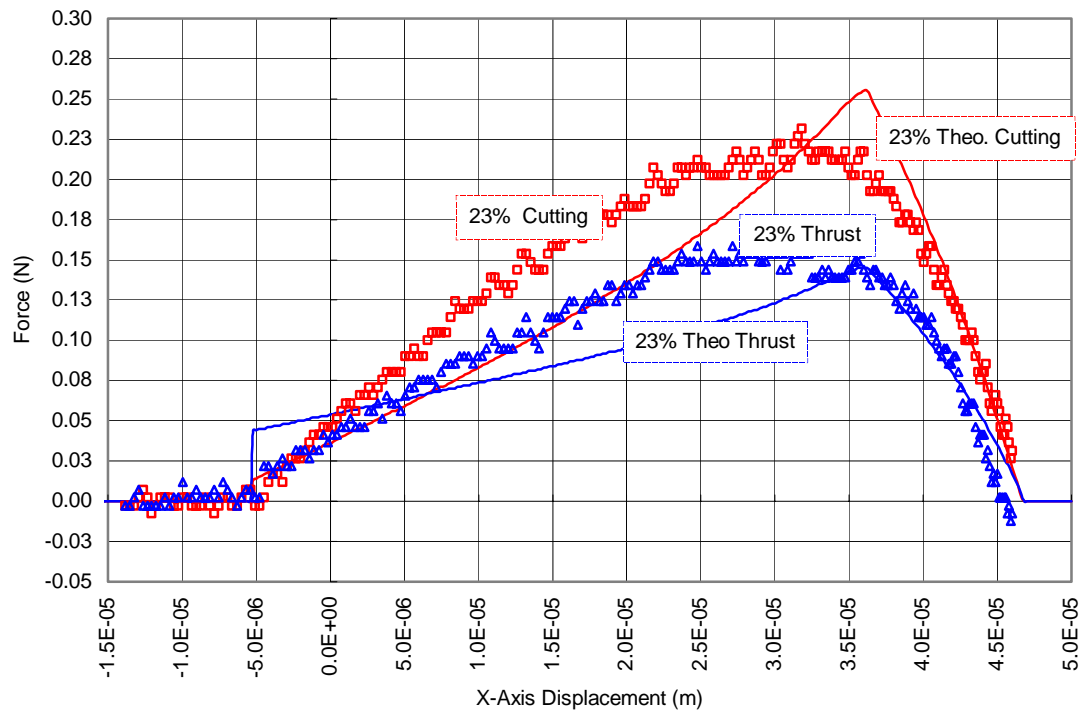


Figure 4.22: Reduction in Machining Forces Due to a Sharp Tool (C110 Cu, 6 μm depth of cut, $R_{edge} = 0.5 \text{ mm}$, sharp tool, $f_{UM}=10 \text{ Hz}$)

4.2.4 Discussion of Vibration Assisted Machining Results

VAM removes the same volume of material as that of a conventional machining per unit time. The advantage of VAM is that the thickness of the chip that is removed per cutting cycle is smaller than the depth of cut. In non-vibration cutting all material is removed at one time. During this time, a 6 μm depth of cut is equivalent to a chip thickness of 6 μm . In elliptical vibration machining, which consists of tens to thousands of cycles per second, a 6 μm depth of cut with a 22% 2D VAM duty cycle is equivalent to a peak chip

thickness of 1.5 μm . As a result, the volumetric contact between the tool and workpiece is reduced and with it the time averaged machining forces. But at the same time, the sliding distance of the tool is increased. Therefore the energy required to remove the material is the same in both 2D VAM and conventional machining

VAM has been shown to produce forces that are substantially lower than that of standard machining given a sharp tool. The trials have produced machining forces that are on average 50% lower than those of conventional machining.

The PEC developed VAM model can predict both the shape and magnitude of the machining forces. Although the forces involved in diamond turning are small, as manufactures continue to shrink the size of components, they will become critical. To achieve a lower level of cutting force one option is VAM. The use of the PEC model should allow for quick calculation of machining forces.

4.3 VIBRATION ASSISTED MACHINING OF STEEL WITH DIAMOND TOOLS

Achieving an optical quality surface, $R_a < 50 \text{ nm}$, on iron and steel materials is difficult without the use of a post polishing step. The need for an additional step can be not only cost prohibitive, but also size restrictive in the case of micro-structured parts [5]. Surface finishes of this magnitude are common place in diamond turning, however the diamond turning of steel alloys is impractical due to severe tool wear [4].

4.3.1 Tool Wear and VAM

Research has shown that an optical surface is possible on carbon containing materials with the use of a monocrystalline diamond articulated with a VAM servo [4-7]. Tool wear has been demonstrated by Brinksmeier [4] to be a function of contact time. It is postulated that the contact time between the diamond and carbon containing workpiece is such that heat generation at the interface is insufficient in magnitude and time to cause chemical abrasion. Evans [21] compared the diamond machinability of various materials with the their atomic structure. His research suggests that unpaired d-electrons of iron containing materials are responsible for the break up of carbon bonds in the diamond

lattice. Research carried out at North Carolina State University bolsters Evans contention by theoretically and experimentally attaching a temperature at which solid-state diffusion occurs [1].

Combining the results of the cited literature, it is concluded that the primary wear mechanism of vibration assisted machining is a result of abrasive wear as oppose to chemical wear [21]. Since abrasive wear is more than an order of magnitude less than chemical wear, VAM of ferrous metals becomes possible.

The experimental work carried out at the PEC serves to add to the growing body of evidence that steels can be successfully diamond turned as well as to investigate tool wear in non-ultrasonic vibration diamond turning. Until now, all previous research had utilized ultrasonic cutting frequencies, those greater than 20 kHz [4-8]. These earlier trails also used cutting amplitudes 10X smaller than those of the UltraMill. The question, “Are good surface finishes and long tool life possible at low frequencies?”, will be answered.

4.3.2 Experimental Setup

Tool steel (AISI Type W2) was chosen over mild steel such as 1018 because the area of application, i.e. injection die molds, would typically use the harder material. The ASG-2500 DTM was configured for turning with the UMLS. This arrangement was described in Section 4.0.2 and can be seen in Figure 4.3. Two sets of cutting trails would be performed, one with the UltraMill active and one with the UltraMill acting as a standard tool post.

Two identical, new 0.5 mm radius monocrystalline diamond tools were used, one for each trial. Inspecting the rake face of the diamond at equal cutting intervals with an Olympus BH2-UMA optical microscope would serve to catalog any tool wear. A white-light interferometer was used to correlate surface roughness with tool wear. Direct inspection of the rake face and indirectly quantifying tool wear by the decay in surface

finish quality are the methods used in previous trails [4-6]. Several attempts to AFM the diamond tips, but it was found to be inaccurate due to severe wear of the AFM probe tip.

4.3.3 Elliptical Vibration Cutting of Steel Results

Approximately 68 meters of steel was machined, 20 meters of VAM and 48 of conventional machining. Equal machining distances were not obtained due to equipment failure that cause and early end to the trial. The machining was done in two 5 mm bands, 16 mm and 22.5 mm from the center of the part. The cross feed was set to 0.05 mm/min and 0.02 mm/min for the conventional and VAM trails respectively. This results in the inner band of the conventional trail equaling the sum of the two VAM bands. Limiting analysis to these three bands allows for a comparison to be made.

Pictured in Figure 4.23 and 4.24 are the two steel sample pieces. A visual inspection of the surfaces shows the improvement that VAM parts have over conventionally turned parts. The radial and angular surface roughnesses are quantified in Table 4.5 and Table 4.6.

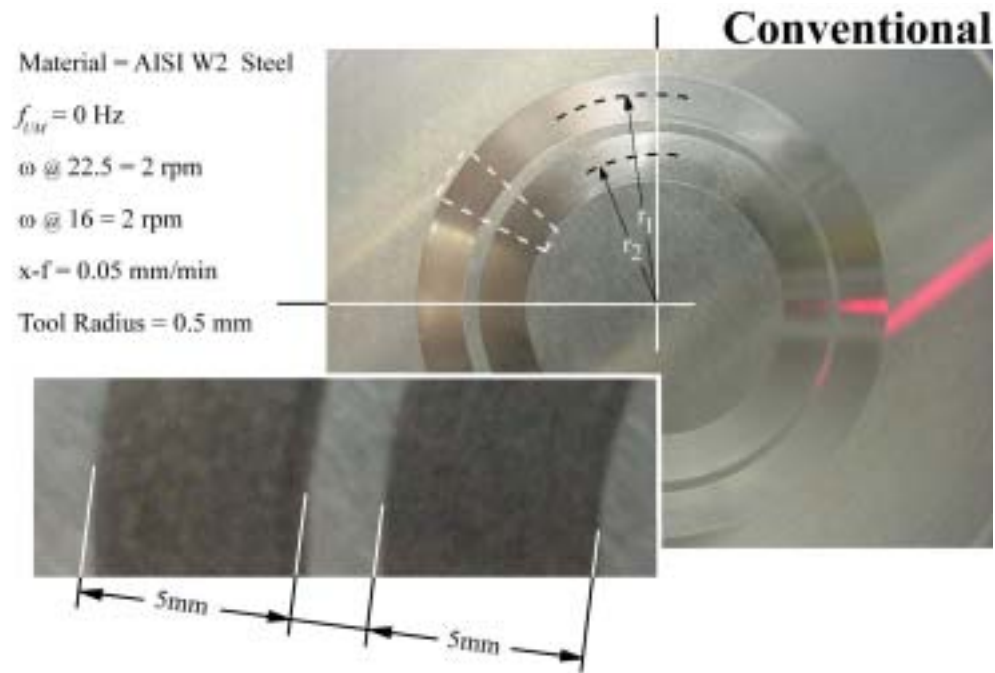


Figure 4.23: Photograph of Conventionally Diamond Turned Steel Surface

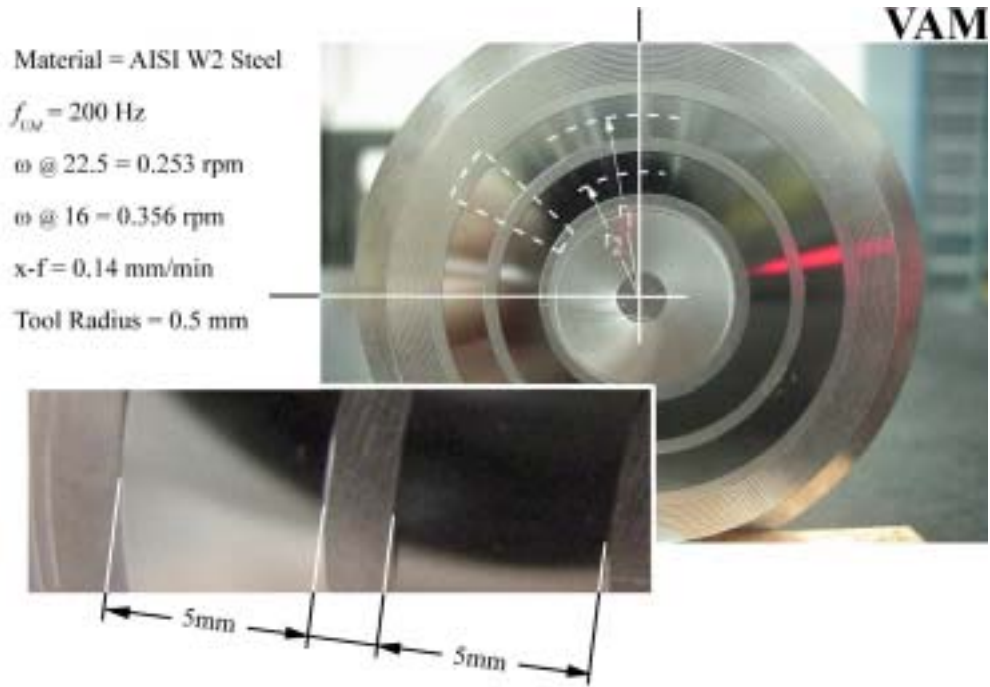


Figure 4.24: Photograph of Diamond Turned VAM Steel Surface ($HSR_{R1} = 0.0095$, $HSR_{R2} = 0.0090$, $d = 6 \mu\text{m}$, $a = 47.5 \mu\text{m}$, $b = 7 \mu\text{m}$)

Table 4.5: Radial Surface Roughness of Turned Steel Flats

Surface Roughness of Diamond Turned Steel Flat						
Pass	Radial [μm]					
	Standard			VAM		
	Rt	RMS	Theo. Rtzy	Rt	RMS	Theo. Rtzy
R ₁ (outer)	0.861	0.244	0.160	2.049	0.555	1.560
R ₂ (inner)	0.893	0.231	0.160	1.206	0.306	0.790

Table 4.6: Angular Surface Roughness of Turned Steel Flats

Surface Roughness of Diamond Turned Steel Flat						
Pass	Angular [μm]					
	Standard			VAM		
	Rt	RMS	Theo. Rtxy	Rt	RMS	Theo. Rtxy
R ₁ (outer)	0.161	0.034	0	0.024	0.006	0.003
R ₂ (inner)	0.115	0.028	0	0.034	0.008	0.003

A HSR of approximately 0.01 was chosen for the VAM trial. This was chosen to avoid the elliptical cutting path being imprinted on the workpiece surface (See Section 4.1.2 and Figure 4.15). The VAM peak to valley radial surface roughness, averaging 1.42x the theoretical R_t for the two passes, held closer to the theoretical surface roughness than did the conventional, which exceeded its theoretical level by 5x. The ability of VAM to more closely track the theoretical goal is seen even more in the angular trace data of Table 4.6. The VAM steel piece exceeded the theoretical goal by approximately 10x over both passes. Additionally, the VAM turned part maintained a lower surface roughness than the conventionally turned part over the same distance. This would suggest, 1) that VAM is not as effected by impurities and grain boundaries of the material as convention machining and 2) the VAM diamond experienced less wear or at least more even wear than that of diamond used in the conventional trial.

Figure 4.25 shows an oblique plot of the surface finish of the conventional steel flat at the end of the pass #2. The tool feed path is from the right to the left of the page. This saw-tooth pattern is a result of the chip not fully being removed by the diamond as it passes over the workpiece. The root of the chip fractures off, leaving jagged surface. As the tool passes from one row to the next, the jagged surface mechanically erodes the diamond tip. Figure 4.26 provides and SEM image of both tools at the ends of the two cutting passes.

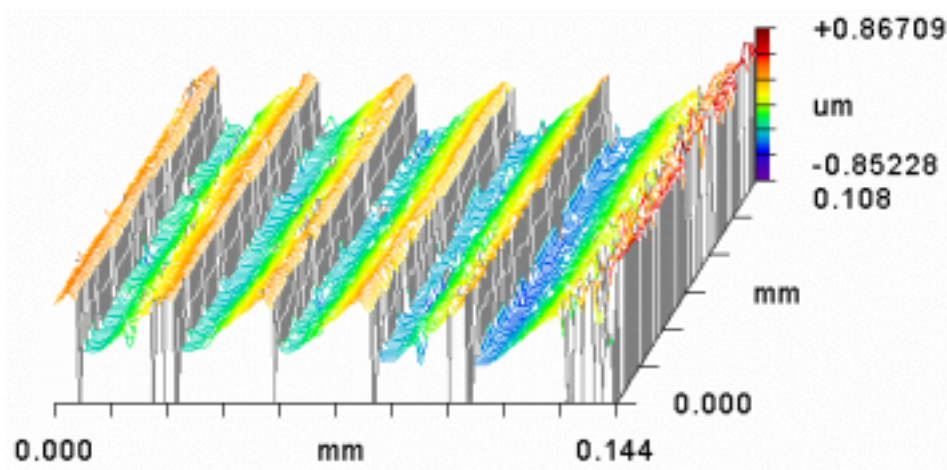


Figure 4.25 Oblique Plot of a Non-Vibration Turned Steel Part

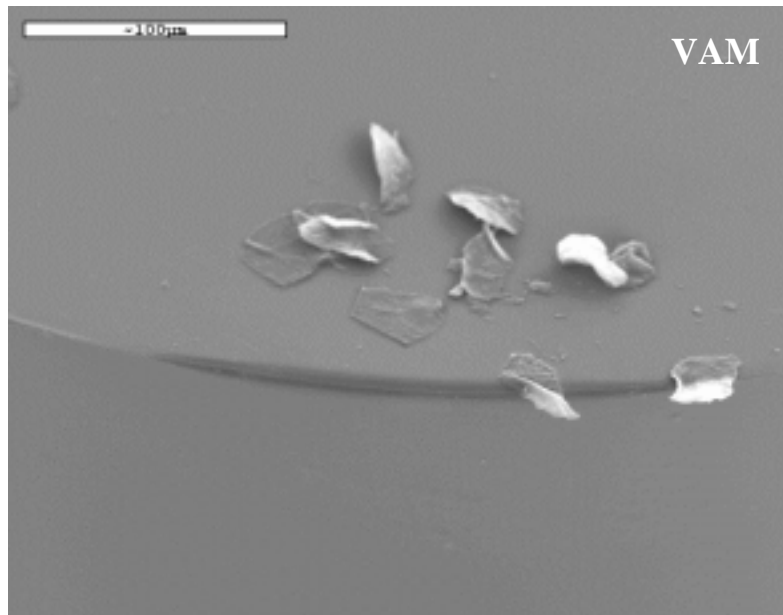
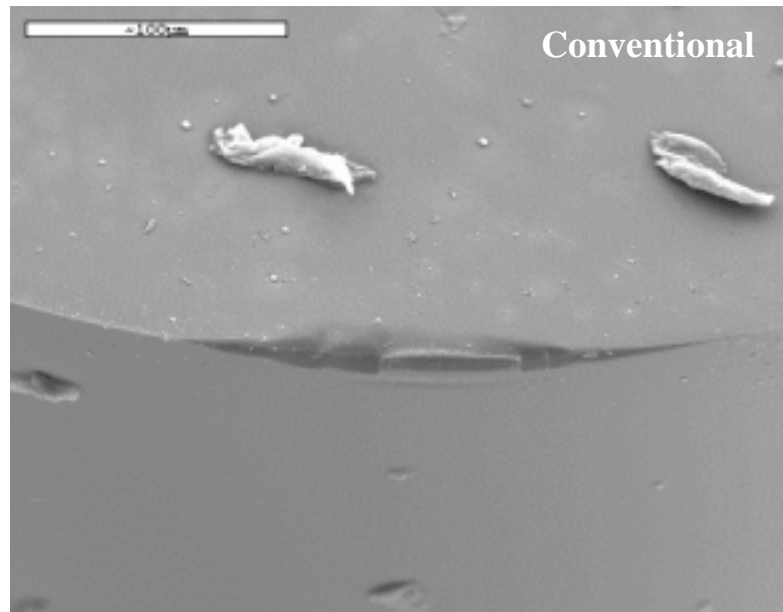


Figure 4.26: SEM Images of Post Trial 0.5 mm Radius Diamond Tools

The scour marks made by the steel surface on the radius of the diamond tool used in the conventional trial can easily be seen. Where as the VAM tool shows no noticeable marks, only even wear. Reorienting the diamond tip to the SEM, Figure 4.24, and doubling the magnification provides a more detailed view of the wear geometry.

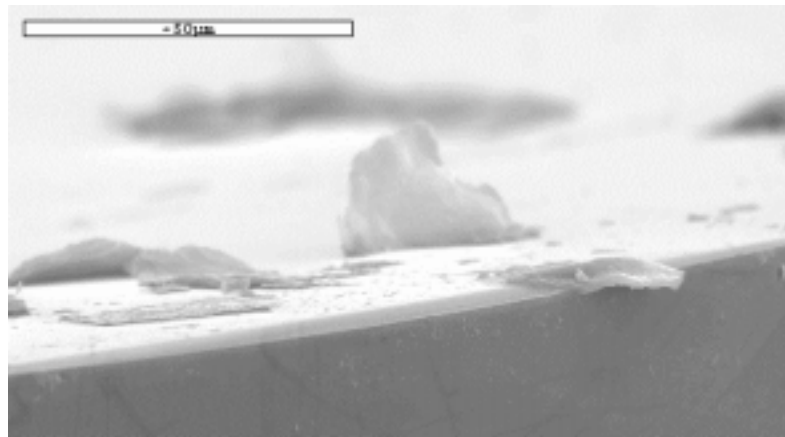
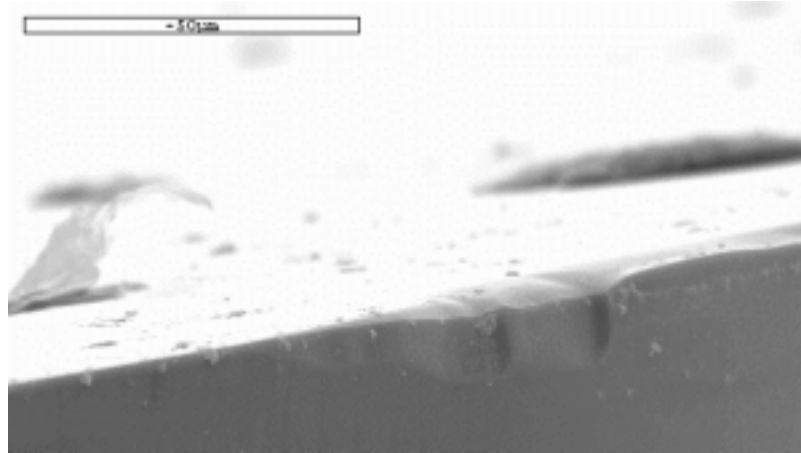


Figure 4.27: SEM Images of Post Trial 0.5 mm Radius Diamond Tools

The wear patterns off the two diamonds are very distinct. The conventional tool shows triangle shaped grooves worn into the diamond edge radius while the VAM tool exhibits a smooth continuous angled wear patch.

4.3.4 Discussion of Diamond Turning of Steel

Studies from the University of Bremen and Fraunhofer IPT, Aachen have reported cutting distances of 1500+ meters before surface degradation become significant with an ultrasonic servo [4,5]. While the PEC cutting trials were on a much smaller scale, they infer similar benefits at lower cutting speeds. It also supports the theory that diamond wear is a result of mechanical rather than chemical abrasion. Though further testing needs to be done.

Seen in the PEC trial but not previously reported is the pattern of tool wear for a VAM servo. A possible explanation is that since tool contact is only made with the rake face of the tool, due to the elliptical path, that only it abrades. And that abrasion of the rake face acts to sharpen the tool in process and remove tool defects that would result in a poor surface finish. In addition to the SEM images of the tool, the consistency of the surface finish, Tables 4.5 and 4.6, lends credence to theory of positive VAM tool wear. Figure 4.28 illustrates the sharpening effect of elliptical vibration machining.

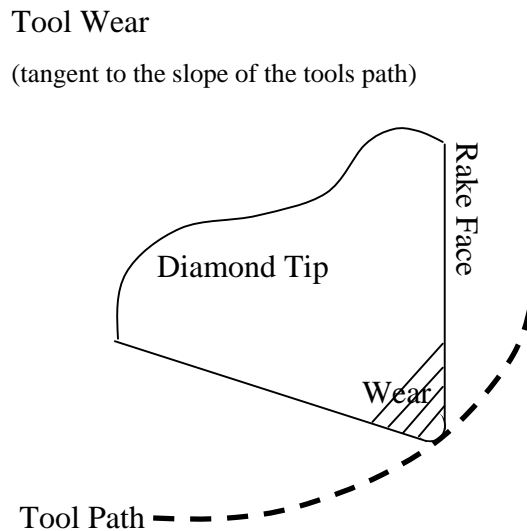


Figure 4.28: Theorized 2D VAM Tool Wear in Steel

CHAPTER FIVE: HIGH SPEED ULTRAMILL PROTOTYPE

5.0 DESIGN GOALS

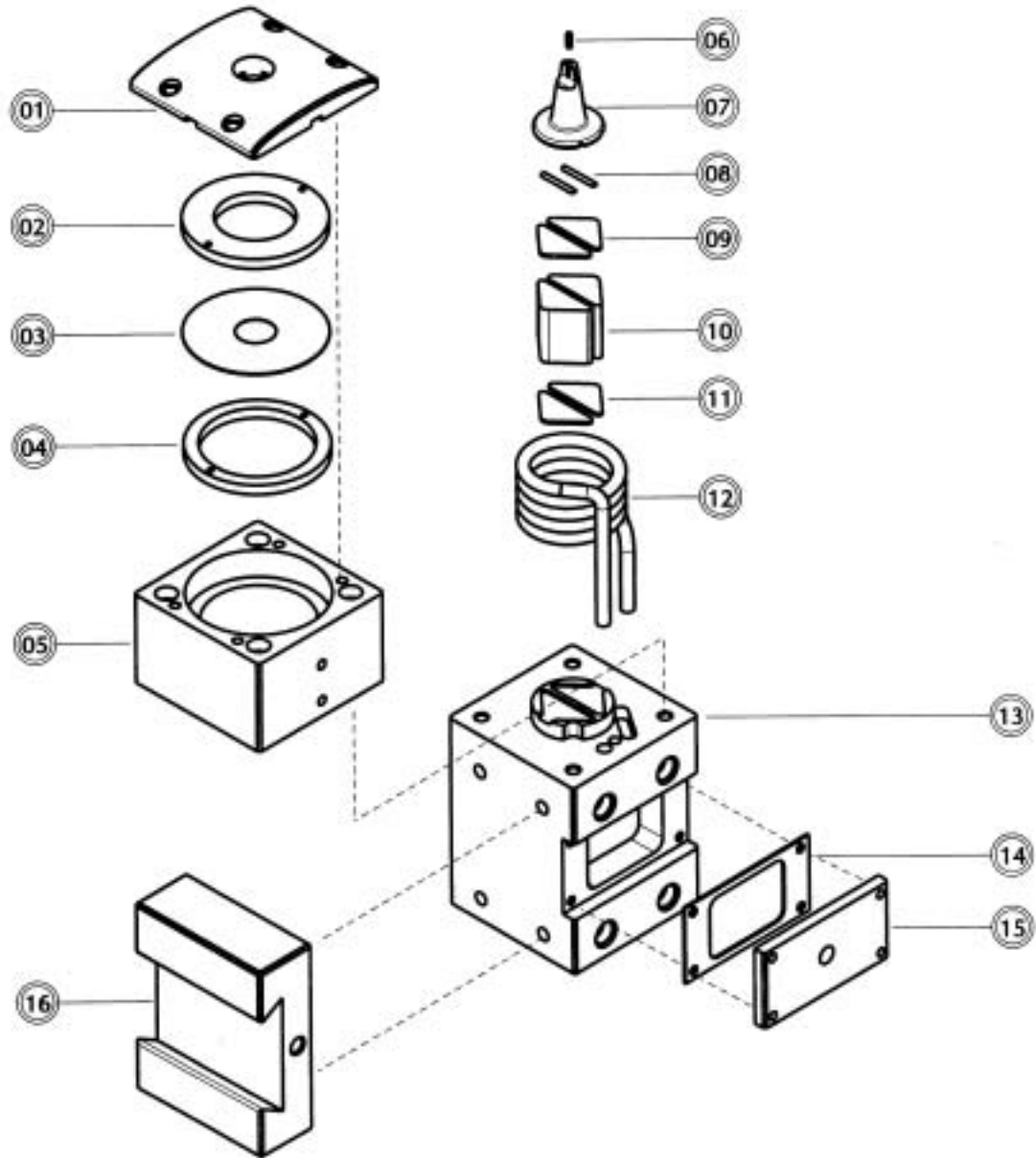
The low speed variant of the UltraMill was designed with the goals of studying the linkage dynamics, tool force and tool wear. As a result, it has several limiting factors that keep it from being used outside the laboratory setting. The first shortcoming is the low operating frequency. Operating at a 22% EDC with a 6 μ m depth of cut, the feed rate of the UMLS is limited to 72 mm/min when driven at its maximum frequency of 400 Hz. The low natural frequency, 525 Hz, is a result of the low stiffness to weight ratio of the servo. The low stiffness of the system also contributes to form error when machining hard materials or taking large depths of cuts.

On the mechanical side, the cyclical stresses induced in the preload wire cause tension to be reduced by a third to a half after 40 hrs of continuous machining. After logging approximately 50 hrs of cutting time, the preload wire reached a point of failure. The stress concentration points are the 90° bends where the wire enters and exits the head. The remainder of the preload mechanism is disadvantageous due to its large size.

With these factors in mind, the task of designing a high-speed tool servo was undertaken. The two main design goals were to increase the operational bandwidth by an order of magnitude and to produce a system that was rugged enough to be used in production.

5.1 DESIGN OF THE HIGH SPEED SERVO

The high-speed version of the UltraMill (UMLS) is a compact design, measuring less than 14 cm in overall length from diamond tip to mounting base. The servo's depth and width were limited to 6 cm to be compatible with a standard Aluris tool post. The servo, excluding support equipment (amplifiers, liquid chiller, etc.) and fittings, is made up of only 16 parts. Figure 5.1 is an exploded schematic of the UMHS. When completely assembled, the inner workings of the UMHS (actuators, cooling coil, etc.) are completely shielded from cooling liquid, part shavings and other manufacturing debris in a rugged steel housing. Figure 5.2 shows the UMHS in its assembled state.



Part List			
No.	Description	No.	Description
01	Protective Cap	09	Ceramic End Caps (top)
02	Diaphragm Backing Nut	10	Piezoelectric Actuators
03	Diaphragm (Preload Spring)	11	Ceramic End Caps (bottom)
04	Preload Adjustment Nut	12	Cooling Coils
05	Stack Housing	13	Base
06	Diamond Tool	14	Gasket
07	Cutter Head	15	Power / Cooling Compartment Cover
08	Pivot Half-Rounds	16	Aluris Attachment

Figure 5.1: Exploded Drawing of UMHS

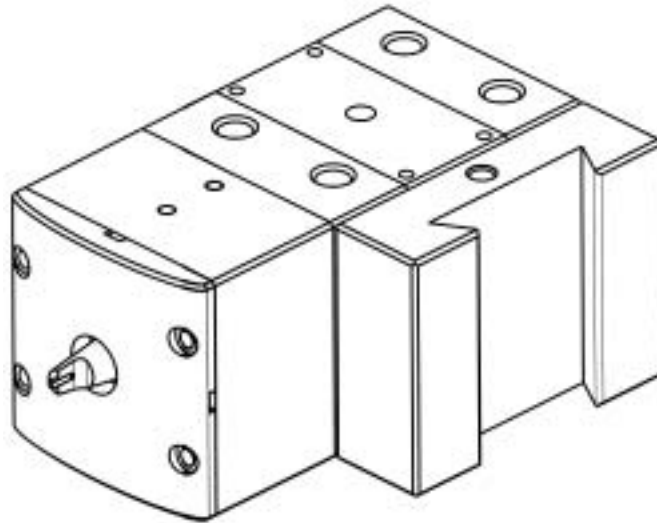


Figure 5.2: Assembly Drawing of UMHS with Aluris Attachment

5.1.1 Actuator

The high-speed version employs the same “T” shaped linkage as its predecessor. The arm lengths, a and b , have been increased from 3.150 mm to 5 mm to accommodate larger diameter stacks. The increased separation also allows the force transmission path to be closer to the centerline of each actuator. To maintain a good major to minor axis ratio, the trunk of the “T”, distance c , has been increased from 23 mm to 26 mm. The end result is an x-axis displacement of 103 μm and a y-axis displacement of 20 μm or a ratio of 5.15. The linkage arrangement, Figure 2.12, is reprinted below.

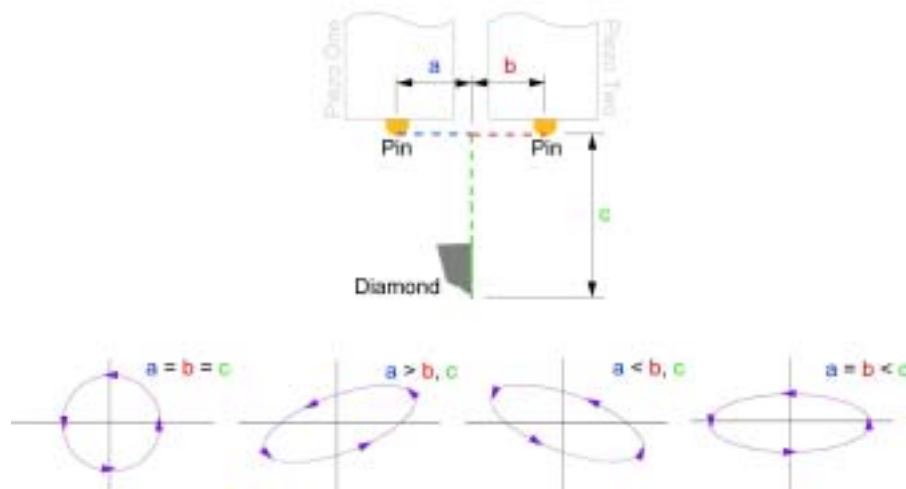


Figure 2.12: UltraMill “T” Linkage

The shape and size of the piezoelectric actuators were radically modified in an attempt to increase the stiffness while keeping the additional mass to a minimum. Finite element analysis (FEA) was employed to determine the optimal shape. Compared to the UMLS, the cross-sectional area was increased by a factor of 10 to 185.5 mm² and the length of the stack was reduced by 5.5% to 22 mm. Aside from the change in size, the most noticeable change is the shape of the actuator. FEA of several cross-sections showed that a triangle shaped actuator had the advantage of placing the centerlines of two facing actuators close together, thus allowing arms a and b to remain relatively short. This arrangement increased the natural frequency of the stack by 1 kHz compared to the closest design candidate, a semi-circle. Figure 5.3 illustrates the shape and basic dimensions of the new actuators. Detailed actuator specifications are tabulated at the end of this section and in Appendix B.

The actuators transmit force to the cutter head by 2 mm diameter half-round pivot pins similar to the previous design. The material of the pins has changed to alumina ceramic (Coorstek AD99.5) to increase the stiffness and decrease weight. The length of the pins has been increased to 15 mm for greater stability and for better force distribution.

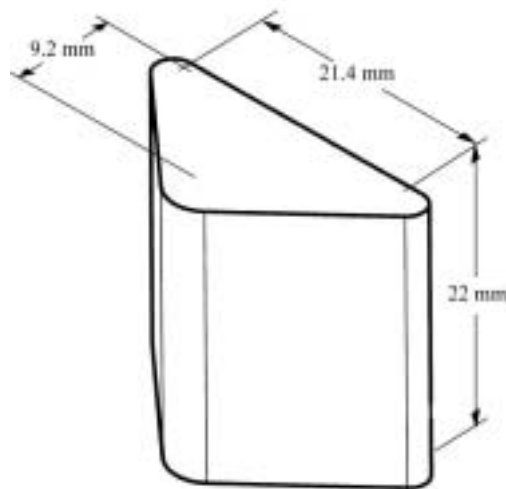


Figure 5.3: PZT Actuator of UMHS

5.1.2 Cutter Head

To increase the natural frequency, the system required a bigger PZT actuator and a lighter, symmetrical cutter head. Analysis of the low-speed prototype showed that a significant improvement in natural frequency could be realized if the cutter head's center of rotation were closer to the PZT actuators and inline with the centerline of the linkage. Figure 5.4 shows the cross-section of the new cutter head. In section A-A, the centroid is located at $y = 6.811$ mm, $x = 0.0$ mm and $z = 0.105$ mm.

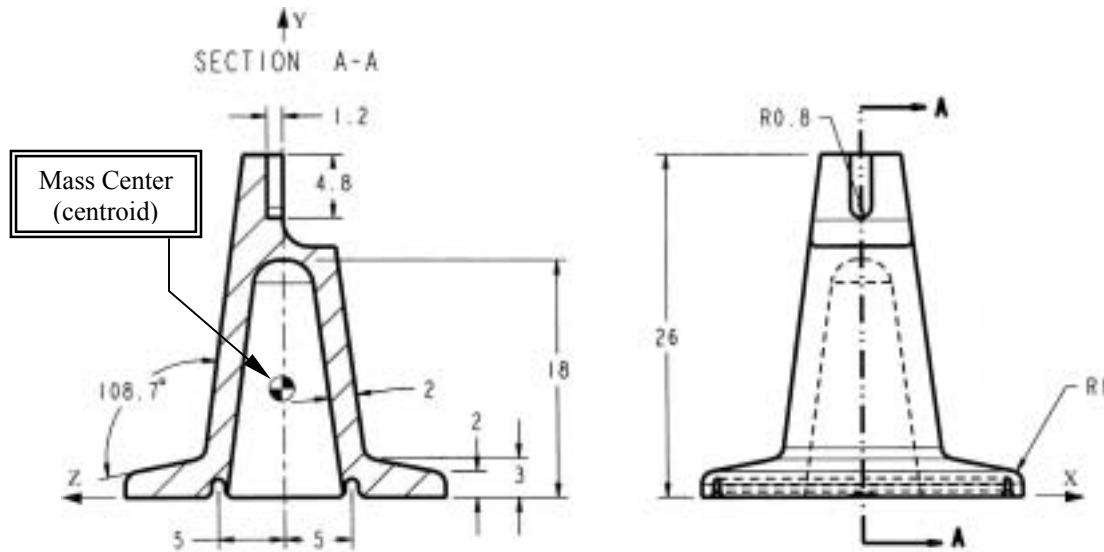


Figure 5.4: Cross-Section of UMHS Cutter Head

Selecting the optimum material for the cutter head is key to the design. A material that possessed a high elastic modulus, a low density and high resistance to surface abrasion was needed. Three potential candidates emerged: Aluminum, Alumina Ceramic and Nitride Bonded Silicon Carbide (NBSC).

Aluminum was considered as a candidate given its lightweight and low expense. However aluminum has a fairly low modulus of elasticity and low resistance to abrasion. These are important because a cutter head fabricated from a high modulus material will deflect less. The head needs to resist abrasion given the selected preload mechanism. As seen in Figure 5.5, a titanium diaphragm (Section 5.1.3) provides a preload directly to the

cutter head. At high cutting speeds, the contact between the diaphragm and an aluminum cutter head could result in severe wear, loss of preload and destruction of the servo.

Given these material limitations, steps could be taken to make aluminum viable. Hard-coat anodizing the material would increase abrasion resistance. Finite element analysis showed that a cutter head of the geometry shown in Figure 5.4 would deflect $0.7\ \mu\text{m}$ under 5 N of cutting force. Given the major axis stroke of the UMHS, $103\ \mu\text{m}$, this is an acceptable amount of deflection. The calculated first and second natural frequencies of an aluminum cutter head are 16.75 kHz and 20.24 kHz respectively.

The two ceramic materials, alumina and NBSC, both possess high elastic modulus and high abrasion resistance. However with a density of 2.6 g/cc, NBSC is half as dense as alumina, 4.9 g/cc. Finite element analysis of a NBSC cutter head placed the first natural frequency at 27.47 kHz and the second at 28.45 kHz. The maximum head deflection was predicted to be $0.5\ \mu\text{m}$ under 5 N of cutting force. Lighter than alumina and producing less deflection than aluminum, NBSC was deemed the preferred material.

5.1.3 Preload Spring

A titanium diaphragm will be used to preload the cutter head onto the PZT actuators. A diaphragm was chosen because it was a single component that could both preload servo and seal the assembly compartment. Titanium was ideally suited for this application because of its high yield stress, good strength to weight ratio and resistance to abrasion. A thin cross-section titanium diaphragm will be able to withstand prolonged periods of cyclical stress.

Illustrated in Figure 5.5, the preload assembly consists of four parts: The threaded housing (05), The preload adjustment nut (04), The diaphragm (03) and The diaphragm backing nut (02).

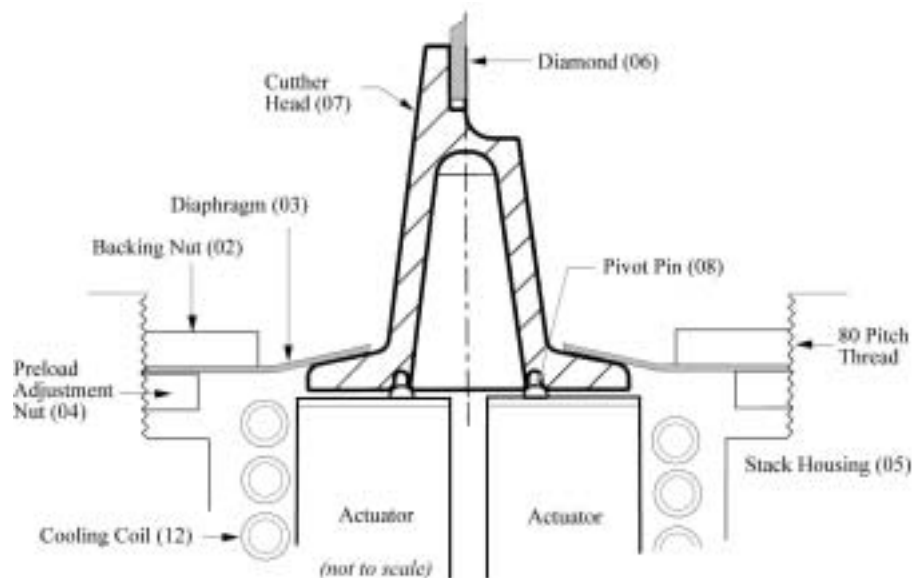


Figure 5.5: Illustration of UMHS Assembly

Imparting an initial deflection to the diaphragm controls the amount of force applied to the assembly. Approximately 400 N of preload force is needed to compensate for the acceleration of the linkage mass while being driven at 5 kHz. This can be accomplished with a 1mm deflection of the diaphragm. It should be noted that the preload force never decreases during servo operation since it is assembled while the stacks are de-energized. During operation, the preload force fluctuates by 8 N resulting from the 20 μ m of vertical deflection of the cutter head.

Setting the preload is a simple task. The diaphragm is first set on top of the assembly and the point of contact between the inner edge of the diaphragm and the cutter is marked. The diaphragm is then removed and the preload adjustment nut, Item 04 in Figure 5.5, is screwed until the upper surface of the nut is 1 mm below the marked contact point. The diaphragm is now placed back over the assembly. Finally, using a specially designed spanner wrench, the backing nut, Item 02, is screwed down until firm contact is made between itself, the diaphragm and the adjustment nut. The backing nut serves as not only a jam nut to keep the diaphragm in place, but also as a stop that limits the amount the diaphragm can deflect.

5.1.4 Diamond Tool

In cooperation with Chardon Tool, a diamond tool insert was designed for use in the UMHS. 5.6 mm in length by 1.2 mm deep and 1.5 mm wide, the 1 mm nose radius tool is cut from a single crystal diamond. To minimize weight, the diamond tool is not mounted on a substrate. Instead it is bonded into a groove in the cutter head, shown in Figures 5.4 and 5.5, with 3M structural adhesive. The structural adhesive will hold the tool firmly in place, and with the application of a high heat source, allow the tool to be removed for lapping.

5.1.5 Support Equipment

Heat generation is always a concern with precision equipment. The servo needs to be maintained at a constant temperature, preferably room temperature, so that thermal expansion does not alter tools position over time. The average power, P_{avg} , consumed by each PZT stack can be calculated by,

$$P_{avg} = \frac{CV^2f}{2} \quad (65)$$

where C is the capacitance of the stack in farads, V is the peak-to-peak (P-P) applied voltage and f is the drive frequency in Hz. The capacitance of the selected stack actuator is 0.25 μ farads. The UMHS will be driven with an 800 V P-P sinusoidal signal at up to 5000 Hz. Therefore the power required by each stack is 400 Watts. The manufacture estimates that the hysteresis of the PZT stacks to be approximately 20%. In order to keep the stack assemblies at approximately room temperature, 150 Watts of heat will have to be removed.

The heat generated by the stacks will be removed through the use of a thermoelectric air to liquid chiller capable of removing up to 400 Watts. The chiller will circulate ethylene glycol (EG) enriched water through a copper coil that surrounds the actuators. This coil is Item 12 in Figure 5.1. A thermocouple mounted in the stack housing, Item 5, provides feedback to the PID controller of the chiller. The temperature of the EG, flowing at 3

liters per min, is regulated by the controller to maintain a user defined set point within 0.2°C. The cooling path from the coil to the PZT actuators is completed by filling the stack housing with a Diamethylsiloxane Polymer fluid (Dow Corning 561 Transformer Fluid). Designed for use in high-voltage transformers, this is an ideal fluid to use in the UMHS. It provides both high thermal conductivity to carry excess heat away from critical components and a high dielectric for an extra measure of protection against arcing of the stack electrodes.

The two PZT actuators are controlled via two independent sinusoidal 0-800 volt signals at 5 kHz. Two 90° out of phase signals are produced with an HP 8904A Function Generator. The signals are then independently routed through two 500 W magnetically coupled linear amplifiers where they are first offset by 4 volts and then amplified 100 times. The end result is two 90° separated, 0-800 volt, 5000 Hz signals.

5.1.6 System Specifications

The specifications of the servo and that of its support equipment are compiled in Table 5.1 through Table 5.9. Detailed drawing of the UMHS can be found in Appendix B.

Table 5.1: UMHS Tool Path

Elliptical Path								
Δx	102.92	μm						
Δy	19.78	μm						
"T" Components								
a	5	mm	b	5	mm	c	26	mm

Table 5.2: UMHS Cutter Head

Cutter Head								
Material	Nitride Bonded Silicon Carbide (NBSC)							
density	2.6	g/cc	E	152	GPa	v	0.2	--
mass	4.811	gm						
Center of Gravity								
x	0.0	mm	y	6.811	mm	z	0.105	mm
Inertia About Axis								
Ixx	558.9	g *mm ²	Iyy	214.1	g *mm ²	Izz	554.2	g *mm ²
Natural Frequency								
First	27.47	Hz	Second	28.45	Hz			
Deflection @ 5N	0.5	µm						

Table 5.3: UMHS Natural Frequency

Natural Frequency			
Total System	4503	Hz	Modal Analysis
Head	27470	Hz	FEA
Stacks	10744	Hz	FEA
Diaphragm	9885	Hz	FEA

Table 5.4: Piezoelectric Material

Piezoelectric Actuators					
Formula	PZTW100 ~ Similar to PZT-5A				
Strain	1300	µ strain			
Stack Specific Information					
Capacitance	0.25	µf	Power Requirement @ 812 V and 5 kHz	500	watts

Table 5.5: Miscellaneous Parameters

Miscellaneous Notes					
Speed of Sound in Cooling Fluid	1.2	Km/s	Wavelength	0.24	m
Maximum Diaphragm Velocity @ 5 kHz	0.44	m/s			
Required Preload	90	lbf			

Table 5.6: UMHS Cooling

Cooling Fluid Specifications					
Brand	Dow Corning 561 Transformer Fluid (Diamethylsiloxane Polymer)				
Appearance	Clear	--	Kinetic Viscosity @ 100 C	0.15	stokes
Specific Gravity	0.98	--	Dynamic Viscosity @ 100 C	14.4	cP
Flash Point	572	F	Specific Heat	2094	J/Kg K
Thermal Diffusivity	0.003	Ft ² /hr	Thermal Conductivity	0.155	W/m K

Table 5.7: UMHS Amplifiers

Amplifier		
Model	500 W Magnetic Coupled Linear Amplifier	Hz @ 812 VAC
Manufacturer	Kinetic Ceramic	
Bandwidth	500-5000	
Quantity Required	2	
Additional Notes	Built in Variable DC Offset	

Table 5.8: UMHS Chillers

Chiller			
Model	"Thermocube-400" Thermoelectric Air to Liquid Chiller		
Manufacturer	Solid State Cooling System		
Specifications			
Operational Range	-10° to 50° C	Size	12.75" x 11.25" x 12.0"
Cool Capacity	400 W @ 25° C amb. air	Weight	33 lbs
Coolant	water / EG mixture	Pump	3 liters / min
Noise	< 50 dB at 3 feet		
Controller	Digital PID control with < 0.2° C accuracy		
Additional Notes	Reservoir with level sensor		
	Alarm for over heating		

Table 5.9: UMHS Function Generator

Function Generator		
Model	8904A	
Manufacturer	HP (Agilent Technologies)	
Range	DC to 600	kHz
Channels	2	

CHAPTER SIX: CONCLUSION

6.0 QUESTIONS ANSWERED

Chapter 1 concluded with a series of 6 questions that previous research in the areas of vibration assisted machining and elliptical vibration machining had not addressed. With the work presented in this thesis, they can now be answered.

“Why are the forces reduced?”

Forces are reduced in elliptical vibration machining due to a reduction in per cycle chip thickness. For a given unit of time, both elliptical and standard machining remove the same amount of material. However, during this unit of time, elliptical vibration machining divides the volume into several smaller volumes. The number of smaller volumes depends on the operational frequency of the tool servo. The size of the smaller volume is a product of the horizontal speed ratio (HSR), the overall depth of cut, the tool geometry and the elliptical tool path. Therefore the time average force required in VAM is only that necessary to remove the smaller volume, referred to as the per cycle chip thickness.

“How does tool motion relate to surface finish?”

The surface finish of a 2D vibration machined workpiece is a function of the elliptical shape (major and minor axis), the depth of cut, the up-feed, the cross-feed and the ratio between the two feed directions (phase). The 3D surface roughness is can be found from Equations (16) and (17) which define the peak-to-valley (R_t) surface roughness in the xy- and zy-planes respectively.

“What surface finish is possible with VAM?”

Vibration assisted machining is capable of producing any surface feature that can be created from a summation of elliptical volumes. The spacing of the elliptical volumes defined by the up-feed and cross-feed results in surface finishes ranging from non-overlapping half ellipsoids to pyramids to the best surface finish obtainable by standard machining methods.

“What cutting speed will produce a benefit?”

The cutting speed or rate at which the tool engages new workpiece material is dependent on the desired surface finish and/or the desired machining force. Both of which are adjusted with the selection of the HSR. The HSR relates the cutting speed to the shape of the tool path and the frequency of oscillation of the tool. Given a desired surface finish or machining force, the cutting speed can be increased by increasing x-axis displacement of tool and/or the frequency of oscillation. Cutting speed is directly proportional to the shape of the ellipse and the operational frequency of the servo.

“Why is diamond tool life increased?”

Research showed that elliptical vibration machining produced wear similar in magnitude to that of conventional machining. However, due to the elliptical path of the tool, wear is only exhibited on the rake face of the tool. This type of wear is not detrimental to the surface finish since it is the trailing edge that last makes contact with the workpiece that determines the finish condition. Wear experiments on the machining of steel suggest that flank face wear is beneficial, continually sharpening tool to leave a fresh trailing edge. This is most likely the cause for extended to life in 2D VAM.

“What is the best servo design for a given application?”

The maximum operational frequency and the shape of the ellipse determine the performance of a servo. The time required to manufacture a part with of a given surface finish decreases as the operational frequency of the servo increases. However obtaining a high operational speed with current technology comes at the expense of path shape and control. The optimum servo design depends on the application.

6.1 SUMMARY

The model developed in this thesis has provided both a physical and a mathematical explanation for the results of the past 20 years of research in vibration assisted machining. It forms the basis of future research into tool wear and the machining of

brittle materials. Lastly, it provides the engineering information necessary to take the benefits of VAM from the laboratory floor to the production floor.

REFERENCES

1. Larson, C., Strenkowski, J.; “Diamond Tool Wear”, Precision Engineering Center Annual Report, North Carolina State University, Raleigh NC, Vol. 10, pp. 123-135, 1992.
2. Storz, G., Dow, T.; “Geometric Modeling of a Contour Grinding Operation”, Precision Engineering Center Annual Report, North Carolina State University, Raleigh NC, Vol. 10, pp. 49-61, 1992.
3. Jung-Hwan, A., Han-Seok, L., Seong-Min, S.; “Improvement of Micro-machining Accuracy by 2-Dimensional Vibration Cutting”, American Society of Precision Engineers Conference Proceedings, Vol. 20, pp. 150-153, 1999.
4. Brinksmeier, E., Glabe, R.; “Elliptical Cutting of Steel with Diamond Tools”, American Society of Precision Engineers Conference Proceedings, Vol. 20, pp. 163-166, 1999.
5. Klocke, F., Rubenach, O.; “Ultrasonic Assisted Diamond Turning of Steel and Glass”, American Society of Precision Engineers Conference Proceedings, Vol. 19, pp. 179-190, 1998.
6. Moriwaki, T., Shamoto, E.; “Ultra-precision Diamond Cutting of Hardened Steel by Applying Elliptical Vibration Cutting”, Annals of the CIRP, Vol. 48, pp. 441-444, 1999.
7. Shamoto, E., Moriwaki, T.; “Study on Elliptical Vibration Cutting”, Annals of the CIRP, Vol. 43, pp. 35-38, 1994.
8. Moriwaki, T., Shamoto, E.; “Ultra-precision Diamond Turning of Stainless Steel by Applying Ultrasonic Vibration”, Annals of the CIRP, Vol. 40, pp. 559-562, 1991.
9. Kazuo, N., Minoru, A., Torahiko, K.; “Machining Characteristics of Hard Materials”, Annals of the CIRP, Vol. 37, pp. 89-92, 1988
10. Dautzenberg, J., Hijink, J., Van der Wolf, A.; “The Minimum Energy Principle Applied to the Cutting Process of Various Workpiece Materials and Tool Rake Angles”, Annals of the CIRP, Vol. 31, pp. 91-96, 1982.

11. Ikawa, N., Donadson, R., Komanduri, R., Konig, W., McKeown, P., Moriwaki, T., Stowers, I.; "Ultraprecision Metal Cutting – The Past, the Present and the Future", *Annals of the CIRP*, Vol. 40, part 2, pp. 587-597, 1991
12. Moriwaki, T., Horiuchi, A., Okuda, K.; "Effect of Cutting Heat on Machining Accuracy in Ultra-Precision Diamond Turning", *Annals of the CIRP*, Vol. 39, pp. 81-84, 1990.
13. Chandrasekaran, H., Reddy, T.; "On the Nature of Cyclic Stress in the Tool Tip in Peripheral Milling and Their Implications on Tool Fracture", *Annals of the CIRP*, Vol. 31, pp. 85-89, 1982.
14. Casstevens, J.; "Diamond Turning of Steel in Carbon-Saturated Atmospheres", *Precision Engineering*, Vol. 5, pp. 9-15, 1983.
15. Masuda, M.; "Ultra-precision Cutting of Steel with CBN Tools" (In Japanese), *JSPE*, Vol. 52, pp. 384-389, 1986.
16. Moriwaki, T.; "Machinability of CBN Tools in Precision Engineering of Stainless Steel", *Proceedings of the 5th International Conference on Manufacturing Engineering*, Wollongong, pp. 129-133, 1990.
17. Evans, C.; "Cryogenic Diamond Turning of Stainless Steel", *Annals of the CIRP*, Vol. 40, pp. 571-575, 1991.
18. Arcona, C.; "Tool Force, Chip Formation and Surface Finish in Diamond Turning", PhD Thesis, North Carolina State University, 1996.
19. Standard Test Method for Microhardness of Materials, ASTM Committee E-4, Publication E384-84, July 1984
20. Material Properties of Metals, Ferrous and Non-Ferrous Search, Internet Site: www.matweb.com, March 2001.
21. Evans, C., Paul, E., Mangamelli, A., Mc Glaufin, M.; "Chemical Aspects of Tool Wear in Single Point Diamond Turning", *Precision Engineering*, Vol. 18, pp. 4-19, 1996.
22. Dresher, J.; "Tool Force Measurement in Diamond Turning", Masters Thesis, North Carolina State University, 1989
23. Dresher, J.; "Tool Force, Tool Edge and Surface Finish Relationships in Diamond Turning", PhD Thesis, North Carolina State University, 1991

APPENDIX A: MATHCAD WORKSHEETS

1D Duty Cycle Calculation

units:

$$\mu\text{m} := 1 \cdot 10^{-6} \text{ m}$$

General Time Parameter, t:

$$i := 0, 1..1000$$

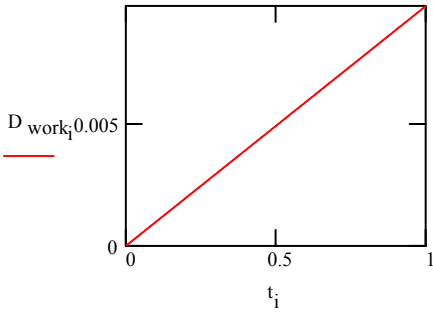
$$t_i := i \cdot 0.001 \text{ sec}$$

Workpiece Parameters:

Workpiece velocity, V: $V := 10 \frac{\text{mm}}{\text{sec}}$

Displacement, D.work: $D_{\text{work}_i} := V \cdot t_i$

Velocity, V.w: $V_{w_i} := \frac{D_{\text{work}_i}}{t_i}$



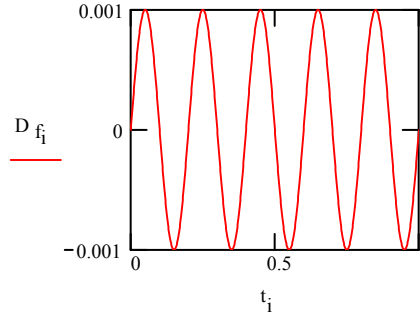
Vibration Parameters:

Amplitude, A: $A := 1 \text{ mm}$

Frequency, ω : $\omega := 5 \cdot 2 \pi \cdot \text{Hz}$

Velocity, V.f: $V_{f_i} := A \cdot \omega \cdot \cos(\omega \cdot t_i)$

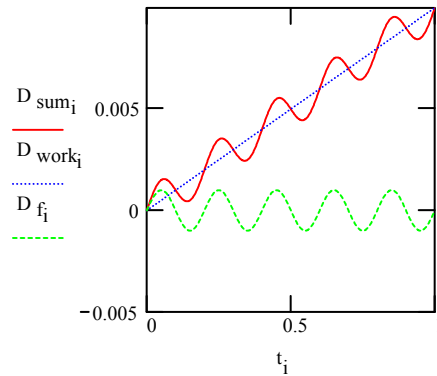
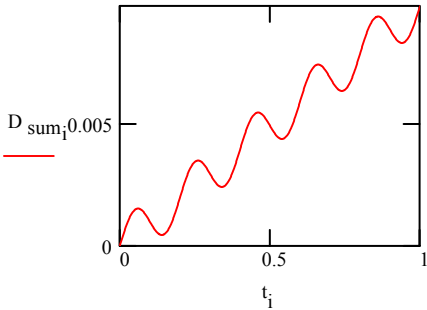
Displacement, D.f: $D_{f_i} := A \cdot \sin(\omega \cdot t_i)$



Summation of Displacements/Velocities:

$$D_{\text{sum}_i} := D_{\text{work}_i} + D_{f_i}$$

$$V_{\text{sum}_i} := V_{w_i} + V_{f_i}$$



Solve for t.1 which is at the first peak, or at V.sum = zero.

```
T1E(Vector) :=
  j ← 0
  while Vectorj > 0
    j ← j + 1
  j
```

$i_t := T1E(V_{sum})$

$i_t = 61$ Which is the iteration of t where V.sum equals zero:

the time corresponding to this iteration is, t.1:

$$t_1 := 0.001 \cdot i_t \quad t_1 = 0.061$$

Once t.1 is found substitute back into D.sum to find D.1 at t.1.

$$D_1 := D_{sum}(i_t) \quad D_1 = 1.551 \text{ mm}$$

Use D.1 to solve for t.2, which is the location of the next contact.

```
T2E(Vector, Displ, first) :=
  j ← first + 1
  while Vectorj - Displ < 0
    j ← j + 1
  j
```

$j_t := T2E(D_{sum}, D_1, i_t)$

$j_t = 189$ Which is the iteration of t where the tool engages the work surface again:

the time corresponding to this iteration is, t.2:

$$t_2 := 0.001 \cdot j_t \quad t_2 = 0.189$$

$$t_{period} := \frac{1 \cdot (2 \cdot \pi) \cdot \text{Hz}}{\omega}$$

$$t_{period} = 0.2$$

Knowing t.1 and t.2 provides the Duty Cycle information:

Duty Cycle, DC:

$$DC := \frac{t_{period} - (t_2 - t_1)}{t_{period}}$$

$$DC = 0.36$$

Based on the concepts above, an example program (below) was written which provides a chart of Duty Cycle versus Velocity Ratio:

```

DutyCycle := j ← 0
              i ← 0
              t ← 0
              A ← 1
              for Vwork ∈ 0.1, 0.2.. 31.4
                ω ← 5 · 2 · π
                Vsum ← (Vwork) + A · ω · cos(ω · t)
                while Vsum > 0
                  i ← i + 1
                  t ← .001 · i
                  Dwork ← Vwork · t
                  Vw ←  $\frac{D_{work}}{t}$ 
                  Vf ← A · ω · cos(ω · t)
                  Df ← A · sin(ω · t)
                  Vsum ← (Vw) + Vf
                  Dsum ← Dwork + Df
                T1 ← t
                D1 ← Vw · T1 + A · sin(ω · T1)
                k ← 1
                k ← T1 + .001 · k
                while [(Vw · k + A · sin(ω · k)) - D1] < 0
                  k ← k + .001
                T2 ← k
                TC ←  $\left[ \left[ \frac{2 \cdot \pi}{\omega} - (T2 - T1) \right] \right]$ 
                DCj ←  $\left[ \frac{TC}{(2 \cdot \pi)} \right]$ 
                Vrj ←  $\frac{\left( \frac{D_{work}}{t} \right)}{A \cdot \omega}$ 
                Vector0,j ← DCj
                Vector1,j ← T1
                Vector2,j ← T2
                Vector3,j ← Vrj
                j ← j + 1

```

Vector

Parameters Used:

Amplitude, A = 1 mm

Frequency, ω = 5 Hz

Workpiece Velocity, or V_{work} was incremented from 0.1 to 31.4 mm/sec (increments of 0.1) to provide the Velocity Ratio. The selection of velocity range allows for the Velocity Ratio to be charted from nearly zero to nearly 1. Exceeding 31.4 mm/sec for an amplitude of 1 mm and a frequency of 5 Hz, creates a Velocity Ratio greater than one and a corresponding constant contact Duty Cycle.

Q := DutyCycle

	0	1	2	3	4	5
Q =	0.035	0.035	0.035	0.035	0.035	0.035
1	0.051	0.051	0.051	0.051	0.051	0.051
2	0.244	0.244	0.244	0.244	0.244	0.244
3	$3.183 \cdot 10^{-3}$	$3.183 \cdot 10^{-3}$	$3.183 \cdot 10^{-3}$	$3.183 \cdot 10^{-3}$	$3.183 \cdot 10^{-3}$	$3.183 \cdot 10^{-3}$

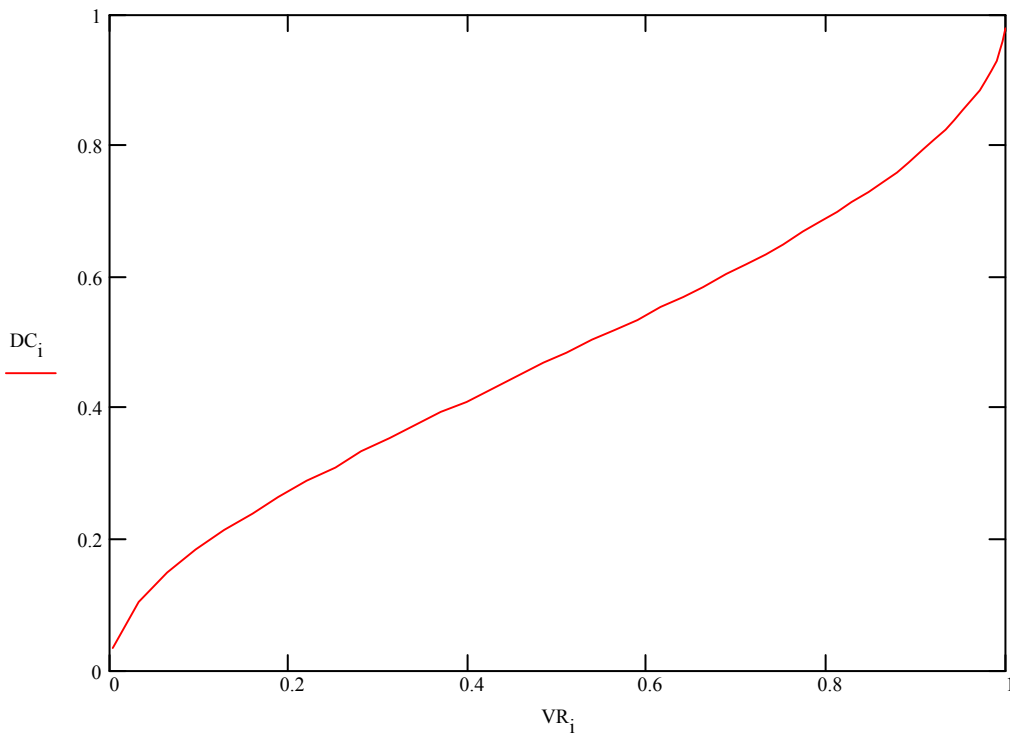
i := 1, 2.. 313

Velocity Ratio, VR:

$$VR_i := Q_{3,i}$$

Corresponding Duty Cycle, DC:

$$DC_i := Q_{0,i}$$



2D Duty Cycle Calculation

Part One: Comparison of UM Tool Path to Elliptical Path

$$l_1 := 3.150 \cdot \text{mm} \quad \text{Length to Pin}$$

$$f := 10 \cdot \text{Hz} \quad \text{UM Frequency}$$

$$\mu\text{m} := 10^{-6} \cdot \text{m} \quad \text{Unit Declaration}$$

$$l_2 := 3.150 \cdot \text{mm} \quad \text{Length to Pin}$$

$$\phi := 1.571 \quad \text{90 deg Phase Shift}$$

$$\text{Disp}_{\text{stack}} := 19 \cdot \mu\text{m} \quad \text{Stack Displacem}$$

$$l_3 := 22.962 \cdot \text{mm} \quad \text{Length to Diamond}$$

$$\omega := f \cdot 2 \cdot \pi \quad \text{Angular Frequency}$$

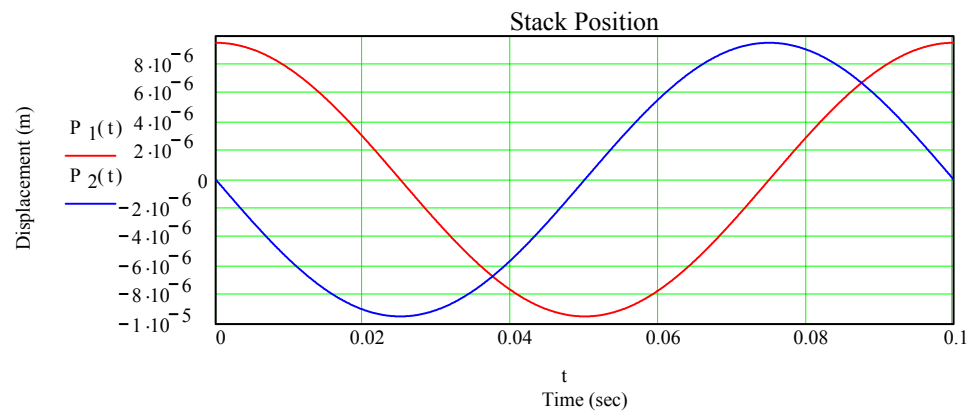
$$t := 0, 0.0001 \cdot \text{s}.. 0.1 \cdot \text{s} \quad \text{Time}$$

Piezo Stack End Location:

$$D := \frac{\text{Disp}_{\text{stack}}}{2}$$

$$P_1(t) := D \cdot \cos(\omega \cdot t)$$

$$P_2(t) := D \cdot \cos(\omega \cdot t + \phi)$$

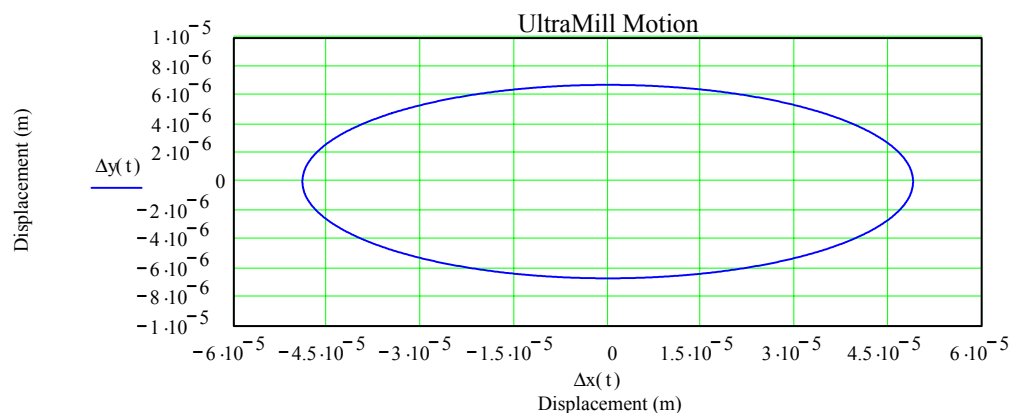


Stack Relationships:

$$\beta(t) := \frac{P_2(t) - P_1(t)}{l_1 + l_2}$$

$$\Delta x(t) := l_3 \cdot \beta(t)$$

$$\Delta y(t) := \frac{P_1(t) \cdot l_2 + P_2(t) \cdot l_1}{l_1 + l_2}$$

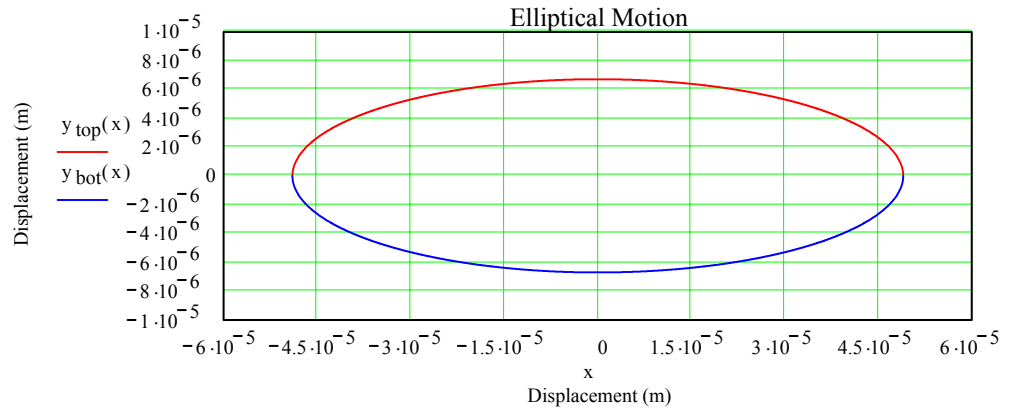


$$a := 48.97 \cdot \mu\text{m} \quad \text{Major Axis}$$

$$b := 6.71 \cdot \mu\text{m} \quad \text{Minor Axis}$$

$$x := -a, -a + \left(a \cdot \frac{1}{1000} \right) .. a \quad \text{Displacement}$$

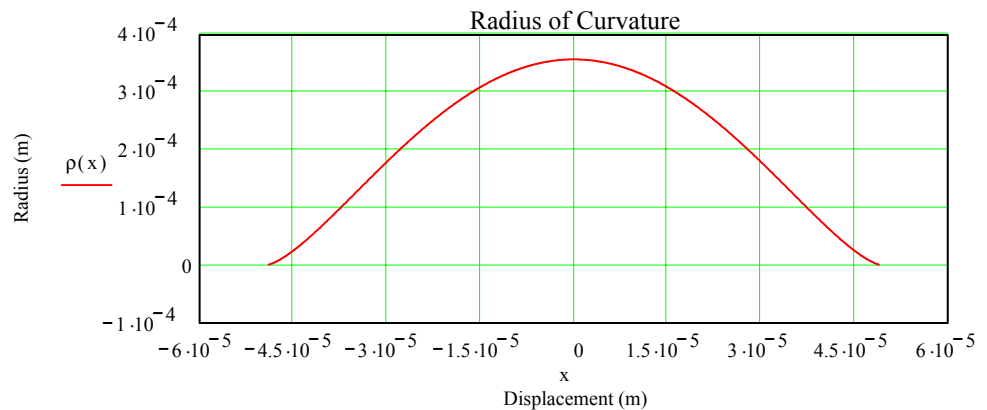
$$y_{\text{top}}(x) := \sqrt{\left[1 - \left(\frac{x^2}{a^2} \right) \right]} \cdot b^2 \quad y_{\text{bot}}(x) := -\sqrt{\left[1 - \left(\frac{x^2}{a^2} \right) \right]} \cdot b^2 \quad \text{Equation of Ellipse in Terms of X - Displacement}$$



Part Two: Radius of Curvature Calculation

$$y(x) := y_{\text{bot}}(x) \quad \text{Re-name Ellipse (only half needed)}$$

$$\rho(x) := \frac{\left[1 + \left(\frac{d}{dx} y(x) \right)^2 \right]^{\frac{3}{2}}}{\frac{d^2}{dx^2} y(x)} \quad \text{Radius of Curvature}$$



$$\rho := 357 \cdot \mu\text{m} \quad \text{Maximum Radius of Curvature (x = 0)}$$

Part Three: Contact Length as a Function of Depth

Cutting Input Parameters:

$$v := 0 \cdot \frac{\text{mm}}{\text{s}}, 0.001 \cdot \frac{\text{mm}}{\text{s}} .. 0.979 \cdot \frac{\text{mm}}{\text{s}} \quad \text{Workpiece Velocity} \quad d := 4 \cdot \mu\text{m} \quad \text{Depth of Cut}$$

Calculated Location Parameters:

$$V_{\text{crit}} := 2 \cdot \pi \cdot f \cdot a \quad \text{Maximum Tool Velocity}$$

$$\text{HSR}(v) := \frac{v}{V_{\text{crit}}} \quad \text{Horizontal Speed Ratio}$$

$$f_{\text{index}}(v) := 2 \cdot \pi \cdot a \cdot \text{HSR}(v) \quad \text{Distance Tool is Indexed per Cycle}$$

$$f_{i2}(v) := \frac{f_{\text{index}}(v)}{2} \quad \text{Half the Indexed Distance}$$

$$\theta_1(v) := \text{asin}\left(\frac{f_{i2}(v)}{a}\right) \quad \text{Trailing Angle (start of cut)}$$

$$\theta_2 := \text{acos}\left(1 - \frac{d}{b}\right) \quad \text{Leading Angle (end of cut)}$$

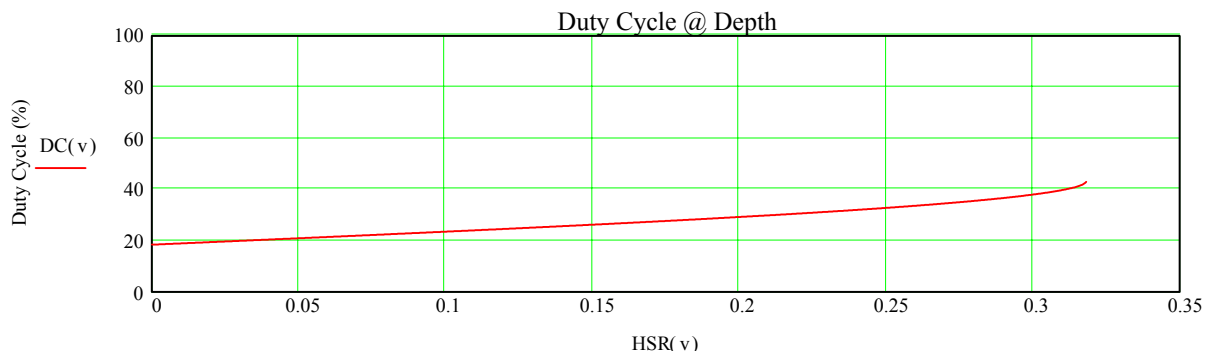
$$\text{Ang}_{\text{sum}}(v) := \theta_1(v) + \theta_2 \quad \text{Angle Summation}$$

$$L_{\text{curve}}(v) := \rho \cdot (\theta_1(v) + \theta_2) \quad \text{Length of Cut}$$

$$L_{\text{ellipse}} := 2 \cdot \pi \cdot \rho \quad \text{Perimeter of Ellipse (approx.)}$$

Part Four: Duty Cycle Calculation

$$\text{DC}(v) := \left(\frac{L_{\text{curve}}(v)}{L_{\text{ellipse}}}\right) \cdot 100 \quad \text{Duty Cycle}$$



UltraMill Tool Force Model

Parameters

Cutting Parameters

$f := 10 \cdot \text{Hz}$ ultramill cutting frequency

$d := 6.0 \cdot 10^{-6} \cdot \text{m}$ depth of cut

$r := 3 \cdot \text{mm}$ tool radius

$a := 95 \cdot 10^{-6} \cdot \text{m}$ major axis

$b := 14.6 \cdot 10^{-6} \cdot \text{m}$ minor axis

Tool Parameters

$\mu_f := 0.30$ flank face friction

$\mu := 0.27$ chip / tool face friction

Material Properties(Copper)

$H := 1.0 \cdot 10^9 \cdot \text{Pa}$ Vickers hardness

$E := 123 \cdot 10^9 \cdot \text{Pa}$ Modulus of Elasticity

$\phi_{\text{stat}} := 45 \cdot \text{deg}$ shear angle (material dependent)

Unit Declartaion

$\mu\text{m} := 10^{-6} \cdot \text{m}$

$\text{nm} := 10^{-9} \cdot \text{m}$

$\text{pm} := 10^{-12} \cdot \text{m}$

General Force Equation

$$F_c = \left(H \cdot \frac{A}{3} \right) \cdot \left(1 + \frac{\cot(\phi)}{\sqrt{3}} \right) + \mu_f \sigma_f A_f \quad \text{cutting force}$$

$$F_t = \mu \cdot \left(H \cdot \frac{A}{3} \right) \cdot \left(1 + \frac{\cot(\phi)}{\sqrt{3}} \right) + \sigma_f A_f \quad \text{thrust force}$$

$$\sigma_f = 0.62 \cdot H \cdot \sqrt{\frac{(43 \cdot H)}{E}} \quad \text{normal flank face stress}$$

Tool characteristics:

$wl := 300 \cdot \text{nm}$ tool wear land

$\text{radius} := 300 \cdot \text{nm}$ diamond edge radius

$\text{ang} := 10 \cdot \text{deg}$ clearance angle

Material behavior:

$sb := 50 \cdot \text{nm}$ mat'l spring back

Dynamic Cutting Force

Duty cycle index:

$$\text{HSR}_{22} := 0.010 \quad \text{22\% EDC} \quad a_m := \frac{a}{2} \quad \text{ellipse major axis} \quad b_m := \frac{b}{2} \quad \text{ellipse minor axis}$$

$$v_{\text{critical}} := 2 \cdot \pi \cdot a_m \cdot f \quad v := \text{HSR}_{22} \cdot v_{\text{critical}} \quad v = 0.03 \frac{\text{mm}}{\text{s}}$$

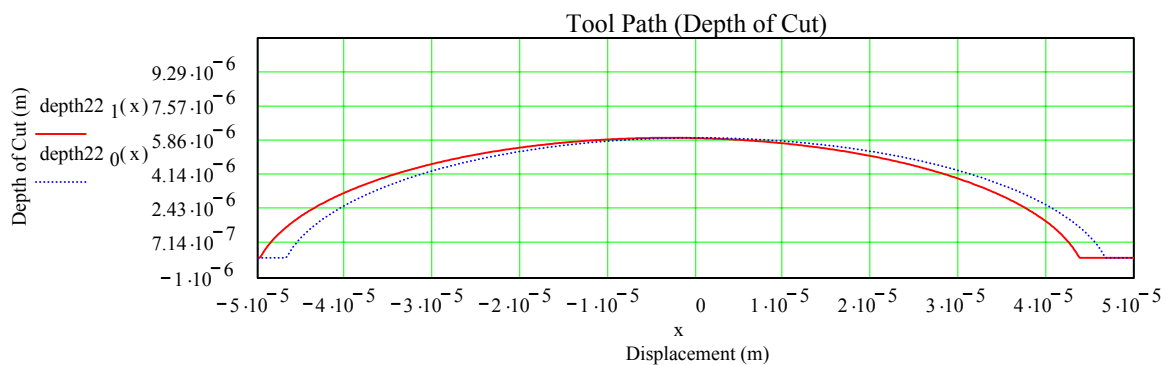
$$f_{22 \text{ index}} := \frac{v}{f} \quad f_{22 \text{ index}} = 2.985 \mu\text{m}$$

Chip thickness: $x := -50 \mu\text{m}, -49.80 \mu\text{m}.. 50 \mu\text{m}$

$$y_1(x) := \sqrt{\left[1 - \frac{(x + f_{22 \text{ index}})^2}{a_m^2}\right]} \cdot b_m^2 \quad y_0(x) := \sqrt{\left[1 - \frac{x^2}{a_m^2}\right]} \cdot b_m^2 \quad y_{\text{surface}} := b_m - d$$

$$\text{depth}_{22_1}(x) := \begin{cases} 0 & \text{if } x < -\sqrt{\left(1 - \frac{y_{\text{surface}}^2}{b_m^2}\right)} \cdot a_m^2 - f_{22 \text{ index}} \\ -y_{\text{surface}} + y_1(x) & \text{if } -\sqrt{\left(1 - \frac{y_{\text{surface}}^2}{b_m^2}\right)} \cdot a_m^2 - f_{22 \text{ index}} \leq x \leq \sqrt{\left(1 - \frac{y_{\text{surface}}^2}{b_m^2}\right)} \cdot a_m^2 - f_{22 \text{ index}} \\ 0 & \text{otherwise} \end{cases}$$

$$\text{depth}_{22_0}(x) := \begin{cases} 0 & \text{if } x < -\sqrt{\left(1 - \frac{y_{\text{surface}}^2}{b_m^2}\right)} \cdot a_m^2 \\ -y_{\text{surface}} + y_0(x) & \text{if } -\sqrt{\left(1 - \frac{y_{\text{surface}}^2}{b_m^2}\right)} \cdot a_m^2 \leq x \leq \sqrt{\left(1 - \frac{y_{\text{surface}}^2}{b_m^2}\right)} \cdot a_m^2 \\ 0 & \text{otherwise} \end{cases}$$



$$\theta_1(x) := \arccos\left(1 - \frac{\text{depth22}_1(x)}{r}\right)$$

$$\theta_0(x) := \arccos\left(1 - \frac{\text{depth22}_0(x)}{r}\right)$$

$$A1_{\text{chip22}}(x) := \left[r^2 \cdot \theta_1(x) - (r - \text{depth22}_1(x)) \cdot \sqrt{\text{depth22}_1(x) \cdot (2 \cdot r - \text{depth22}_1(x))} \right]$$

$$A0_{\text{chip22}}(x) := \left[r^2 \cdot \theta_0(x) - (r - \text{depth22}_0(x)) \cdot \sqrt{\text{depth22}_0(x) \cdot (2 \cdot r - \text{depth22}_0(x))} \right]$$

$$L1_{22}(x) := 2 \cdot r \cdot \theta_1(x)$$

$$L0_{22}(x) := 2 \cdot r \cdot \theta_0(x)$$

$$\text{chip22}_{\text{thick}}(x) := \begin{cases} 0 & \text{if } x < \frac{-f22_{\text{index}}}{2} \\ (\text{depth22}_0(x) - \text{depth22}_1(x)) & \text{if } x > \frac{-f22_{\text{index}}}{2} \end{cases}$$

$$\text{wear22}_{\text{land}}(x) := \begin{cases} w_l & \text{if } x \leq \frac{-f22_{\text{index}}}{2} \\ \left[w_l \cdot \left[1 - \left[\frac{(x)}{a_m} \right] \right] \right] & \text{if } \frac{-f22_{\text{index}}}{2} < x \leq a_m \\ 0 & \text{otherwise} \end{cases}$$

$$A1_{f22}(x) := L1_{22}(x) \cdot \left[\text{radius} + \text{wear22}_{\text{land}}(x) + \frac{(2 \cdot sb)}{3 \cdot \tan(\text{ang})} \right]$$

$$A0_{f22}(x) := L0_{22}(x) \cdot \left[\text{radius} + \text{wear22}_{\text{land}}(x) + \frac{(2 \cdot sb)}{3 \cdot \tan(\text{ang})} \right]$$

$$A_{22} \text{ fric}(x) := \begin{cases} 0 & \text{if } x \leq \frac{-f_{22} \text{ index}}{2} \\ A_{0 f_{22}}(x) & \text{if } \frac{-f_{22} \text{ index}}{2} < x \end{cases}$$

$$A_{22} \text{ chip}(x) := \begin{cases} 0 & \text{if } x \leq \frac{-f_{22} \text{ index}}{2} \\ A_{0 \text{ chip}_{22}}(x) - A_{1 \text{ chip}_{22}}(x) & \text{if } \frac{-f_{22} \text{ index}}{2} < x \end{cases}$$

$$\theta(x) := \frac{d}{dx} y_0(x)$$

$$\Lambda_{\text{shear}}(x) := \frac{\pi}{4} - \frac{\theta(x)}{2}$$

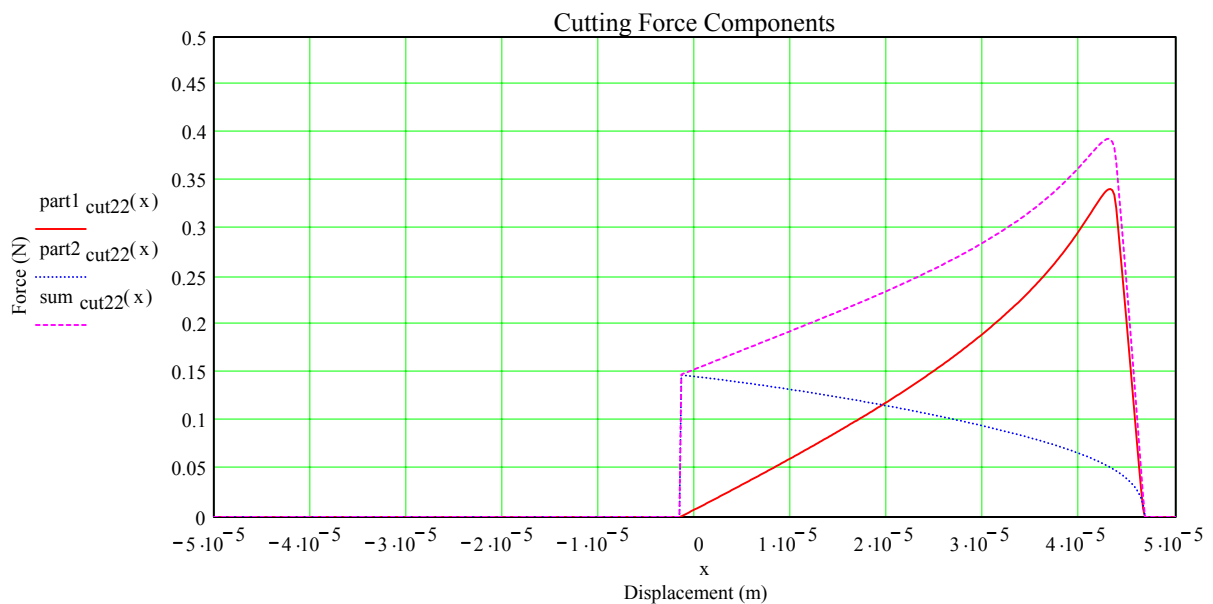
$$H_{22a} := H \cdot 2.7 \quad H_{22b} := H \cdot 2.7$$

$$\sigma_{f_{22}} := 0.62 \cdot H_{22b} \cdot \sqrt{\frac{(43 \cdot H_{22b})}{E}}$$

$$\text{part1}_{\text{cut}_{22}}(x) := \left(H_{22a} \cdot \frac{A_{22} \text{ chip}(x)}{3} \right) \cdot \left(1 + \frac{\cot(\Lambda_{\text{shear}}(x))}{\sqrt{3}} \right)$$

$$\text{part2}_{\text{cut}_{22}}(x) := \mu_f \sigma_{f_{22}} \cdot A_{22} \text{ fric}(x)$$

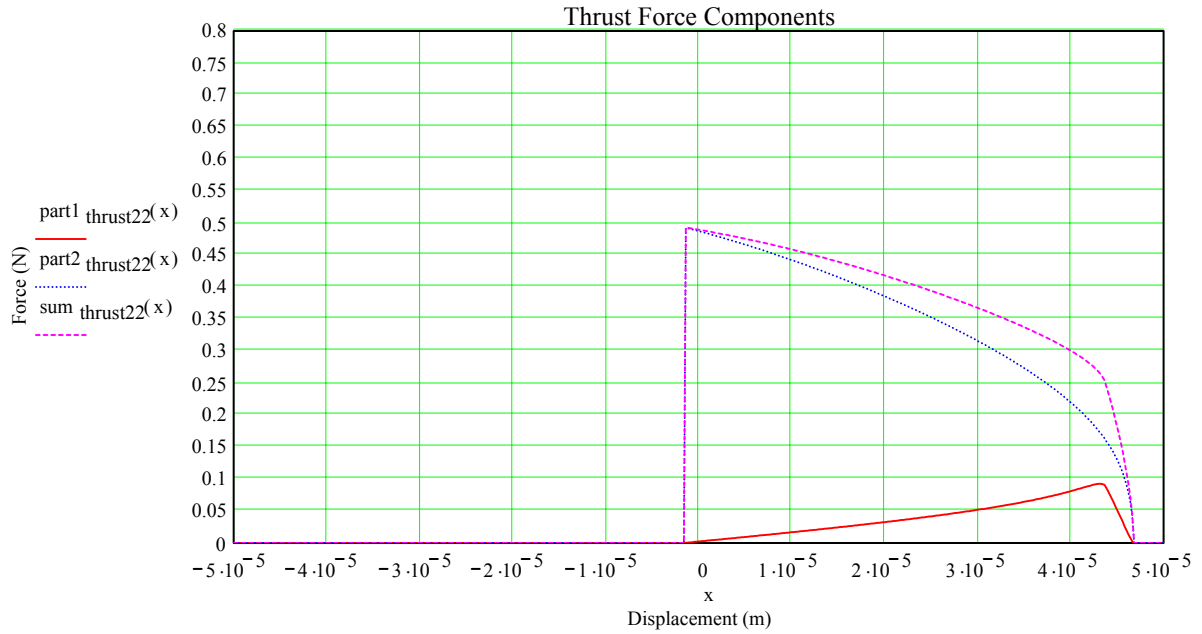
$$\text{sum}_{\text{cut}_{22}}(x) := \text{part1}_{\text{cut}_{22}}(x) + \text{part2}_{\text{cut}_{22}}(x)$$



$$\text{part1_thrust22}(x) := \mu \cdot \left(H_{22a} \cdot \frac{A_{22_chip}(x)}{3} \right) \cdot \left(1 + \frac{\cot(\Lambda_{shear}(x))}{\sqrt{3}} \right)$$

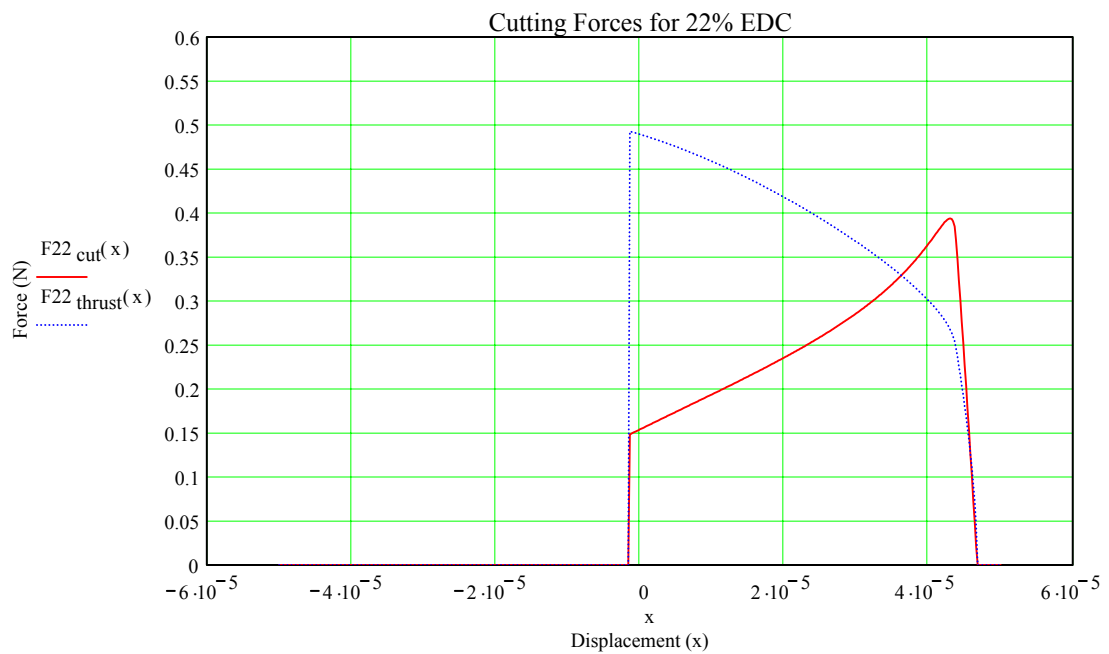
$$\text{part2_thrust22}(x) := \sigma_{f22} \cdot A_{22_fric}(x)$$

$$\text{sum_thrust22}(x) := \text{part1_thrust22}(x) + \text{part2_thrust22}(x)$$



$$F_{22_cut}(x) := \text{sum_cut22}(x)$$

$$F_{22_thrust}(x) := \text{sum_thrust22}(x)$$



Dynamic Cutting Force

Duty cycle index:

$$v_{23 \text{ ratio}} := 0.035 \quad \text{23\% EDC} \quad a_m := \frac{a}{2} \quad \text{ellipse major axis} \quad b_m := \frac{b}{2} \quad \text{ellipse minor axis}$$

$$v_{\text{critical}} := 2 \cdot \pi \cdot a_m \cdot f \quad v := v_{23 \text{ ratio}} \cdot v_{\text{critical}} \quad v = 0.104 \frac{\text{mm}}{\text{s}}$$

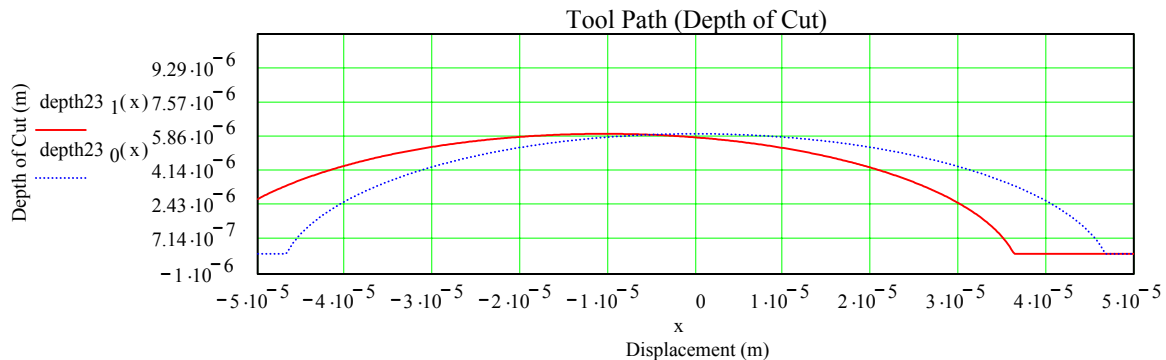
$$f_{23 \text{ index}} := \frac{v}{f} \quad f_{23 \text{ index}} = 10.446 \mu\text{m}$$

Chip thickness: $x := -50 \mu\text{m}, -49.80 \mu\text{m}.. 50 \mu\text{m}$

$$y_1(x) := \sqrt{\left[1 - \frac{(x + f_{23 \text{ index}})^2}{a_m^2}\right]} \cdot b_m^2 \quad y_0(x) := \sqrt{\left[1 - \frac{x^2}{a_m^2}\right]} \cdot b_m^2 \quad y_{\text{surface}} := b_m - d$$

$$\text{depth}_{23 \ 1}(x) := \begin{cases} 0 & \text{if } x < -\sqrt{\left(1 - \frac{y_{\text{surface}}^2}{b_m^2}\right)} \cdot a_m^2 - f_{23 \text{ index}} \\ -y_{\text{surface}} + y_1(x) & \text{if } -\sqrt{\left(1 - \frac{y_{\text{surface}}^2}{b_m^2}\right)} \cdot a_m^2 - f_{23 \text{ index}} \leq x \leq \sqrt{\left(1 - \frac{y_{\text{surface}}^2}{b_m^2}\right)} \cdot a_m^2 - f_{23 \text{ index}} \\ 0 & \text{otherwise} \end{cases}$$

$$\text{depth}_{23 \ 0}(x) := \begin{cases} 0 & \text{if } x < -\sqrt{\left(1 - \frac{y_{\text{surface}}^2}{b_m^2}\right)} \cdot a_m^2 \\ -y_{\text{surface}} + y_0(x) & \text{if } -\sqrt{\left(1 - \frac{y_{\text{surface}}^2}{b_m^2}\right)} \cdot a_m^2 \leq x \leq \sqrt{\left(1 - \frac{y_{\text{surface}}^2}{b_m^2}\right)} \cdot a_m^2 \\ 0 & \text{otherwise} \end{cases}$$



$$\theta 1(x) := \arccos\left(1 - \frac{\text{depth}23_1(x)}{r}\right)$$

$$\theta 0(x) := \arccos\left(1 - \frac{\text{depth}23_0(x)}{r}\right)$$

$$A1_{\text{chip}23}(x) := \left[r^2 \cdot \theta 1(x) - (r - \text{depth}23_1(x)) \cdot \sqrt{\text{depth}23_1(x) \cdot (2 \cdot r - \text{depth}23_1(x))} \right]$$

$$A0_{\text{chip}23}(x) := \left[r^2 \cdot \theta 0(x) - (r - \text{depth}23_0(x)) \cdot \sqrt{\text{depth}23_0(x) \cdot (2 \cdot r - \text{depth}23_0(x))} \right]$$

$$L1_{23}(x) := 2 \cdot r \cdot \theta 1(x)$$

$$L0_{23}(x) := 2 \cdot r \cdot \theta 0(x)$$

$$\text{chip_thick}(x) := \begin{cases} 0 & \text{if } x < \frac{-f23_{\text{index}}}{2} \\ (\text{depth}23_0(x) - \text{depth}23_1(x)) & \text{if } x > \frac{-f23_{\text{index}}}{2} \end{cases}$$

$$\text{wear}23_{\text{land}}(x) := \begin{cases} w1 & \text{if } x \leq \frac{-f23_{\text{index}}}{2} \\ \left[(w1) \cdot \left[1 - \left[\frac{(x)}{a_m} \right] \right] \right] & \text{if } \frac{-f23_{\text{index}}}{2} < x \leq a_m \\ 0 & \text{otherwise} \end{cases}$$

$$A1_{f23}(x) := L1_{23}(x) \cdot \left[\text{radius} + \text{wear}23_{\text{land}}(x) + \frac{(2 \cdot sb)}{3 \cdot \tan(\text{ang})} \right]$$

$$A0_{f23}(x) := L0_{23}(x) \cdot \left[\text{radius} + \text{wear}23_{\text{land}}(x) + \frac{(2 \cdot sb)}{3 \cdot \tan(\text{ang})} \right]$$

$$A_{23} \text{ fric}(x) := \begin{cases} 0 & \text{if } x \leq \frac{-f_{23} \text{ index}}{2} \\ A_{0 f_{23}}(x) & \text{if } \frac{-f_{23} \text{ index}}{2} < x \end{cases}$$

$$A_{23} \text{ chip}(x) := \begin{cases} 0 & \text{if } x \leq \frac{-f_{23} \text{ index}}{2} \\ A_{0 \text{ chip}_{23}}(x) - A_{1 \text{ chip}_{23}}(x) & \text{if } \frac{-f_{23} \text{ index}}{2} < x \end{cases}$$

$$\theta(x) := \frac{d}{dx} y_0(x)$$

$$\Lambda_{\text{shear}}(x) := \frac{\pi}{4} - \frac{\theta(x)}{2}$$

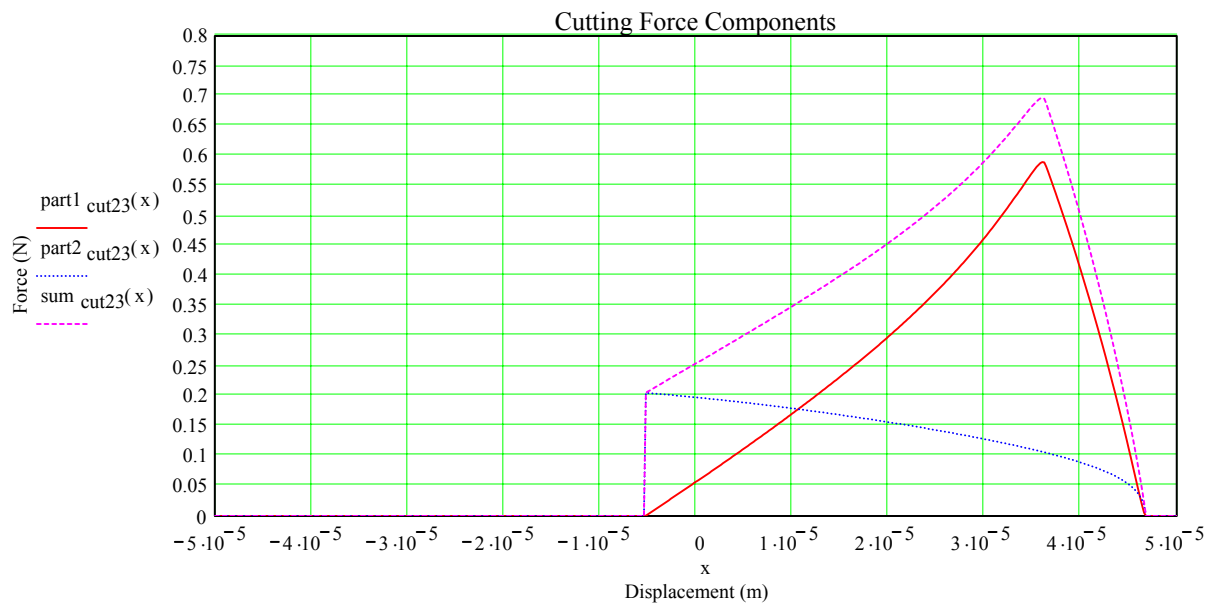
$$H_{23a} := H \cdot 1.6 \quad H_{23b} := H \cdot 3.3$$

$$\sigma_{f_{23}} := 0.62 \cdot H_{23b} \cdot \sqrt{\frac{(43 \cdot H_{23b})}{E}}$$

$$\text{part1}_{\text{cut}_{23}}(x) := \left(H_{23a} \cdot \frac{A_{23} \text{ chip}(x)}{3} \right) \cdot \left(1 + \frac{\cot(\Lambda_{\text{shear}}(x))}{\sqrt{3}} \right)$$

$$\text{part2}_{\text{cut}_{23}}(x) := \mu_f \sigma_{f_{23}} \cdot A_{23} \text{ fric}(x)$$

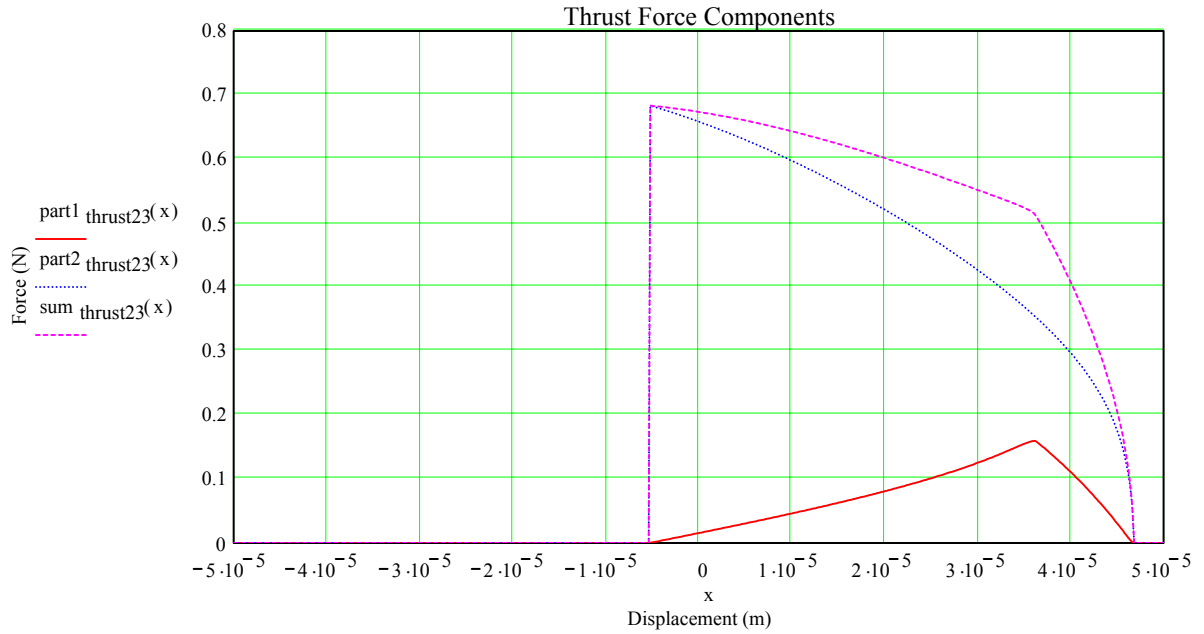
$$\text{sum}_{\text{cut}_{23}}(x) := \text{part1}_{\text{cut}_{23}}(x) + \text{part2}_{\text{cut}_{23}}(x)$$



$$\text{part1_thrust23}(x) := \mu \cdot \left(H_{23a} \cdot \frac{A_{23_chip}(x)}{3} \right) \cdot \left(1 + \frac{\cot(\Lambda_{shear}(x))}{\sqrt{3}} \right)$$

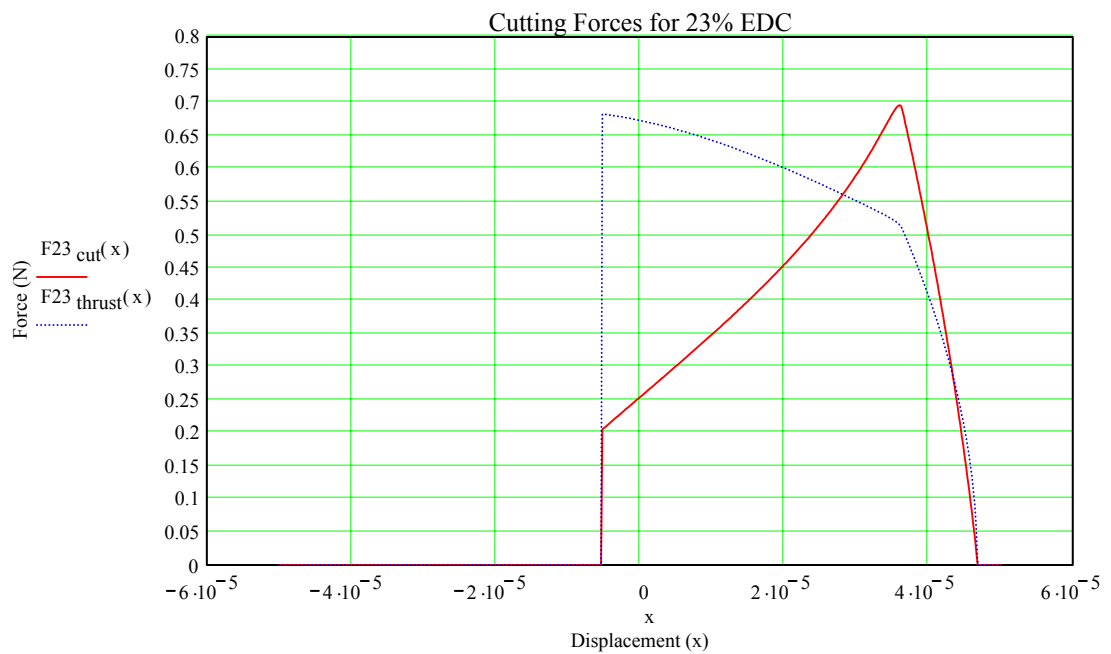
$$\text{part2_thrust23}(x) := \sigma_{f23} \cdot A_{23_fric}(x)$$

$$\text{sum_thrust23}(x) := \text{part1_thrust23}(x) + \text{part2_thrust23}(x)$$



$$F_{23_cut}(x) := \text{sum_cut23}(x)$$

$$F_{23_thrust}(x) := \text{sum_thrust23}(x)$$



Dynamic Cutting Force

Duty cycle index:

$$v_{25 \text{ ratio}} := 0.0725 \text{ 25\% EDC} \quad a_m := \frac{a}{2} \text{ ellipse major axis} \quad b_m := \frac{b}{2} \text{ ellipse minor axis}$$

$$v_{\text{critical}} := 2 \cdot \pi \cdot a_m \cdot f \quad v := v_{25 \text{ ratio}} \cdot v_{\text{critical}} \quad v = 0.216 \frac{\text{mm}}{\text{s}}$$

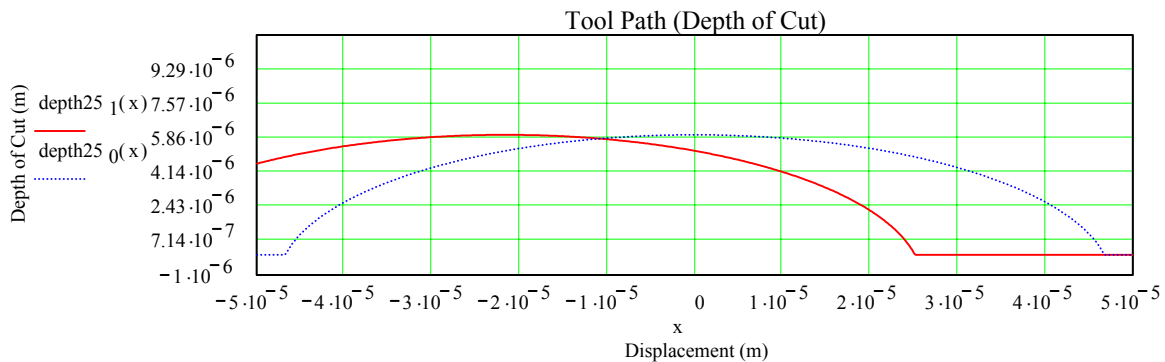
$$f_{25 \text{ index}} := \frac{v}{f} \quad f_{25 \text{ index}} = 21.638 \mu\text{m}$$

Chip thickness: $x := -50 \mu\text{m}, -49.80 \mu\text{m}.. 50 \mu\text{m}$

$$y_1(x) := \sqrt{\left[1 - \frac{(x + f_{25 \text{ index}})^2}{a_m^2}\right]} \cdot b_m^2 \quad y_0(x) := \sqrt{\left[1 - \frac{x^2}{a_m^2}\right]} \cdot b_m^2 \quad y_{\text{surface}} := b_m - d$$

$$\text{depth}_{25_1}(x) := \begin{cases} 0 & \text{if } x < -\sqrt{\left(1 - \frac{y_{\text{surface}}^2}{b_m^2}\right)} \cdot a_m^2 - f_{25 \text{ index}} \\ -y_{\text{surface}} + y_1(x) & \text{if } -\sqrt{\left(1 - \frac{y_{\text{surface}}^2}{b_m^2}\right)} \cdot a_m^2 - f_{25 \text{ index}} \leq x \leq \sqrt{\left(1 - \frac{y_{\text{surface}}^2}{b_m^2}\right)} \cdot a_m^2 - f_{25 \text{ index}} \\ 0 & \text{otherwise} \end{cases}$$

$$\text{depth}_{25_0}(x) := \begin{cases} 0 & \text{if } x < -\sqrt{\left(1 - \frac{y_{\text{surface}}^2}{b_m^2}\right)} \cdot a_m^2 \\ -y_{\text{surface}} + y_0(x) & \text{if } -\sqrt{\left(1 - \frac{y_{\text{surface}}^2}{b_m^2}\right)} \cdot a_m^2 \leq x \leq \sqrt{\left(1 - \frac{y_{\text{surface}}^2}{b_m^2}\right)} \cdot a_m^2 \\ 0 & \text{otherwise} \end{cases}$$



$$\theta 1(x) := \arccos\left(1 - \frac{\text{depth}25_1(x)}{r}\right)$$

$$\theta 0(x) := \arccos\left(1 - \frac{\text{depth}25_0(x)}{r}\right)$$

$$A1_{\text{chip}25}(x) := \left[r^2 \cdot \theta 1(x) - (r - \text{depth}25_1(x)) \cdot \sqrt{\text{depth}25_1(x) \cdot (2 \cdot r - \text{depth}25_1(x))} \right]$$

$$A0_{\text{chip}25}(x) := \left[r^2 \cdot \theta 0(x) - (r - \text{depth}25_0(x)) \cdot \sqrt{\text{depth}25_0(x) \cdot (2 \cdot r - \text{depth}25_0(x))} \right]$$

$$L1_{25}(x) := 2 \cdot r \cdot \theta 1(x)$$

$$L0_{25}(x) := 2 \cdot r \cdot \theta 0(x)$$

$$\text{chip}25_{\text{thick}}(x) := \begin{cases} 0 & \text{if } x < \frac{-f25_{\text{index}}}{2} \\ (\text{depth}25_0(x) - \text{depth}25_1(x)) & \text{if } x > \frac{-f25_{\text{index}}}{2} \end{cases}$$

$$\text{wear}25_{\text{land}}(x) := \begin{cases} w1 & \text{if } x \leq \frac{-f25_{\text{index}}}{2} \\ \left[(w1) \cdot \left[1 - \left[\frac{(x)}{a_m} \right] \right] \right] & \text{if } \frac{-f25_{\text{index}}}{2} < x \leq a_m \\ 0 & \text{otherwise} \end{cases}$$

$$A1_{f25}(x) := L1_{25}(x) \cdot \left[\text{radius} + \text{wear}25_{\text{land}}(x) + \frac{(2 \cdot sb)}{3 \cdot \tan(\text{ang})} \right]$$

$$A0_{f25}(x) := L0_{25}(x) \cdot \left[\text{radius} + \text{wear}25_{\text{land}}(x) + \frac{(2 \cdot sb)}{3 \cdot \tan(\text{ang})} \right]$$

$$A_{25} \text{ fric}(x) := \begin{cases} 0 & \text{if } x \leq \frac{-f_{25} \text{ index}}{2} \\ A_{0 f_{25}}(x) & \text{if } \frac{-f_{25} \text{ index}}{2} < x \end{cases}$$

$$A_{25} \text{ chip}(x) := \begin{cases} 0 & \text{if } x \leq \frac{-f_{25} \text{ index}}{2} \\ A_{0 \text{ chip}_{25}}(x) - A_{1 \text{ chip}_{25}}(x) & \text{if } \frac{-f_{25} \text{ index}}{2} < x \end{cases}$$

$$\theta(x) := \frac{d}{dx} y_0(x)$$

$$\Lambda_{\text{shear}}(x) := \frac{\pi}{4} - \frac{\theta(x)}{2}$$

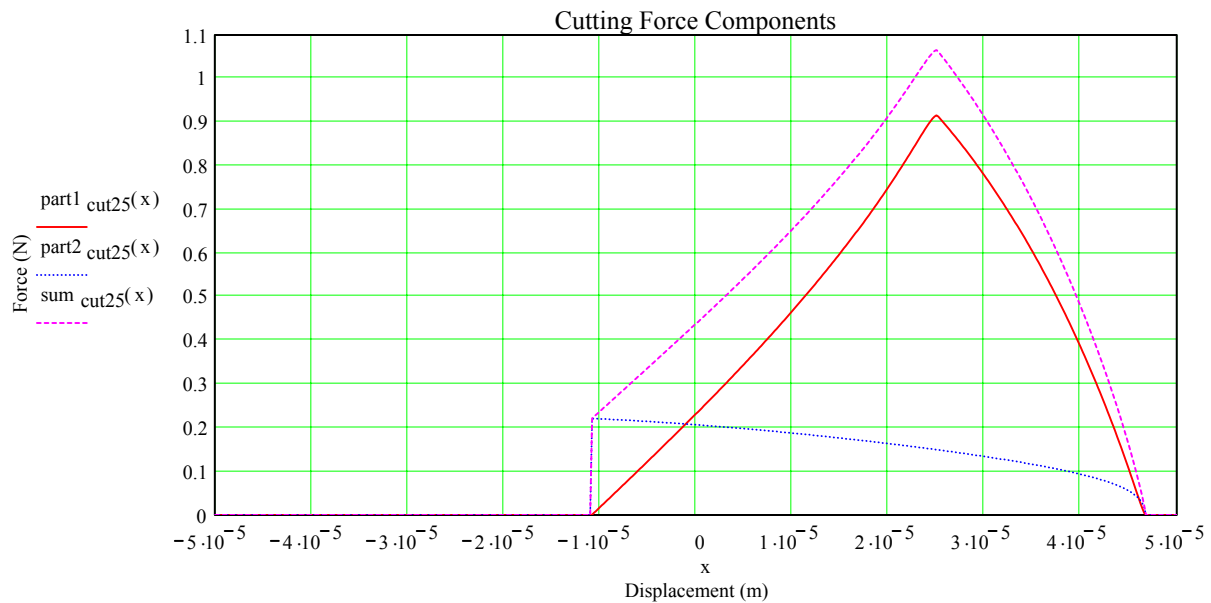
$$H_{25a} := H \cdot 1.5 \quad H_{25b} := H \cdot 3.4$$

$$\sigma_{f_{25}} := 0.62 \cdot H_{25b} \cdot \sqrt{\frac{(43 \cdot H_{25b})}{E}}$$

$$\text{part1}_{\text{cut}_{25}}(x) := \left(H_{25a} \cdot \frac{A_{25} \text{ chip}(x)}{3} \right) \cdot \left(1 + \frac{\cot(\Lambda_{\text{shear}}(x))}{\sqrt{3}} \right)$$

$$\text{part2}_{\text{cut}_{25}}(x) := \mu_f \sigma_{f_{25}} \cdot A_{25} \text{ fric}(x)$$

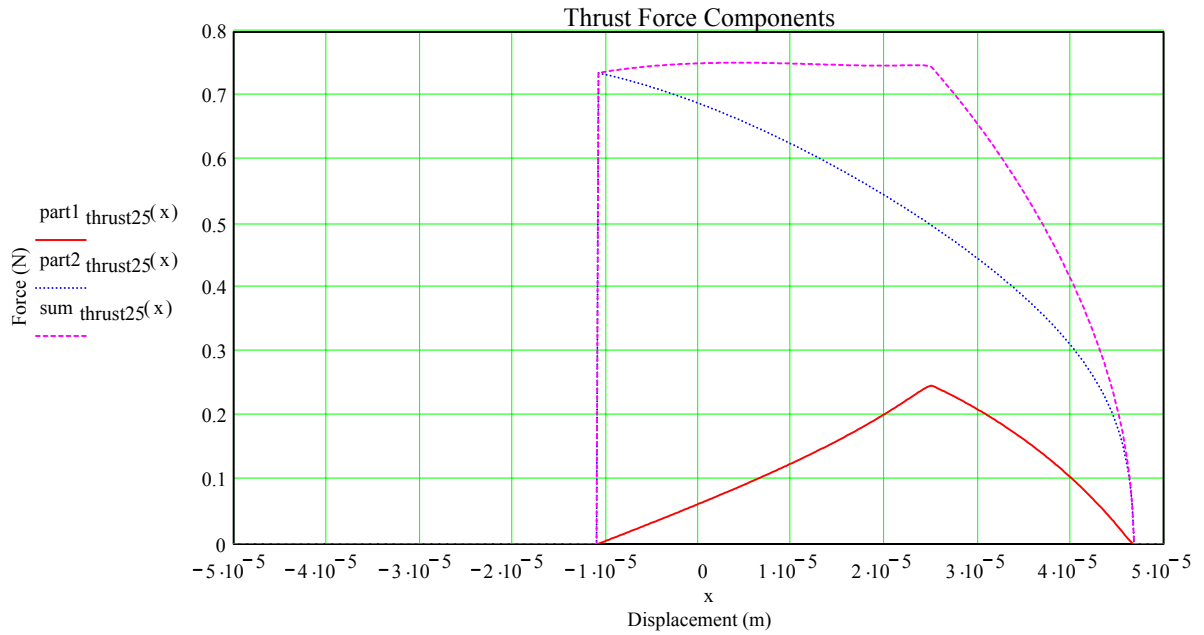
$$\text{sum}_{\text{cut}_{25}}(x) := \text{part1}_{\text{cut}_{25}}(x) + \text{part2}_{\text{cut}_{25}}(x)$$



$$\text{part1_thrust25}(x) := \mu \cdot \left(H_{25a} \cdot \frac{A_{25_chip}(x)}{3} \right) \cdot \left(1 + \frac{\cot(\Lambda_{shear}(x))}{\sqrt{3}} \right)$$

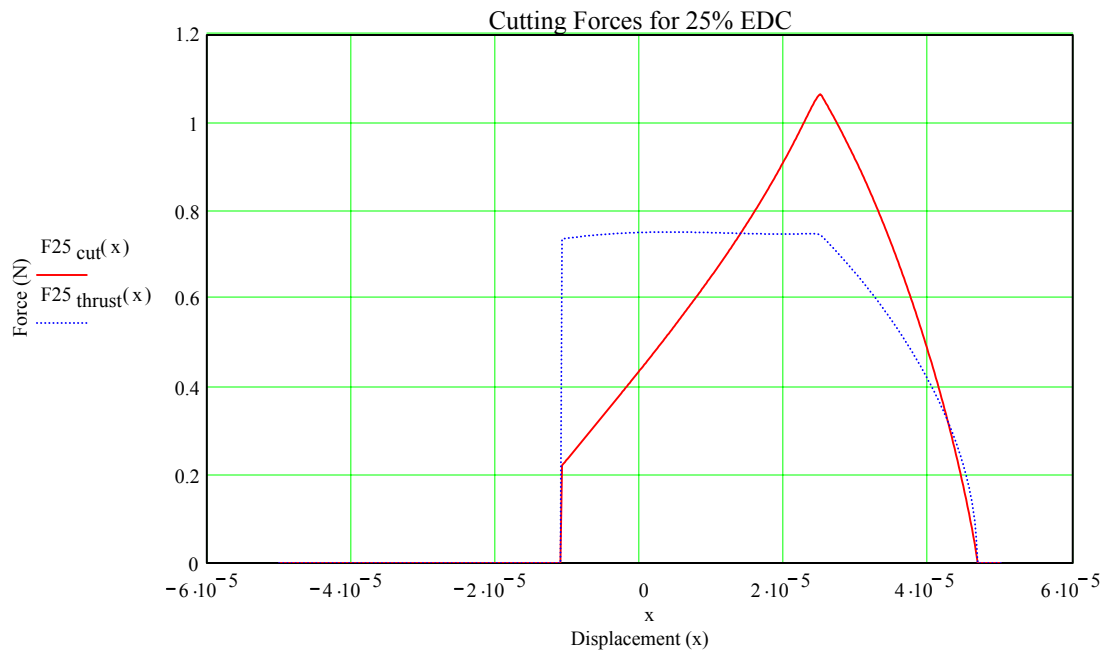
$$\text{part2_thrust25}(x) := \sigma_{f25} \cdot A_{25_fric}(x)$$

$$\text{sum_thrust25}(x) := \text{part1_thrust25}(x) + \text{part2_thrust25}(x)$$



$$F_{25_cut}(x) := \text{sum_cut25}(x)$$

$$F_{25_thrust}(x) := \text{sum_thrust25}(x)$$



Static Cutting Force

Chip Area for non-overlapping cuts:

$$\theta := \arccos\left(1 - \frac{d}{r}\right) \quad \text{tool engagement angle}$$

$$A_{\text{chip}} := r^2 \cdot \theta - (r-d) \cdot \sqrt{d \cdot (2 \cdot r - d)} \quad \text{chip area via tool radius and depth of cut}$$

$$A_{\text{chip}} = 1.517 \cdot 10^3 \mu\text{m}^2$$

Tool contact length:

$$L := 2 \cdot r \cdot \theta$$

$$L = 379.537 \mu\text{m}$$

$$A_f := L \cdot \left[\text{radius} + w_l + \frac{(2 \cdot s_b)}{3 \cdot \tan(\text{ang})} \right]$$

$$A_f = 299.471 \mu\text{m}^2 \quad \text{surface contact (friction) surface area}$$

Force calculations:

$$H_c := H \cdot 2.8 \quad H_t := H \cdot 3.4$$

$$\sigma_f := 0.62 \cdot H_t \cdot \sqrt{\frac{(43 \cdot H_t)}{E}} \quad \text{average normal stress}$$

$$\sigma_f = 2.298 \cdot 10^9 \text{ Pa}$$

$$F_{\text{static}_y} := \left(H_c \cdot \frac{A_{\text{chip}}}{3} \right) \cdot \left(1 + \frac{\cot(\phi_{\text{stat}})}{\sqrt{3}} \right) + \mu_f \sigma_f A_f \quad \text{cutting force}$$

$$F_{\text{static}_z} := \mu \cdot \left(H_c \cdot \frac{A_{\text{chip}}}{3} \right) \cdot \left(1 + \frac{\cot(\phi_{\text{stat}})}{\sqrt{3}} \right) + \sigma_f A_f \quad \text{thrust force}$$

$$F_{\text{static}_y} = 2.44 \text{ N}$$

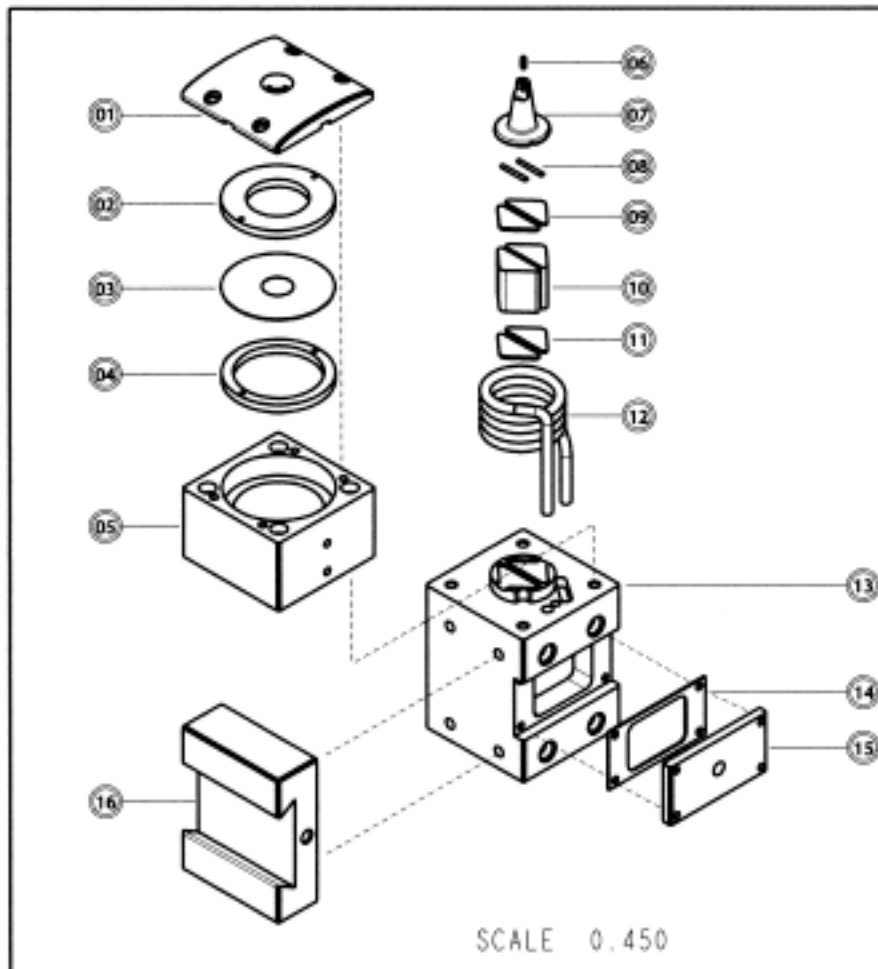
$$F_{\text{static}_y} = 0.549 \text{ lbf}$$

or

$$F_{\text{static}_z} = 1.291 \text{ N}$$


$$F_{\text{static}_z} = 0.29 \text{ lbf}$$

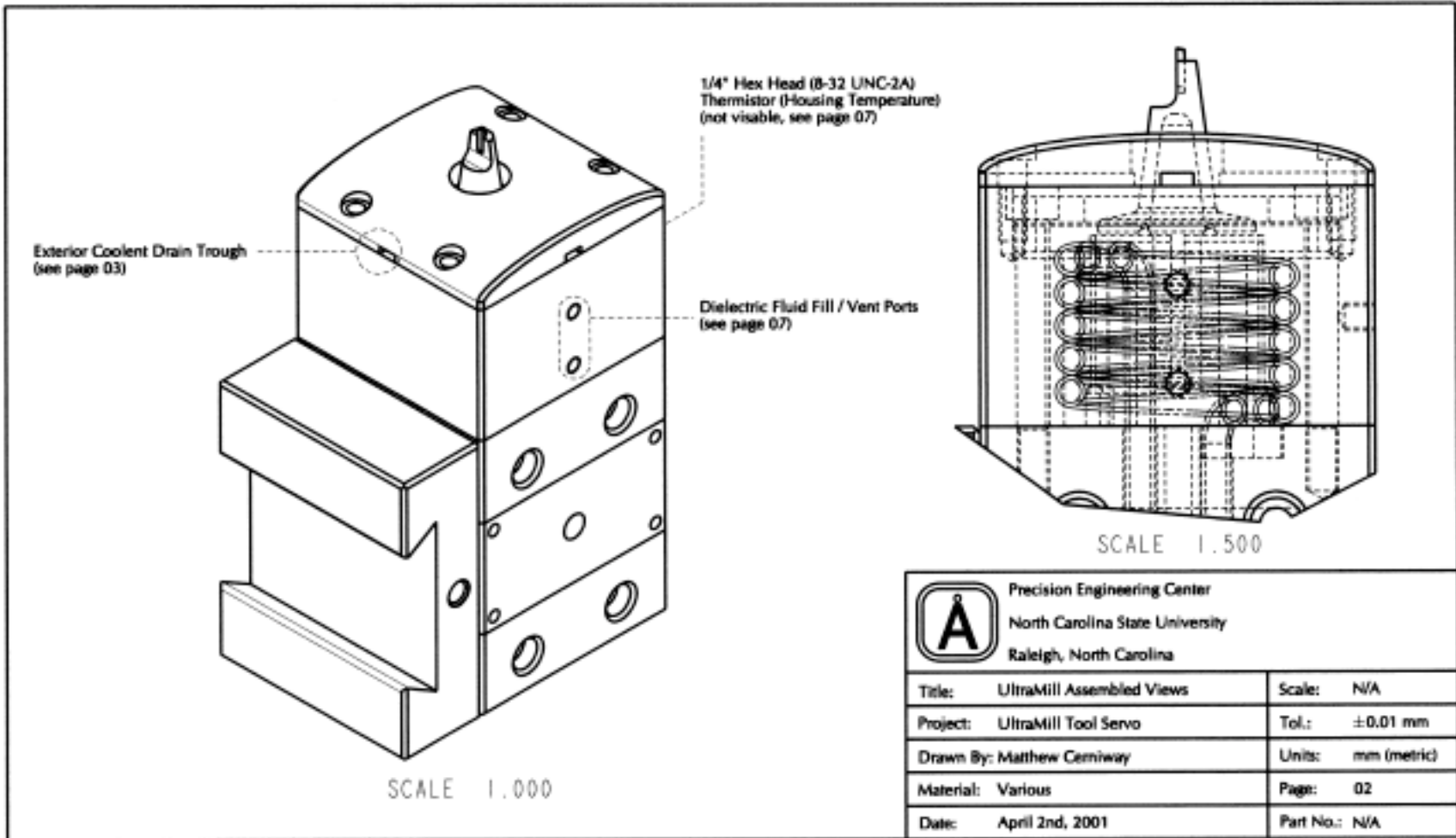
APPENDIX B: ULTRAMILL HIGH SPEED DETAILED DRAWINGS

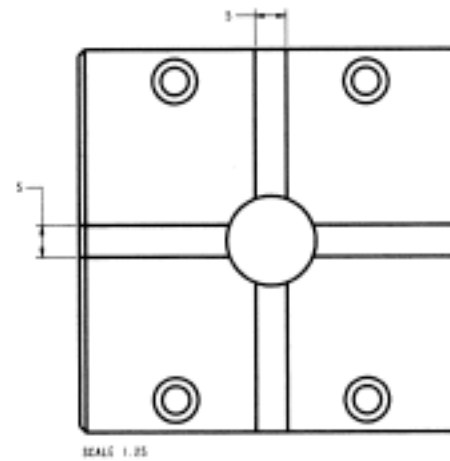
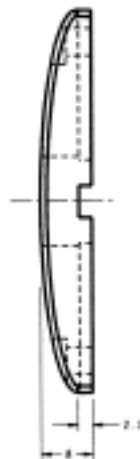
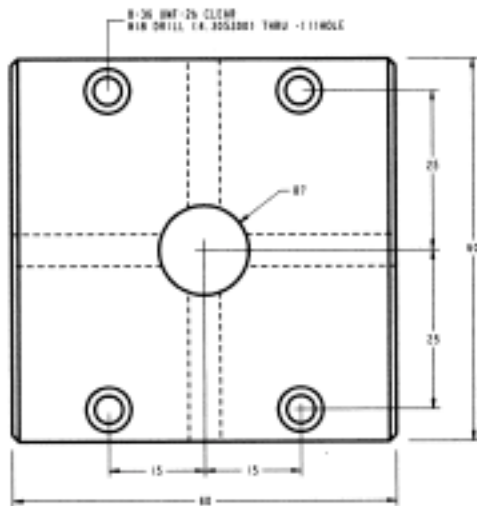


Item No.	Part No.	Description	Material	Qty.	Page
01	UM001	Protective Cap	1018 Steel	1	03
02	UM002	Diaphragm Backing Nut	1018 Steel	1	04
03	UM003	Diaphragm (Preload Spring)	Titanium (6AL-4V)	1	05
04	UM004	Preload Adjustment Nut	1018 Steel	1	06
05	UM005	Stack Housing	1018 Steel	1	07
06	UM006	Diamond Tool	Synthetic Diamond	1	08
07	UM007	Cutter Head	SCNB	1	09
08	UM008	Pivot Half-Rounds	AD99.5 Alumina	2	10
09	UM009	Ceramic End Caps (top)	Ceramic	2	11
10	UM010	Piezoelectric Actuator	PZWT100 Ceramic	2	12
11	UM011	Ceramic End Caps (bottom)	Ceramic	2	11
12	UM012	Cooling Coils	Copper	1	13
13	UM013	Base	1018 Steel	1	14
14	UM014	Gasket	Aramid w/ Nitrile Binder	1	15
15	UM015	Power / Cooling Compartment Cover	1018 Steel	1	16
16	UM016	Alaris Attachment	1018 Steel	1	17
--	--	Equipment for Operation	--	--	18
--	--	Notes	--	--	19

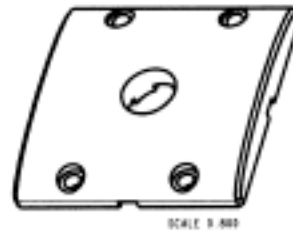
Revision 2.1 (April 4th, 2001)

	Precision Engineering Center	
	North Carolina State University	
Raleigh, North Carolina		
Title:	UltraMill Exploded View	Scale: 0.45
Project:	UltraMill High Speed Tool Servo	Tol.: N/A
Drawn By:	Matthew Cerniway	Units: mm (metric)
Material:	Various	Page: 01
Date:	April 2nd, 2001	Part No.: N/A



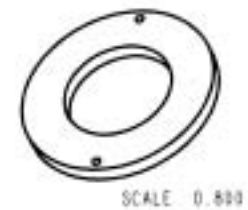
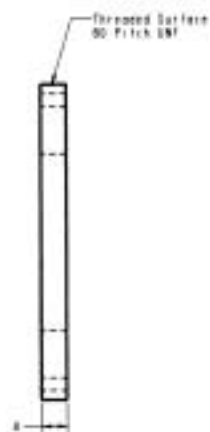
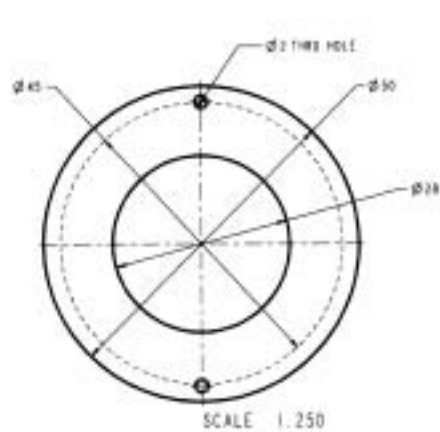


- Notes:
- 1) Part is symmetric about centerline
 - 2) Chamfer is 45° x 1 mm unless otherwise stated
 - 3) Counter bore depth is 4 mm from the top surface
 - 4) Finish all over (FOA)




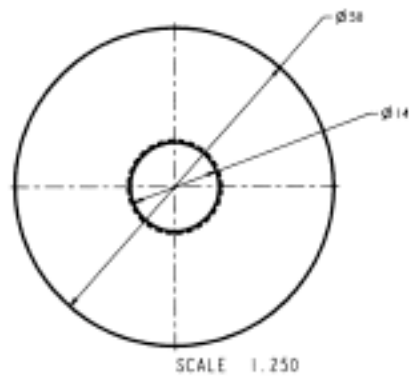
Precision Engineering Center
North Carolina State University
Raleigh, North Carolina

Title:	Protective Cap	Scale:	1.25
Project:	UltraMill Tool Servo	Tol.:	±0.01 mm
Drawn By:	Matthew Cerniway	Units:	mm (metric)
Material:	1018 Steel	Page:	03
Date:	April 2nd, 2001	Part No.:	UM001



Notes:
 1) $\varnothing 30$ is the mean diameter of the external threaded surface
 2) FAO

	Precision Engineering Center North Carolina State University Raleigh, North Carolina	
	Title: Diaphragm Backing Nut	Scale: N/A
Project: UltraMill Tool Servo	Tol.: ± 0.01 mm	
Drawn By: Matthew Cerniway	Units: mm (metric)	
Material: 1018 Steel	Page: 04	
Date: April 2nd, 2001	Part No.: UIM002	

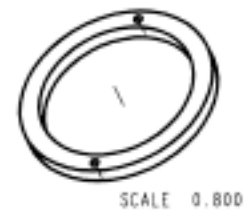
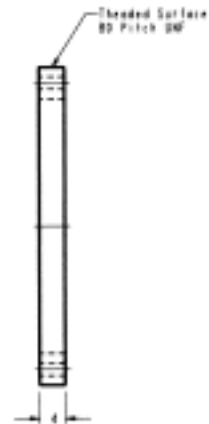
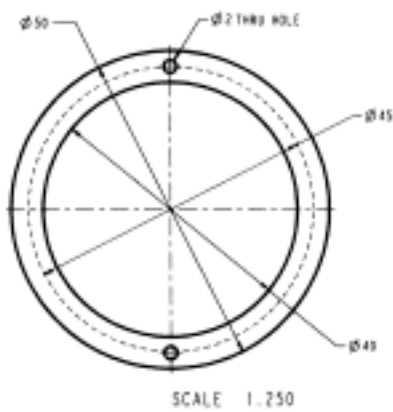


- Notes:
 1) Break the edge of the inner radius (denoted by R 0.4)
 2) Material is standard 0.016" titanium sheet metal



Precision Engineering Center
 North Carolina State University
 Raleigh, North Carolina

Title:	Diaphragm (PZT Preload)	Scale:	N/A
Project:	UltraMill Tool Servo	Tol.:	± 0.01 mm
Drawn By:	Matthew Cerniway	Units:	mm (metric)
Material:	Titanium 6AL-4V	Page:	05
Date:	April 2nd, 2001	Part No.:	UM003

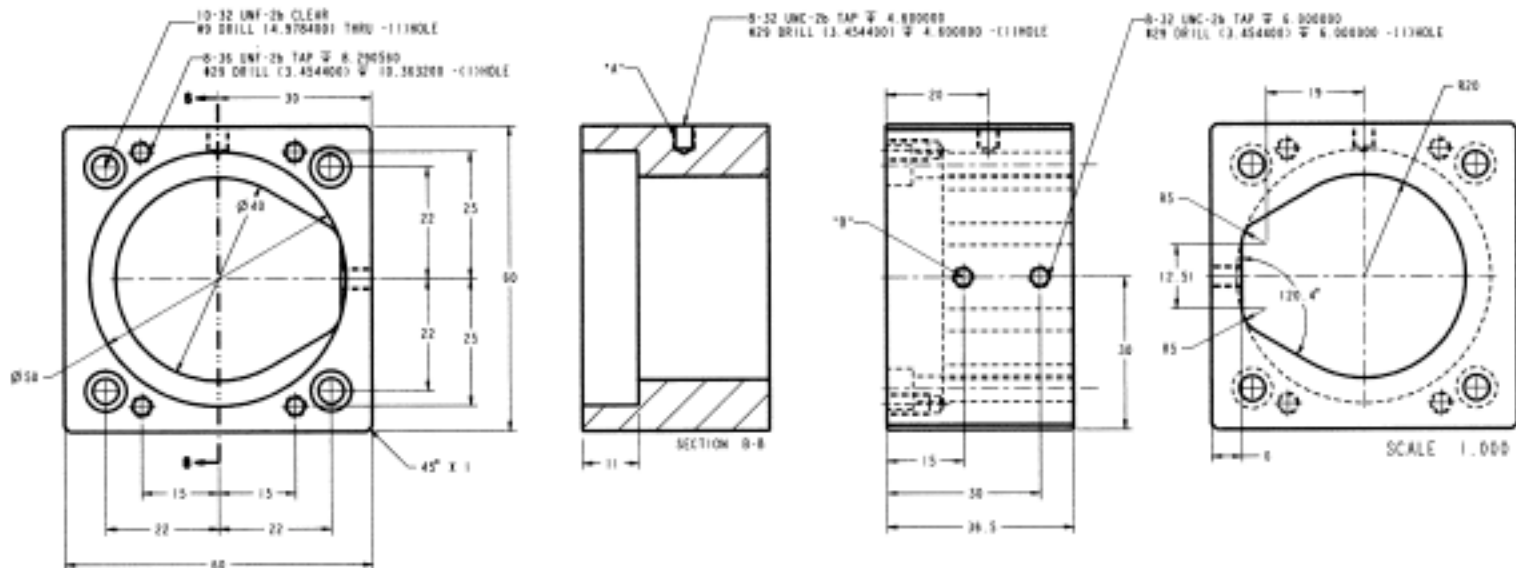


Notes:
 1) $\varnothing 50$ is the mean diameter of the external threaded surface
 2) FAD

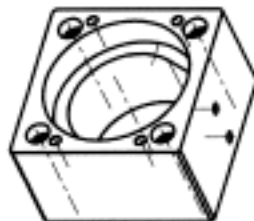


Precision Engineering Center
 North Carolina State University
 Raleigh, North Carolina

Title:	Preload Adjustment Nut	Scale:	N/A
Project:	UltraMill Tool Servo	Tol.:	± 0.01 mm
Drawn By:	Matthew Carnway	Units:	mm (metric)
Material:	1018 Steel	Page:	06
Date:	April 2nd, 2001	Part No.:	UM004

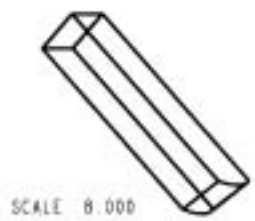
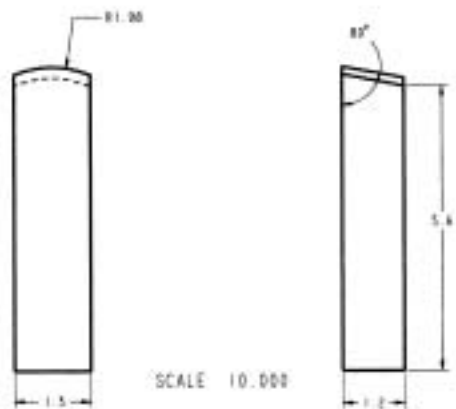


- Note:
 1) FAD
 2) Item "A", Housing Thermistor
 Manufacturer: Omega
 Style: CH-950
 Temperature Range: 0-100 °C ±0.1 °C
 3) Item "B", Body Access Port
 Self-Sealing Pan Head Screw
 Material: 316 Stainless Steel
 O-Ring: Buna-N




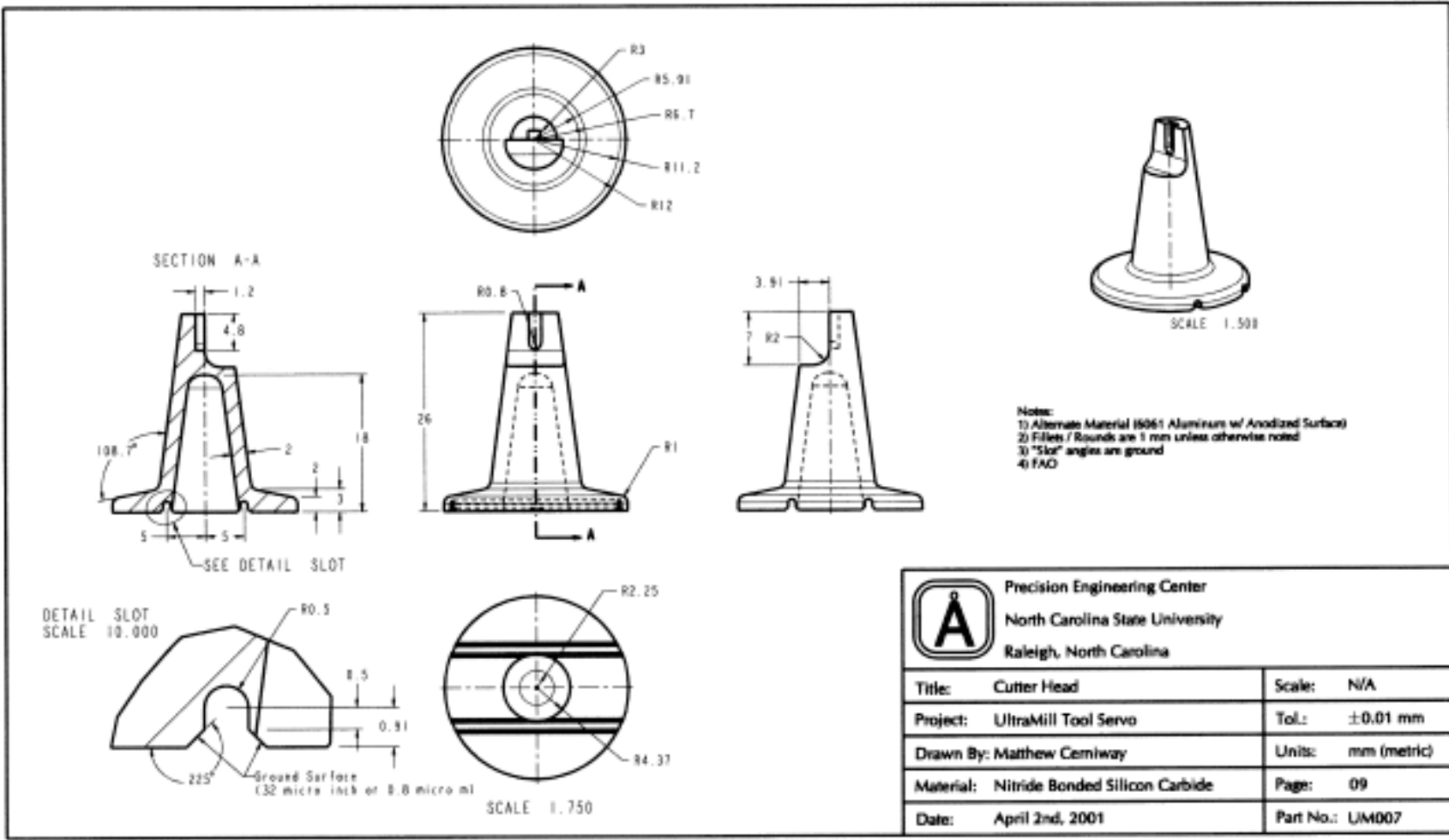
SCALE 0.600

	Precision Engineering Center	
	North Carolina State University Raleigh, North Carolina	
Title:	PZT Stack Housing	Scale: N/A
Project:	UltraMill Tool Servo	Tol.: ±0.01 mm
Drawn By:	Matthew Cerniway	Units: mm (metric)
Material:	1018 Steel	Page: 07
Date:	April 2nd, 2001	Part No.: UM005



Notes:
 1) Manufactured by Charlton Tool
 2) Radius of tool ordered is 1 mm w/ 90° window

	Precision Engineering Center	
	North Carolina State University Raleigh, North Carolina	
Title:	0.5 mm Radius Diamond Tool	Scale: N/A
Project:	UltraMill Tool Servo	Tol.: ±0.01 mm
Drawn By:	Matthew Cerniway	Units: mm (metric)
Material:	Synthetic Diamond	Page: 08
Date:	April 2nd, 2001	Part No.: UM006

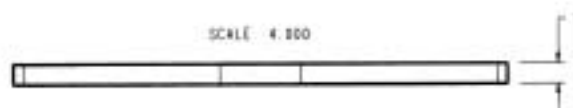
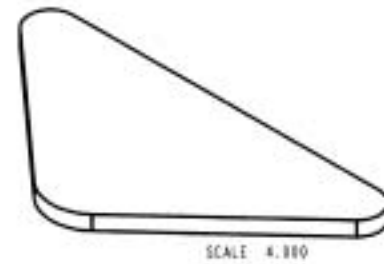
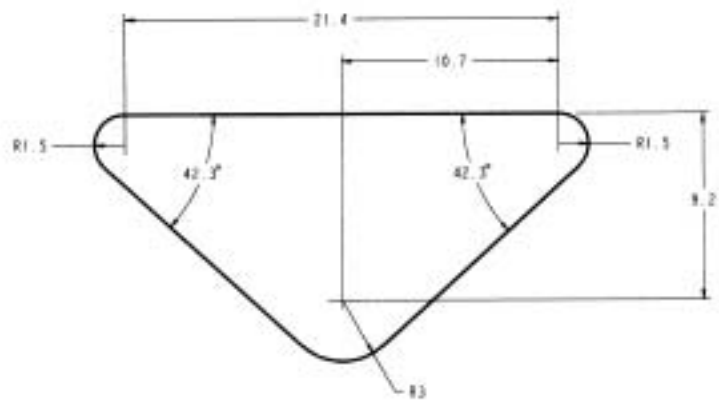


A	Precision Engineering Center	
	North Carolina State University Raleigh, North Carolina	
Title:	Cutter Head	Scale: N/A
Project:	UltraMill Tool Servo	Tol.: ±0.01 mm
Drawn By:	Matthew Cerniway	Units: mm (metric)
Material:	Nitride Bonded Silicon Carbide	Page: 09
Date:	April 2nd, 2001	Part No.: UM007



Notes:
1)

	Precision Engineering Center	
	North Carolina State University Raleigh, North Carolina	
Title:	Pivot Half-Rounds	Scale: N/A
Project:	UltraMill Tool Servo	Tol.: ±0.01 mm
Drawn By:	Matthew Cemiway	Units: mm (metric)
Material:	Coorstek AD99.5 Alumina Ceramic	Page: 10
Date:	April 2nd, 2001	Part No.: UM008

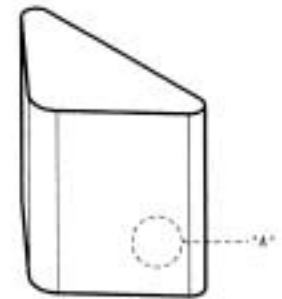
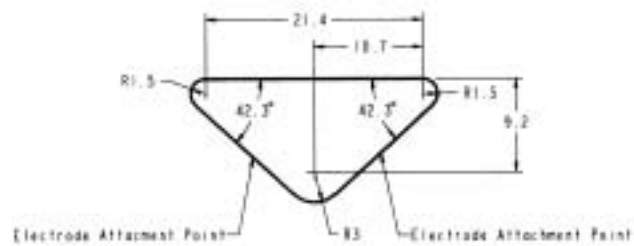


Notes:
1. Attached by Kinetic Ceramics at time of Manufacture



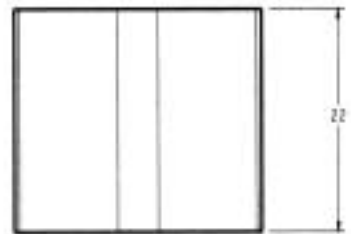
Precision Engineering Center
North Carolina State University
Raleigh, North Carolina

Title:	Piezoelectric Actuator Ceramic Caps	Scale:	4.0
Project:	UltraMill Tool Servo	Tol.:	± 0.10 mm
Drawn By:	Matthew Corniway	Units:	mm (metric)
Material:	Non-Active PZWT100 Ceramic	Page:	11
Date:	April 2nd, 2001	Part No.:	UM009 / 011




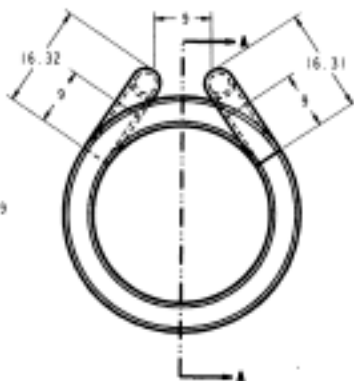
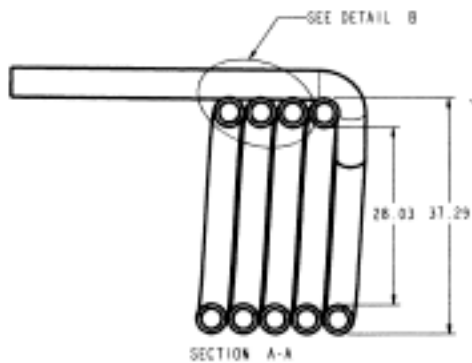
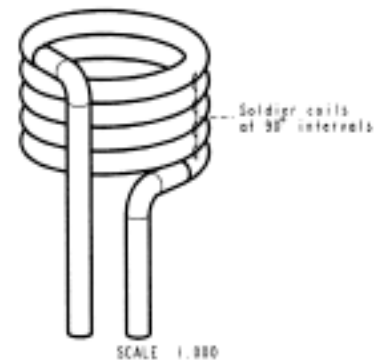
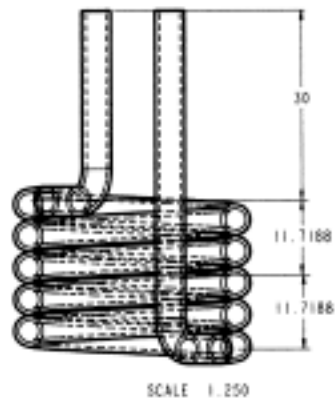
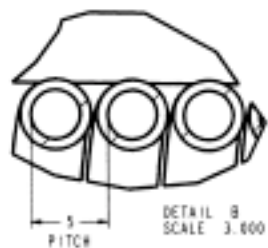
SCALE 2.000

SCALE 2.000



- Notes:
- 1) Stack coating is approx. 0.5mm (prevents electrode arcing)
 - 2) 36 layers / > 1300 micro strain / ~ 28 micro meters elongation
 - 3) Item 'A', Stack Thermistor
- Make: Omega
 Style: OH-909
 Dimensions: OD = 9.52mm, Thickness = 3.18 mm
 Temperature Range: 0-100° C ± 0.1° C

 Precision Engineering Center North Carolina State University Raleigh, North Carolina		
Title:	Piezoelectric Actuator	Scale: 2.0
Project:	UltraMill Tool Servo	Tol.: ± 0.10 mm
Drawn By:	Matthew Corniway	Units: mm (metric)
Material:	Kinetic Ceramics PZWT-100	Page: 12
Date:	April 2nd, 2001	Part No.: UM010

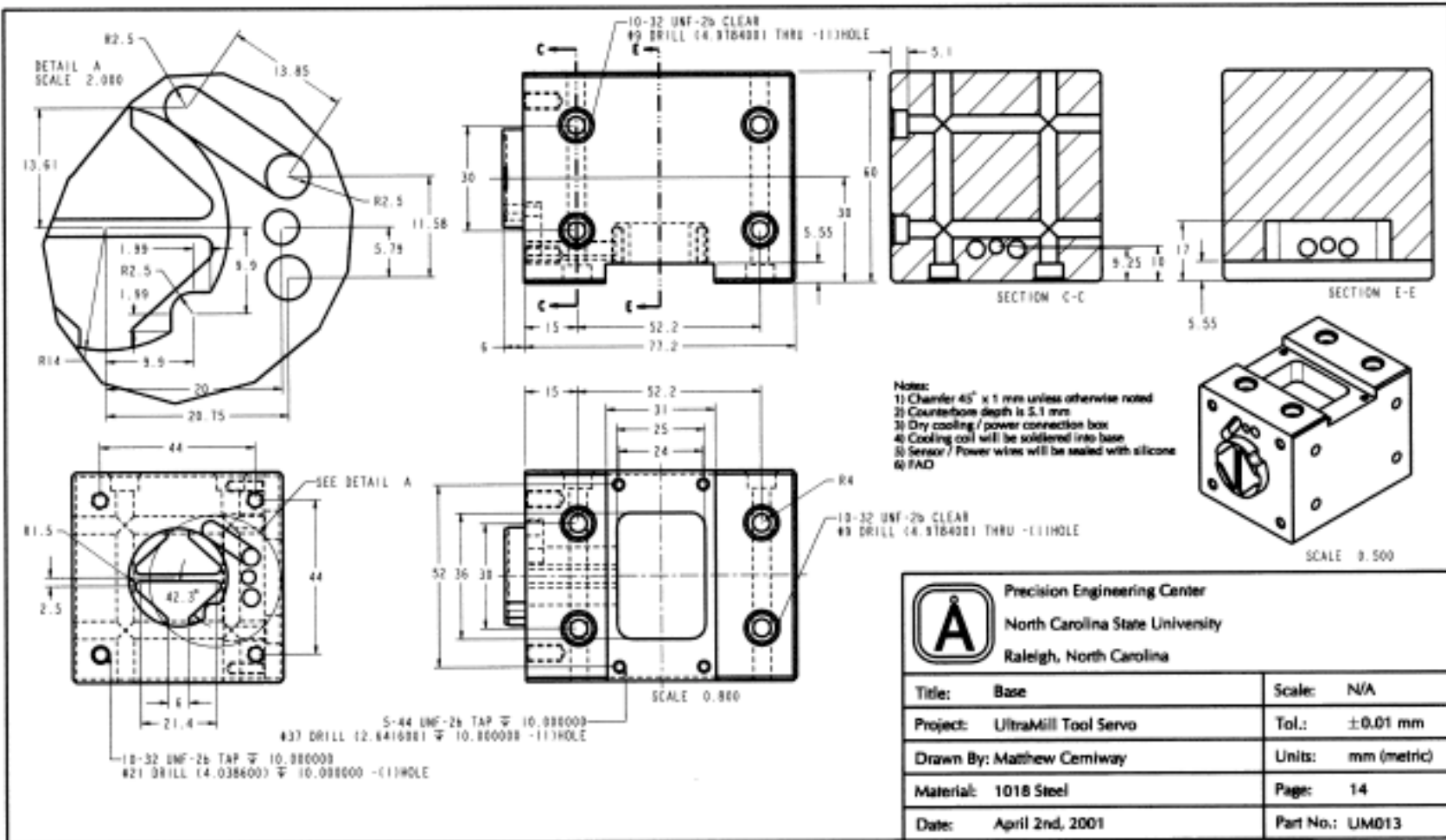


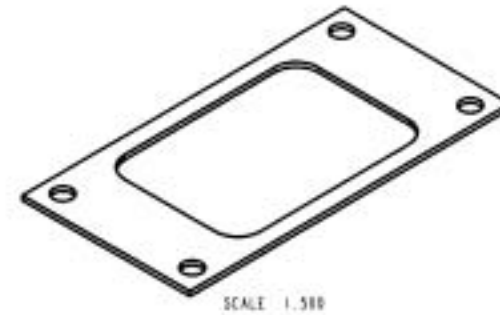
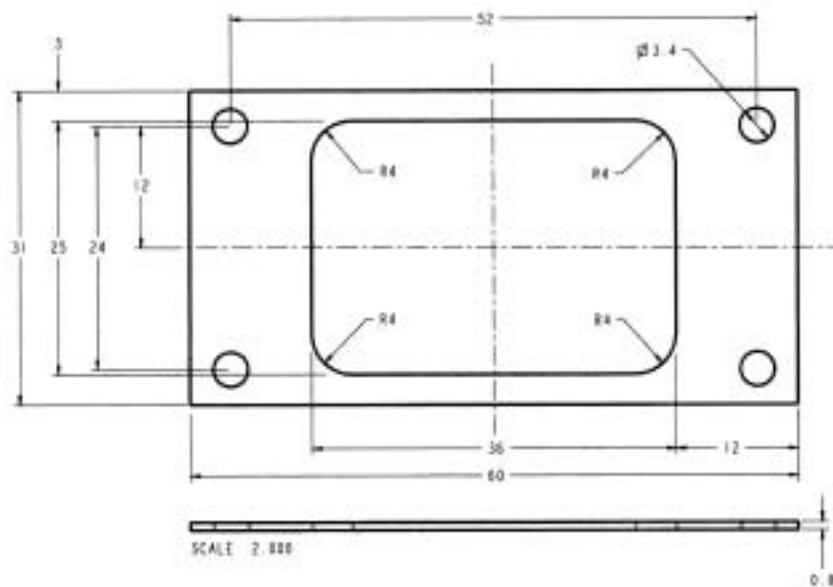
- Notes:
 1) Material: 122 Copper Tubing (3/16" Dia. / 0.030" wall thickness)
 2) Coil pitch = 5 mm
 3) Solder tack the coils together at 90° intervals




Precision Engineering Center
 North Carolina State University
 Raleigh, North Carolina

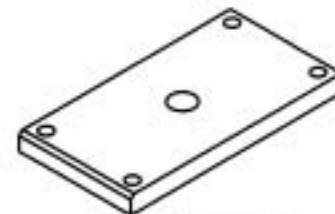
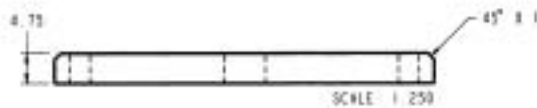
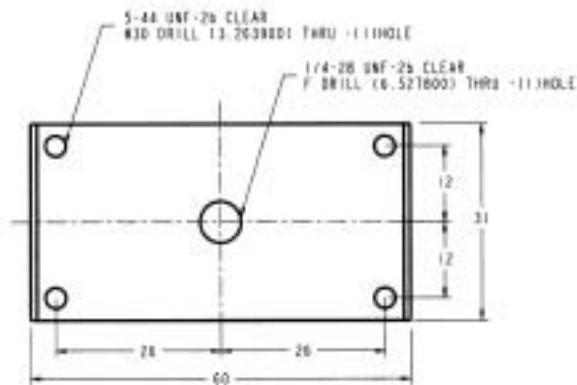
Title:	Cooling Coil	Scale:	N/A
Project:	UltraMill Tool Servo	Tol.:	±0.01 mm
Drawn By:	Matthew Cerniway	Units:	mm (metric)
Material:	Copper	Page:	13
Date:	April 2nd, 2001	Part No.:	UM012





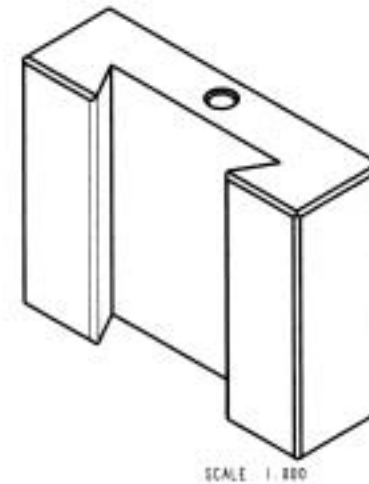
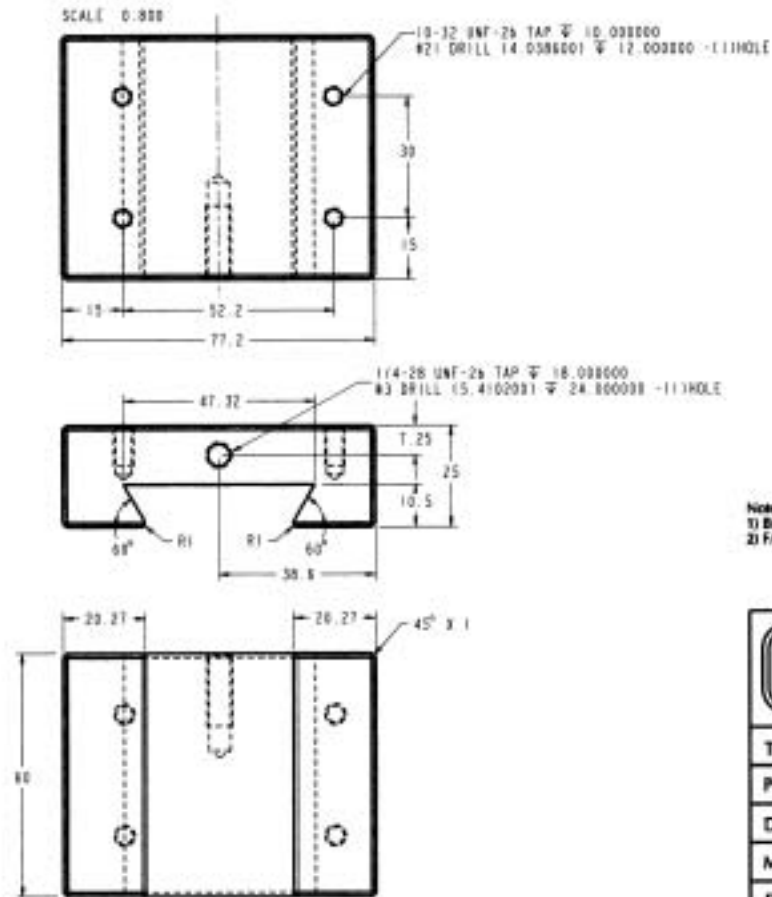
Notes:
1)

	Precision Engineering Center North Carolina State University Raleigh, North Carolina	
	Title: Main Port Gasket	Scale: N/A
Project: UltraMill Tool Servo	Tol.: ± 0.01 mm	
Drawn By: Matthew Carniway	Units: mm (metric)	
Material: Aramid Fiber w/ Nitrile Binder	Page: 15	
Date: April 2nd, 2001	Part No.: UMD14	



Notes:
1) Additional holes will be required to accommodate process cooling lines
2) FAD

	Precision Engineering Center	
	North Carolina State University Raleigh, North Carolina	
Title:	Power / Cooling Compartment Cover	Scale: N/A
Project:	UltraMill Tool Servo	Tol.: ±0.01 mm
Drawn By:	Matthew Carniway	Units: mm (metric)
Material:	1018 Steel	Page: 16
Date:	April 2nd, 2001	Part No.: UMD15



Notes:
1) Break all edges
2) FAD



Precision Engineering Center
North Carolina State University
Raleigh, North Carolina

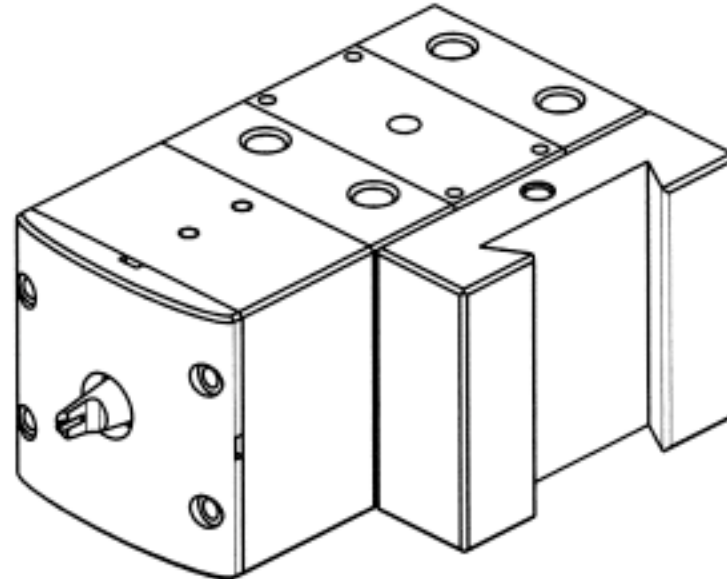
Title:	Aluris Tool Post Attachment	Scale:	N/A
Project:	UltraMill Tool Servo	Tol.:	± 0.01 mm
Drawn By:	Matthew Cerniway	Units:	mm (metric)
Material:	1018 Steel	Page:	17
Date:	April 2nd, 2001	Part No.:	UM016

Amplifier
 500 W Magnetic Coupled Linear Amplifier
 Manufacturer: Kinetic Ceramics
 Bandwidth: 500-5000 Hz @ 812 VAC
 Qty Required: 2
 Additional Note: Built in variable DC offset


Chiller
 Thermocube-400[®] Thermoelectric Air to Liquid Chiller
 Manufacturer: Solid State Cooling Systems
 Specifications:
 Operational Range: -10 to 50[°] C
 Cooling Capacity: 400 Watts @ 25[°] C ambient air
 Coolant: water/ethylene glycol mixture
 Noise: < 50 dB at 3 feet
 Size: 12.75" x 11.25" x 12.0"
 Weight: 33 lbs
 Pump: 3 liters/min @ 40 psi
 Control:
 Digital PID control for < 0.2[°] C accuracy
 Additional Notes:
 Reservoir with level sensor
 Alarm for over heating

Function Generator
 Manufacturer: HP (Agilent Technologies)
 Model: 8904A
 Range: DC to 600 kHz
 Channels: 2

Process Controller
 Dual Input Programmable Process Controller
 Manufacturer: Omega
 Model: CN3000
 Input: 2 thermistor series 400, 2252 Ω @ 25[°] C
 Output: RS-232, 4-20 mA/0-5 Vdc
 Accuracy: $\pm 0.2\%$ of range



SCALE 1:100

	Precision Engineering Center	
	North Carolina State University Raleigh, North Carolina	
Title:	Support Equipment	Scale: N/A
Project:	UltraMill Tool Servo	Tol.: N/A
Drawn By:	Matthew Cerniway	Units: N/A
Material:	N/A	Page: 18
Date:	April 2nd, 2001	Part No.: N/A

System Specifications

Elliptical Path

Delta X = 102.92 micro m
 Delta Y = 19.78 micro m
 T Components (a = b = 5 mm, c = 26 mm)

Head

Material = Nitride Bonded Silicon Carbide
 Material Properties (density = 2.6 gm/cc, modulus = 152 GPa, v = 0.2)
 Mass = 4.811 gm
 Center of Gravity (x = 0.0, y = 6.811, z = 0.105)
 Inertia About Axis (Ixx = 0.0005589 tonne*mm², Iyy = 0.00021413 tonne*mm², Izz = 0.00055415 tonne*mm²)
 Natural Frequency (1st = 27.47 kHz, 2nd = 28.45 kHz)
 Deflection @ 5N = 0.5 micro m

Natural Frequency (First)
 Total System = 4,503 Hz (via Modal Analysis)
 Head = 27,470 Hz (FEA)
 Stack = 10,744 Hz (FEA)
 Diaphragm = 9,885 Hz (FEA)

Cooling Requirements

Heat Generated at 5 kHz = 198 W

Cooling Fluid Specifications


Dimethylsiloxane Polymer (Dow Corning 561)
 Non-Toxic / Not Regulated
 Appearance = Clear
 Specific Gravity = 0.98
 Flash Point = 572 F
 Kinetic Viscosity @ 100 C = 0.15 stokes
 Dynamic Viscosity @ 100 C = 14.4 cP
 Specific Heat = 2094 J/Kg*K
 Thermal Diffusivity = 0.003 Ft²/hr
 Thermal Conductivity = 0.155 W/m*K

Piezoelectric Material

Formula (Kinetic Ceramics PZTW100)
 Strain = 1300 micro
 Physical Properties (Similar to PZT-5A)
 Stack Specific Information
 Capacitance = 0.25 micro farad
 Power Requirement @ 800 V and 5 kHz = 500 W

Misc Notes

Speed of Sound in Fluid = 1.2 Km/s
 Wavelength = 0.24 m
 Maximum Diaphragm Velocity @ 5kHz = 0.44 m/s
 Required Preload = 90 lbf

	Precision Engineering Center	
	North Carolina State University Raleigh, North Carolina	
Title:	System Notes	Scale: N/A
Project:	UltraMill Tool Servo	Tol.: N/A
Drawn By:	Matthew Cerniway	Units: N/A
Material:	N/A	Page: 19
Date:	April 2nd, 2001	Part No.: N/A